Development of advanced operators for enhanced on-chip biosensing in digital microfluidic platforms

by

Ehsan Samiei

B.Sc., Urmia University, Iran, 2007
M.Sc., K. N. Toosi University of Technology (KNTU), Iran, 2010

A THESIS SUBMITTED IN PARTIAL FULFILLMENT OF
THE REQUIREMENTS FOR THE DEGREE OF

DOCTOR OF PHILOSOPHY

in

THE COLLEGE OF GRADUATE STUDIES

(Engineering)

THE UNIVERSITY OF BRITISH COLUMBIA

(Okanagan)

December 2016

The undersigned certify that they have read, and recommend to the College of Graduate Studies for acceptance, a thesis entitled:

Development of advanced operators for enhanced on-chip biosensing in digital microfluidic platforms

Submitted by Ehsan Samiei in partial fulfillment of the requirements of

The degree of Doctor of Philosophy .

Dr. Mina Hoorfar, School of Engineering, The University of British Columbia
Supervisor, Professor (please print name and faculty/school above the line)

Dr. Homayoun Najjaran, School of Engineering, The University of British Columbia
Supervisory Committee Member, Professor (please print name and faculty/school in the line above)

Dr. Vladan Prodanovic, Department of Chemical and Biological Engineering, The University of British Columbia
Supervisory Committee Member, Professor (please print name and faculty/school in the line above)

Dr. Ian Foulds, School of Engineering, The University of British Columbia
University Examiner, Professor (please print name and faculty/school in the line above)

Dr. Ali Dolatabadi, Department of Mechanical and Industrial Engineering, Concordia University
External Examiner, Professor (please print name and university in the line above)

December 13, 2016
(Date submitted to Grad Studies)

Abstract

Over the past two decades, digital microfluidics (DMF) has grown significantly as a powerful tool for lab-on-a-chip (LOC) applications. Since the introduction of DMF with its primary capabilities in sample manipulation (transport, splitting and mixing) in the droplet format, many advances have been made towards the development of platforms capable of performing entire processes of biochemical assays in an automated fashion. These advances include the progress made towards the fabrication methods, and the development of techniques for sample manipulation and integration of biosensors. Despite the general success in such developments, DMF still lacks capabilities in sample manipulation (including the droplets and their contents, e.g. cells and microbeads), specifically for biosensing, in which sample preparation and post-sensing removal of the sample are required. Therefore, in majority of the applications, DMF has been used for processing parts of the entire assay, and after biosensing, the recovery of the chip was hindered due to the contamination of the biosensor for its hydrophilic behavior. This thesis aims at the development of advanced operators for accurate pre-sensing sample preparation, biosensing and post sensing sample removal. For this purpose, an unequal droplet splitting method is developed based on the geometrical modification of one actuating electrode, which enables dispensing/splitting droplets with a wide range of volumes and with an accuracy of over 99%. An electrohydrodynamic technique is developed for rapid mixing inside the stationary droplets, enhancing the mixing time and eliminating the need for frequent and cyclic transport of the droplet on the chip. A dielectrophoretic-gravity driven technique is developed for concentrating and focusing the particles and cells inside the sample droplet. Also, a systematic study has been performed on the surface properties and geometry of the biosensors to optimize their geometry and configuration on DMF devices for complete sample removal after biosensing. Finally, the application of the developed techniques for enhanced on-chip biosensing is shown for detection of *Cryptosporidium* as a proof of concept.

Preface

The research presented in this thesis is the original work performed by the author. This thesis was supervised by Dr. Mina Hoorfar at the Advanced Thermo-Fluidic Laboratory (ATFL) in the School of Engineering, University of British Columbia. Parts of this thesis have been published in different journals and presented in conferences. The details of the publications and the author's contributions in them are explained below:

a. Book chapter

[1] **E. Samiei** and M. Hoorfar, "Biosensing on Digital Microfluidics: From Sample Preparation to Detection", Book chapter in: A. Brolo, S. H. Oh and C. Escobedo, "Miniature Fluidic Devices for Rapid Biological Detection", Springer (2017). (Under review)

b. Refereed journal publications

[1] **E. Samiei**, M. Diaz de Leon Derby, A. Van den Berg and M. Hoorfar, (2016) "An electrohydrodynamic technique for rapid mixing in stationary droplets on digital microfluidic platforms", Lab Chip (Accepted). **Impact Factor: 5.586**
Contribution: Developing the idea, design of experiment, conducting parts of the experiments, performing major parts of data analysis, writing the manuscript.

[2] **E. Samiei**, M. Tabrizian and M. Hoorfar, (2016) "A review of digital microfluidics as portable platforms for lab-on a-chip applications", Lab Chip, 16, 2376-2396. **Impact Factor: 5.586**
Contribution: Developing the idea, performing the review, performing major parts of analysis, writing the manuscript.

[3] **E.Samiei**, G. S. Luka, H. Najjaran and M. Hoorfar, (2016) "Integration of biosensors into digital microfluidics: impact of hydrophilic surface of biosensors on droplet manipulation", Biosensors and Bioelectronics, 81, 480-486. **Impact Factor: 7.476**
Contribution: Developing the idea, design of experiment, conducting major parts of the experiments, performing the data analysis, writing major parts of the manuscript.

[4] B. A. Nestor, **E. Samiei**, R. Samanipour, A. Gupta, A. Van den Berg, M. Diaz de Leon Derby, Z. Wang, H. Rezaei Nejad, K. Kim and M. Hoorfar, (2016) "Digital microfluidic

platform for dielectrophoretic patterning of cells encapsulated in hydrogel droplets", RSC Advances, 6, 57409-57416. **Impact Factor: 3.289**
Contribution: Parts of the design of experiment, conducting parts of the experiments, performing parts of data analysis, writing parts of the manuscript.

[5] **E.Samiei**, H. R. Nejad and M. Hoorfar, (2015) "A dielectrophoretic-gravity driven particle focusing technique for digital microfluidic platforms", App. Phys. Lett., 106, 204101. **Impact Factor: 3.142**
Contribution: Developing the idea, design of experiment, conducting the experiments, performing major parts of data analysis, writing major parts of the manuscript.

[6] H. Rezaei Nejad, **E. Samiei**, A. Ahmadi and M. Hoorfar, (2015) "Gravity-driven hydrodynamic particle separation in digital microfluidic systems", RSC Advances, 5, 35966–35975. **Impact Factor: 3.289**
Contribution: Parts of the design of experiment, conducting parts of the experiments, performing parts of data analysis, writing parts of the manuscript.

[7] **E. Samiei** and M. Hoorfar, (2015) "Systematic analysis of geometrical based unequal droplet splitting in digital microfluidics", J. Micromech. Microeng., 25, 055008. **Impact Factor: 1.768**
Contribution: Developing the idea, design of experiment, conducting the experiments, performing the data analysis, writing the manuscript.

c. Conference proceedings and presentations

[1] **E. Samiei**, M. Diaz de Leon Derby, A. Van Den Berg and M. Hoorfar "Development of a dielectrophoretic-based technique for rapid droplet mixing in digital microfluidics", Dielectrophoresis 2016, MIT, July 13-15 2016, Cambridge, Massachusetts, USA.
Contribution: Developing the idea, design of experiment, conducting parts of the experiments, performing major parts of data analysis, writing the manuscript.

[2] **E. Samiei** and M. Hoorfar, "Geometrical optimization of the hydrophilic surfaces on digital microfluidics for successful droplet transport", Proceedings of The Canadian Society for

Mechanical Engineering (CSME) International Congress 2016, June 26-29, 2016, Kelowna, BC, Canada.
Contribution: Developing the idea, design of experiment, conducting the experiments, performing the data analysis, writing the manuscript.

[3] G. S. Luka, **E. Samiei**, T. Johnson, H. Najjaran and M. Hoorfar, “Label free interdigitated capacitive biosensor for the detection of Cryptosporidium”, MicroTAS 2016, 9-13 October 2016, Dublin, Ireland.
Contribution: Partial development of the idea, design of experiment, conducting parts of the experiments, performing major parts of data analysis, writing parts of the manuscript.

[4] G. S. Luka, **E. Samiei**, H. Najjaran and M. Hoorfar, “Digital microfluidic-based fluorescent biosensor for the multiplex and rapid detection of Cryptosporidium”, MicroTAS 2016, 9-13 October 2016, Dublin, Ireland.
Contribution: Partial development of the idea, design of experiment, conducting parts of the experiments, performing major parts of data analysis, writing parts of the manuscript.

[5] **E. Samiei**, H. R. Nejad and M. Hoorfar, "A novel density-based dielectrophoretic particle focusing technique for digital microfluidics", IEEE-MEMS 2015, 18-22 January, Estoril, Portugal.
Contribution: Developing the idea, design of experiment, conducting parts of the experiments, performing major parts of data analysis, writing major parts of the manuscript.

[6] H. R. Nejad, **E. Samiei** and M. Hoorfar, "Hydrodynamic density-based particle focusing in digital microfluidic systems", MicroTAS 2014, 26-30 October, San Antonio, Texas, USA.
Contribution: Partial development of the idea, conducting parts of the experiments, performing parts of data analysis, writing parts of the manuscript.

[7] H. R. Nejad, **E. Samiei** and M. Hoorfar, "Droplet dispensing from open to close digital microfluidic platforms", Nanotech 2014, 15-18 June, Washington D.C., USA.
Contribution: Partial development of the idea, design of experiment, conducting parts of the experiments, performing major parts of data analysis, writing parts of the manuscript.

[8] **E. Samiei**, H. R. Nejad and M. Hoorfar, " Effect of electrode geometry on droplet splitting in digital microfluidic platforms", ASME-ICNMM2014 August 3-7, 2014, Chicago, Illinois, USA.
Contribution: Development of the idea, design of experiment, conducting parts of the experiments, performing major parts of data analysis, writing major parts of the manuscript.

[9] **E. Samiei** and M. Hoorfar, "Experimental investigation of the possibility of transporting a droplet over a hydrophilic spot in digital microfluidics", Nanotech 2013, Vol. 2, pp 314-317, Washington D.C., USA.
Contribution: Development of the idea, design of experiment, conducting the experiments, performing data analysis, writing the manuscript.

[10] **E. Samiei** and M. Hoorfar, "Modifying Electrode Geometry for Unequal Droplet Splitting in Digital Micro", ASME-IMECE2013 November 15-21, 2013, San Diego, CA, USA.
Contribution: Development of the idea, design of experiment, conducting the experiments, performing data analysis, writing the manuscript.

d. Patent

[1] M. Hoorfar, K. Kim, **E. Samiei**, M. Hampel, A. O'Brien and H. Najjaran, "Integrated Lab-on-Chip Portable Cell Patterning Incubator & Monitoring System", Invention disclosure filled in December 2016.

Table of Contents

List of Tables

List of Figures

List of Symbols

S_d	surface area of droplet
S_d^*	normalized surface area of the split droplet
h	gap height between top and bottom plates
h^*	normalized gap height (divided by the length of the electrode)
n	number of actuated sub-electrodes
r_i	principal radius of droplet interface at the mother droplet side (1 side view, 2 top view)
r_i'	principal radius of droplet interface at the neck (1 side view, 2 top view)
r_i''	principal radius of droplet interface at the sub-electrode side (1 side view, 2 top view)
p	pressure at the mother droplet side
p'	pressure at the neck
p''	pressure at the sub-electrode side
θ_i	apparent contact angle
θ_{adv}	advancing apparent contact angle
θ_{rec}	receding apparent contact angle
θ_{hys}	contact angle hysteresis
U_{rms}	root mean square of the applied voltage
U_{AC}	AC voltage
U_{th}	threshold applied voltage
f	frequency of the applied voltage
σ	interfacial tension between the liquid and the gas phases
w_i	width
L_i	length
γ	aspect ratio
σ_i	electrical conductivity of liquid i

t	time
c	concentration (weight/volume)
C	capacitance
pH	potential of hydrogen (scale of acidity)
ω	angular frequency of the applied field
ε_0	vacuum permittivity
ε_i	permittivity of component i
ε_i^*	complex permittivity of component i
$K(\omega)$	Clausius-Mossotti factor
$\vec{\boldsymbol{F}}_i$	force due to mechanism i
$\vec{\boldsymbol{E}}$	electric field
r	radius
ρ_i	density of component i
$\vec{\boldsymbol{g}}$	gravitational acceleration
Φ	electrostatic potential
$\vec{\boldsymbol{u}}$	fluid or particle velocity
m	mass
x	location
A_{HS}^*	normalized area of the hydrophilic spot
V	droplet volume

Acknowledgements

In the first place, I would like to express my gratitude to my supervisor Dr. Mina Hoorfar for her great guidance and supervision during my PhD career. She has always been a great role model and source of inspiration to me.

I would like to thank my committee members Dr. Najjaran and Dr. Prodanovic for their kind advisory throughout my research. I am also grateful to those who helped me with their greatest knowledge and provided me with their resources, especially Dr. Thomas Johnson who kindly dedicated plenty of his time in advising me.

I am very thankful to all of my friends and colleagues who shared part of their lives with me and created unforgettable memories.

Finally, I would like to express my deepest gratitude to my family who have never hesitated their love and support from me.

This thesis is dedicated to my parents for their endless love and support.

Chapter 1 Introduction[1]

1.1 Lab-on-a-chip and digital microfluidics

In recent years, a prodigious number of studies has been devoted to advance microfluidic devices that can replace the conventional laboratory processes performed by technicians and experts in large scale laboratories [1]. The primary advantages of such devices are automation and reduction of the consumed samples and reagents. In addition, the large surface-to-volume ratio (reducing the reaction time) and high controllability in sample manipulation are the other features of such devices [1]. These advantages have made microfluidic systems suitable for performing biochemical experiments. Following the first attempt in developing a microfluidic system in 1950s [2], several mechanisms have been used to drive and control the flow in microfluidic systems [1]. According to Haeberle and Zengerle [1], the seminal microfluidic systems that have been developed for lab-on-a-chip applications are categorized as: capillary driven test strips [3], pressure driven systems [4], centrifugal microfluidic devices [5], electrokinetic platforms [6], droplet-based (continuous and digital) microfluidic systems [7-9], and non-contact dispensing systems [10]. Despite the common features of these systems, the mechanism of fluid manipulation and the application range of each system are different, and consequently each system has advantages and shortcomings compared to other systems. The review of the aforementioned systems shows that most of these devices have 3D geometries (including pre-etched or machined microchannels/flow passages) and integrated external modules (e.g., syringe pumps and electrical actuators) [3-7] that make the fabrication of the device complicated. Also, in most cases the platform is limited to a certain application, and the

---

[1] Parts of this chapter have been published as a review paper in Lab on a Chip (E.samiei et al., *Lab. Chip.*, (2016) 16, 2376-2396).

device cannot be used for multiple purposes. In addition, the miniaturization of all the assay-processing steps on a single device, required for developing a portable point-of-care device, is difficult. On the other hand, digital microfluidics (DMF) [9, 11-13], which is a droplet-based microfluidic system with a planar geometry can be simply fabricated by photolithography [11, 12]. The fluid manipulation mechanism on these systems (in the form of actuation of discrete droplets) does not require external modules or complicated geometries such as pumps or valves [9, 14]. Another unique feature of DMF is that the actuating electrodes on the chip can be fabricated on a 2D array with a general electrode design, and as a result, a single platform can be reconfigured for multiple applications [11, 12, 15]. The droplet-based characteristics of DMF allows for parallel operations on a platform [16, 17], increasing the speed of assay-processing steps [17]. Furthermore, a significantly high precision can be achieved for sample preparation on such systems [18, 19]. Therefore, DMF has the potential to be further developed for mass production and be merged as a device of choice for point-of-care applications.

Digital microfluidic devices are categorized into open and closed configurations [20-23]. Figure 1-1 shows the schematic of the two DMF configurations. Droplets can be manipulated on DMF using several different techniques such as electrowetting on dielectric (EWOD) [9, 24], dielectrophoresis (DEP) [25, 26], surface acoustic waves [27, 28], magnetic force [29, 30], thermocapillary force [31, 32], optoelectrowetting [33, 34] and magnetic actuation of liquid marbles [35]. Despite the general success of all of these methods, EWOD offers the most flexible and best functionality for droplet actuation, and has been extensively used for lab-on-a-chip applications [11, 12].

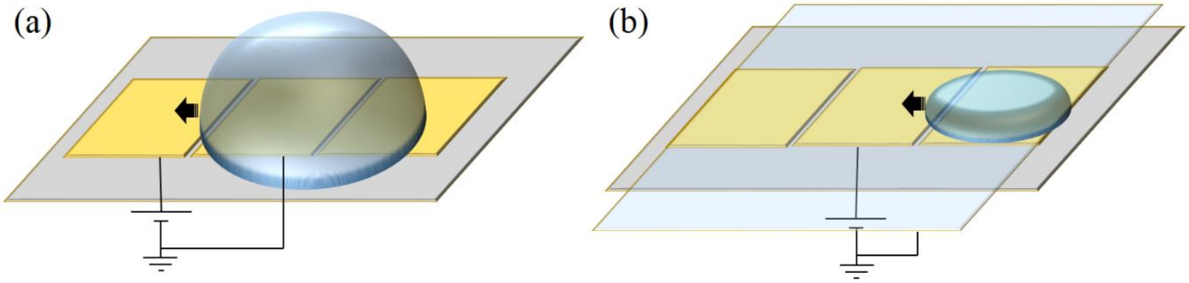

Figure 1-1 The schematic of (a) open and (b) closed DMF systems.

In EWOD-based DMF devices, the electrodes are patterned on a substrate (normally a glass slide or a silicon wafer with thermally grown oxide layer) using photolithography and then covered with a dielectric and a hydrophobic layer [9]. In the closed configuration, the droplet is sandwiched by a top plate which is usually an ITO-coated glass slide used as a transparent electrode, covered with a hydrophobic layer. Droplet manipulation is performed by applying a DC or AC voltage to the system [9, 14]. A detailed review of EWOD can be found in [36] and the references therein.

After the introduction of the primary DMF platforms [9, 37, 38], a large number of studies have been performed on enhancing and advancing these devices for lab-on-a-chip applications. The common purpose of these studies have been to develop a package capable of performing a complete set of operations required for biological assays, and in some cases, develop a portable device for point-of-care applications. Multiple reviews have reported earlier advances for general [11, 39, 40], or specific applications of DMF in areas related to electrochemistry [41], clinical diagnostics [42], cell-based applications [43, 44] and detection or sensing [45]. In this chapter, the most recent and also major timely advances on all aspects of DMF and its applications in lab-on-a-chip devices are reviewed. These advances are categorized into eight major streams including device fabrication, basic fluidic operations, automation, manipulation of biological samples, advanced operations, detection, biological applications and packaging and portability. Each of these streams is thoroughly evaluated to assess the future of the DMF-based devices and their significance in point-of-care applications.

1.2 Overview of digital microfluidics

1.2.1 Device fabrication

1.2.1.1 Substrate

Various substrates have been used for the fabrication of DMF devices. Glass and silicon wafers with an oxidized layer (thermally grown on the surface) are commonly used as the substrate [46, 47]. For the studies including packaging, the DMF chips have been fabricated on printed circuit boards (PCB) [15, 48]. While such substrates are beneficial for non-disposable chips, in recent years there has been a high demand for developing DMF devices with disposable substrates. Paper-based substrates are the most common disposable substrates for chip fabrication [49-53]. Although the quality and resolution of the fabricated electrodes are hindered on these substrates, their low cost and ease of fabrication will allow for replacement of the chip after each round of experiment, and consequently, the chance of cross contamination will significantly decrease. Most studies use screen printing for fabrication of electrodes on the paper-based substrates. Inject printing has also been used for this purpose to enhance the resolution of the fabricated electrodes as well as automating the fabrication process [52]. The applications of these disposable devices were also shown for Immunoassays [53]. Similarly, disposable DMF chips have been fabricated using inexpensive screen printing method on other flexible substrates such as polyimide foils [54]. Other than such flexible substrates, disposable DMF chips have been fabricated using printed circuit boards (PCB) ([55, 56]). Sista et al. [55] used the PCB fabricated device for diagnosing multiple newborn diseases.

1.2.1.2 Electrode

Gold is the most widely used material for the electrodes. However, as adhesion of gold to the substrate is not sufficient, a layer of chromium or titanium is usually deposited as the base layer to increase adhesion of gold to the substrate [57]. Other materials such as ITO [58], chromium [47], sliver, carbon [51] and copper [59] have also been used for pattering the electrodes. While the resolution of the electrode geometry might vary for different materials used for fabrication, the choice of the electrode material does not significantly alter the durability of the device.

1.2.1.3 Dielectric layer

Unlike the electrodes, the choice of material and the quality of deposition for the dielectric layer is very important. The required applied voltage for droplet transport and splitting significantly depends on the dielectric constant of the material, i.e., the higher the dielectric constant the lower the required voltage [36]. Further, uniformity and fineness of the layer is crucial for preventing the dielectric breakdown in applying high voltages or for long actuation periods. The primary studies in literature used the materials such as polytetrafluoroethylene (PTFE) [60], Parylene C [61] and SiO_2 [38]. Parylene C and SiO_2 are the most common dielectric materials due to their stability and uniformity [14, 62]. Their dielectric constant is in a low range of 2-4, and their reported thicknesses are in the range between 0.1-15 µm. The minimum required voltage for droplet actuation is reported as 60-80V for an 800-nm layer of parylene C and ~25V for a 200-nm layer of SiO_2 [24, 62]. However, this is the threshold voltage for droplet motion, while splitting requires higher voltages to overcome the surface tension effect (14). SU-8 and S1813 photoresists have also been used in some studies for their ease of deposition (spin coating). However, they have a low dielectric constant which ranges around 3 [63, 64]. Materials with a very high dielectric constant have recently been used as the dielectric layer for low-voltage droplet transport. Their high dielectric constants prevent dielectric breakdown by requiring low voltage for droplet splitting/dispensing. For instance, droplet actuation with a voltage as low as 15V has been performed with $(Ba_{0.7}Sr_{0.3})TiO_3$ (BST) [65] (with a dielectric constant of ~180) and Ta_2O_5 (with a dielectric constant of 25-40) [66, 67] when they are used as the insulating layer. Such materials with extremely high dielectric constants can be used for EWOD applications requiring a low actuation voltage. However, the necessity of having the hydrophobic layer on the chip as the final layer increases inevitably the required applied voltage [47]. These hydrophobic layers are known to have a low dielectric constant, and hence, the majority of the voltage drop occurs across this layer. Consequently, the minimum actuation voltage and breakdown of the device is limited to the hydrophobic layer coated on the insulating layer [47]. For instance, the minimum required voltage for BST (coated with a hydrophobic layer) is limited to 15V (65, 66). Multilayer insulating layers were shown to function more effectively, and the devices are more durable with a much longer time-dependent dielectric breakdown [47, 68]. For instance, an insulating layer was formed using a layer of high dielectric materials such as Ta_2O_5 followed by a Parylene C and a hydrophobic layer. Thermal treatment of the Ta_2O_5 layer significantly increased the electrical properties and the durability of the device [47]. Most recently, Narasimhan and Park [69] introduced an ion gel material with a high dielectric constant as the insulating layer which can be easily spin coated on the chip surface. The ion gel consists of poly(vinylidene fluoride-cohexafluoropropylene) [P(VDF-HFP)] as the copolymer, and 1-ethyl-3-methylimidazolium bis(trifluoromethylsulfonyl)imide [EMIM][TFSI] as the ionic liquid.

1.2.1.4 Hydrophobic layer

The last layer in the fabrication of the DMF devices is the hydrophobic layer commonly made of fluoropolymer-based materials such as Teflon [14] and CYTOP [19, 47, 68] allowing for droplet transport on the chip [9, 14]. The contact angle reported for water on these fluoropolymers is between 105-117˚. However, when used with ambient oil or silicone oil, a contact angle of up to 180˚ has also been reported [19]. The layer formed by such fluoropolymer is stable enough in aqueous solutions [70]. However, their hydrophobicity is compromised as they become in contact with biological samples such as proteins [70]. This issue will be discussed in detail in Section 1.2.4.

1.2.1.5 Advanced fabrication

In more recent studies, fabrication of the DMF devices with multilayer electrode-connection system has allowed for patterning a 2D array of electrodes without any limitations for the electrical access to the electrodes. In these devices, the connection lines are initially patterned on the substrate. An intermediate dielectric layer is then deposited with patterned holes for accessing the connection lines. On the top of the dielectric layer, the electrodes are patterned which are connected to the connection lines through the holes in the dielectric layer [47, 64, 68]. Printed circuit boards have also been used for multilayer chip fabrication [71], where the electrodes can be patterned on the entire chip, enhancing multiple parallel droplet manipulation. It is also shown that with the use of a thin film transistor array for electrode fabrication, one can make a large number of electrodes in a 2D array with the capability of capacitive droplet sensing for the control of the position and the size of the droplet [72].

1.2.1.6 Integration with other systems

Digital microfluidics has also been interfaced with other microfluidics systems [73-77]. Such hybrid microfluidic devices provide the benefits of discrete format of DMF along with the advantages of continuous microfluidics for sample processing. To interface a pressurized flow within a microchannel with a sandwiched DMF system, Ahamed et al. [73] developed a thermal passive microvalve to control the delivery of the liquid sample from the microchannel into the DMF section of the chip. The microvalve functioned based on EWOD actuation of a thermo-responsive polymer for controlling the flow. Banerjee et al. [76] developed a programmable high throughput hybrid systems including micro-channels interfaced with a DMF platform. In order to achieve the high throughput sample processing platform, while benefiting from the advantages of DMF, parallel channels were fabricated. The device was programmed to generate droplets from the continuous flow through each channel. After processing each droplet, it was transferred and merged in to another channel. Shih et al. [77] interfaced a droplet microfluidic system with DMF for single cell applications. Their device uses the advantages of each system: the droplet microfluidic system is used to generate droplets which encapsulate single cells, and then the DMF system is used for highly controlled manipulation of the formed droplets.

1.2.2 Basic fluidic operations

Manipulation of droplets by EWOD began after the introduction of the technique by Berge [78] who added an insulating layer on the electrodes to separate them from the conductive liquid and prevent the electrolysis problems. A review of early studies on this phenomenon can be found in [79]; a more thorough review on EWOD droplet actuation can be found in [36]. As mentioned earlier, two categories of DMF devices consist of open and closed (sandwiched) systems. While access to the droplet (and sample delivery) is easier on the open system, the closed system allows droplet manipulation (transport and splitting) in a more straightforward manner [21]. Four basic fluidic operations developed on DMF are droplet transport, merging, splitting and dispensing (Figure 1-2) which enable the DMF devices for sample manipulation. Pollack et al. [9] demonstrated that EWOD can be used to transport aqueous droplets on the chip. Droplet splitting and mixing in silicone oil were later introduced [24]. The use of silicone oil facilitates droplet manipulation on the chip as the contact angle becomes larger and the contact angle hysteresis smaller [14]. The four basic fluidic operations were performed and further studied with air as the surrounding medium by Cho et al. [14]. Further improvements in the device fabrication resulted in manipulation of droplets with a voltage in the range of 20V and a transport speed of several cm/s [36]. Use of an AC applied voltage rather than a DC voltage resulted in reducing the contact angle hysteresis and delaying dielectric breakdown [36, 80]. A proper frequency of the applied voltage based on the system properties was also found based on the theory introduced in [81, 82]. Their study showed that applying DC pulses rather than an AC (or DC) voltage can prolong the chip lifetime and increase the velocity of the droplet transport significantly [83].

The primary technique for droplet mixing was moving the droplet back and forth on an array of electrodes which took several seconds [14]. Subsequently, more advanced techniques were developed for faster droplet mixing using enhanced EWOD manipulation of droplets by monitoring the liquid motion inside the droplet [84, 85], rotating the droplet over a 2D array of electrodes [85], and frequency-dependent droplet oscillation [86, 87], reducing the mixing time.

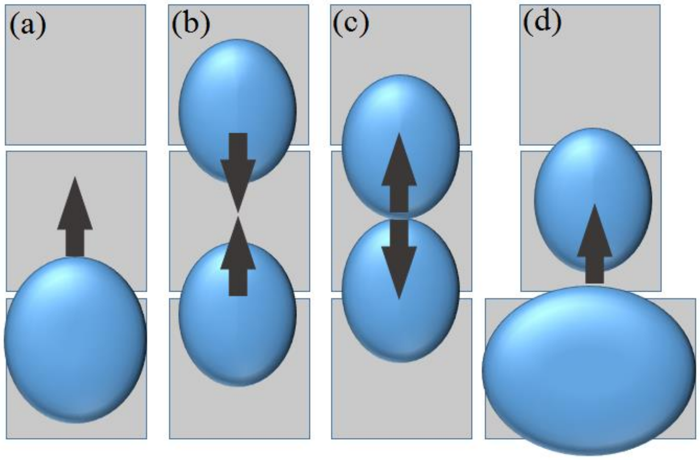

Figure 1-2 Basic fluidic operations on DMF: (a) transport, (b) merging, (c) splitting, and (d) dispensing.

Compared to droplet mixing and transport, droplet splitting and dispensing (from a larger mother droplet as a reservoir) are more challenging, as they require larger applied voltage and are limited to the geometrical parameters of the device [14]. Successful applications of DMF for lab-on-a-chip applications depends on the precision of the device in sample preparation. Therefore, high control on the droplet size is required when droplet extraction or splitting is performed [14, 18]. In general, droplet splitting is carried out on an array of 3 electrodes. The droplet is placed on the middle electrode, and by turning on the two side electrodes, the droplet will pinch and then split [14, 88]. Droplet splitting depends on the gap height between the top and bottom plates, the size of the droplet and the electrodes, and the applied voltage [14]. Berthier et al. [89, 90] developed an analytical model to determine the required voltage for droplet extraction from a reservoir as a function of the gap height. They showed that for a certain size of the electrodes, there is a limit for the gap height for droplet extraction. In recent studies conducted on droplet splitting/dispensing, multiple approaches were attempted to reduce the error of the droplet size to less than 1%. Gong and Kim [18] developed a feedback control and capacitance measurement system (integrated into the DMF device) to control the volume of the extracted droplets by adjusting the applied voltage to the activation electrodes. Banerjee et al. [91] and Liu et al. [19] showed that using a continuous reservoir as well as ramping down the applied voltage to the middle electrode facilitates the generation of precise volumes of droplets.

1.2.3 Automation

Soon after the development of the basic fluidic operations and successful droplet handling on DMF devices, feedback control and sensing systems were integrated to these devices to manage droplet formation and to automate on-chip processes. Image processing [92], thin film [93] and optical fiber [94] based sensing systems have been used for controlling the droplet size and position. However, most of the developed sensing systems for controlling the sample manipulation of DMF devices have been based on capacitance measurement to determine the droplet size and interface position [17, 95, 96]. Multiple studies used the measurement of the change in the capacitance between the top and the bottom plates due to the presence of the droplet to automate sample manipulation [48, 97, 98]. Precise generation of droplet volumes [18, 19] and control of the mixing process [99] have also been performed using these feedback control and sensing systems. In a different configuration, droplet sensing using the co-planar electrodes, i.e., using a pair of actuating electrodes on the bottom plate, has been demonstrated as an accurate way to monitor the droplet size and position [100-102].

For parallelization on DMF devices, it is necessary to efficiently allocate sites on the chip for droplet storage and manipulation, and identify the motion paths for performing a large number of assay-related operations on a 2D array of electrodes. Böhringer [16] presented multiple algorithms for automating the parallel tasks performed on the chip. These algorithms include the task and motion planning for manipulation of several droplets simultaneously, as well as approaches to transfer the laboratory protocols to control commands compatible with DMF systems. Despite the general success of these algorithms in providing efficient solutions for performing parallel operations, they were not able to identify the optimum solution due to a high number of possible processes on a 2D array of electrodes. Taking advantage of the strategies used in very-large-scale-integration (VLSI) design for wire routing, Su et al. [103] developed a routing technique for droplet manipulation on DMF systems to minimize the number of electrodes used for the parallel processes to achieve a high throughput device. In this study the physical constraints imposed by the liquid and chip (such as the minimum distance between droplets to avoid accidental coalescence) were also taken into account and the developed algorithm was tested experimentally. This method resulted in identifying the maximum number of parallel operations that could be achieved with a given number of electrodes. In a different study conducted on parallelization on DMF systems a Connect-5 structure of the pin configuration was used to control the droplet paths to minimize cross-contamination between droplets [104]. This method can also identify the optimum solution for performing parallel operations. The application of such parallelization strategies have been shown for PCR [105] and cell-based [106] applications considering the cross contamination issues and routing optimization. Such advances in parallelization, along with the developed feedback control and sensing systems provide the capability of developing high throughput DMF-based platforms for performing multiple biochemical assays.

1.2.4 Manipulation of biological samples

When handling aqueous and non-biological samples, the hydrophobicity of the surface of the DMF devices prevents any residue of the samples on the chip and consequently there is no, or negligible cross contamination even in numerous cycles of droplet manipulation. On the other hand, handling biological samples leaves permanent traces on the hydrophobic surface of the chip, resulting in cross contamination and hindering further sample manipulation [70]. This is mainly caused by hydrophobic adsorption and electrostatic interaction of the molecules such as proteins and lipids with the hydrophobic layer (deposited on the electrodes), which makes the surface permanently hydrophilic [70].

Multiple techniques have been developed to prevent or limit molecular adsorption to the surface of microfluidic devices with more or less success. In the first attempt, developed by Yoon and Garrell [107], the pH of the sample, as well as the frequency, magnitude and the actuation period of the applied voltage were controlled to minimize the molecular adsorption on the surface. The use of silicone oil to insulate the sample droplet from the chip surface was another strategy used for EWOD actuation of body fluids such as whole blood [108]. This method was successful for transporting a blood droplet over thousands of cycles without surface contamination. However, sample contamination and subsequence detection of the targets can be a great concern [109]. Bayiati et al. [110] used plasma deposition technique instead of spin coating for the hydrophobic fluorocarbon deposition on the DMF chip and studied the decrease in the contact angle upon applying the voltage. A significant reduction of surface contamination could be achieved with plasma deposition method, shown after the solutions containing proteins was incubated on the device for 5 minutes. In another study, protein adsorption onto the surface was investigated in the presence of a low concentration of Pluronic F127 [70]. The sample observation by confocal microscopy and mass spectrometry allowed to conclude a reduced non-specific adsorption of proteins though a concentration of protein as high as 1mg/mL was used. The mechanism for such antifouling effect was hypothesized to be the formation of a Pluronics layer at the liquid phase boundary, similar to that reported for the use of silicone oil. Yang et al. [111] developed a strategy based on disposable polymer skins: after each experiment the top layer is removed and a new layer is replaced to eliminate cross-contamination and solve the device breakdown problems. Despite the ease of this technique, it is not practical for point-of-care applications as the manipulations are required to be performed in a cleanroom and the device should be assembled by well-trained personnel. Generating nanostructured super-hydrophobic surfaces is another method used for preventing surface biofouling [112, 113]. The super-hydrophobicity of the surface significantly decreases adsorption of biomolecules to the surface, providing anti-biofouling properties. Prakash et al. [113] successfully used a DMF platform equipped with such a nanostructured super-hydrophobic surface for PCR detection of Influenza virus.

1.2.5 Advanced operations

Basic fluidic operations (droplet transport, merging, splitting and dispensing) are the key to the functionality of the DMF devices for performing biochemical applications. However, performing complete biological assays on such devices will not be feasible only by basic fluidic operations. The implementation of some strategies or integration of modules into the chip has to be considered for advanced operations or processes such as cell manipulation, particle binary separation, heating and biochemical sensing. For some operations such as particle manipulation, the DMF setup does not require reconfiguration. Only by modulating the applied voltage to the electrodes, the operations can be carried out. Conversely, for multiple other advanced operations the geometry of the planar electrodes has to be modified or some external modules should be integrated according to the electrical, optical, and biochemical properties of the sample and the chip.

One of the advanced and essential operations is the ability to dispense a different range of volumes of samples or split a mother droplet into two unequal (volume) daughter droplets. This operation is important for particle and cell separation/concentration [114, 115] or sample dilution [46, 108] for which the use of equal droplet dispensing or splitting requires several repetitions, increasing significantly the process time and errors in the final product [18]. In [18] voltages of different amplitudes were applied to the actuating electrodes and by controlling the applied voltage, variable droplet volumes were dispensed from a reservoir: the volume of the dispensed droplets was controlled by a capacitive sensing and feedback control system.

Manipulation of micro-particles and cells inside the droplet has been performed in multiple studies for applications such as particle focusing [116], patterning [59] and separation [117, 118]. These techniques have been mostly applied to microbeads which are important in several biological applications [119-122]. Similar strategies can be adopted for the manipulation of cells and biomolecules, such as optoelectric driven cell manipulation presented by Shah et al. [123] and cell patterning and encapsulation by Nestor et al. [124]. The particle manipulation techniques developed for DMF function based on optical [123], magnetic [125-127], hydrodynamic [116, 128], electrophoretic [129] and dielectrophoretic [59, 114, 130] properties of the particles and or the medium (droplet). Zhao et al. [118] used a traveling-wave dielectrophoretic technique to separate two types of particles by controlling the frequency of the applied voltage. In another study, magnetic beads were collected in one side of the droplet using an external magnet, and then the droplet was split. This allowed for concentrating over 90% of the beads in one of the split droplets [117]. Focusing non-buoyant particles in a micro-droplet using a hydrodynamic-gravity driven method was performed in [116]. Electrophoretic separation of one type of particles along with the binary separation of two different types of particles with opposite charges was also performed in [129].

Sista et al. [131] and Li et al. [132] reported the integration of a heater into the DMF platform for the thermal control of the assays. The heaters are patterned on the chip similar to the method used for electrode fabrication. In essence, a thermal element is formed by a metal layer, and heat is generated by passing a controlled electrical current through the electrode.

1.2.6 Detection

Sensing or detecting a biological event on the chip is an important and inseparable part of any biochemical assay. Numerous investigations are dedicated to develop detection systems being used with DMF platforms. A review of detection on DMF systems was performed by Malic et al. [45]. While the majority of the approaches are based on fluorescent microscopy [133], other techniques such as mass spectrometry, chemiluminescence and electrochemical systems have also been used for detection of targets on DMF. As such, these methods can be categorized in optical, electrochemical and mass spectrometry according to their sensing mechanisms. They can also be classified based on their mode of detection, i.e., off-line (or off-chip) and on-line (or on-chip) detection [45]. While the off-line mode is suitable for in-lab uses, on-line systems are beneficial for packed and portable devices for point-of-care applications.

Regardless of the transduction mechanism (electrical, electrochemical, optical and mechanical), all biosensors require the modification of their sensing surface by functionalizing it with selective bio-receptors as biological recognition elements. Based on the surface modification techniques, biosensors can be categorized [134] as enzyme-based [135-137], antibody-based [138, 139], and aptamer-based [140-142] biosensors. A review of different surface modification techniques for biosensors integrated into microfluidic devices can be found in [134]. Implementing similar techniques for surface functionalization, many biosensors have been developed for DMF devices which are covered in this section.

Off-line detection based on optical methods [143] (such as fluorescence [111, 144, 145], absorbance [125, 146], and chemiluminescence [125]) along with mass spectrometry [147-149] are major sensing techniques to analyze samples extracted from DMF platforms. Label-free optical detection such as surface plasmon resonance (SPR) [150, 151] has also been used. The reason behind the popularity of the off-line methods is that the required equipment is readily available in most of laboratories for biochemical or cell-based assays [46, 57, 152].

As for the on-line detection, the conventional design and configuration of the detection systems have to be modified to miniaturize them for integration into the DMF devices. Examples are fluorescence detection for the polymerase chain reaction (PCR) [131, 153], proteomics [154] and enzymatic assays [152]. Other optical methods such as chemiluminescence [125, 131, 155] and absorbance [58, 108] have also been integrated into DMF devices. The requirement for this integration is to leave the top or the bottom plate transparent (e.g. the use of ITO as the electrode) in order to have optical access to the sample. An electrochemiluminescence technique was used on a DMF device for the detection of single nucleotide mismatches of microRNA-143 (miRNA-143) in cancer cell lysates with a high sensitivity [156]. Similarly, miniaturized SPR biosensors have also been integrated into DMF [157-159]. A detection limit as low as 5 pM was achieved for the DNA hybridization (176). Multiple studies report on the integration of mass spectrometry detection system into DMF [160-163]. Interfacing between DMF and liquid chromatography-mass spectrometry has further been demonstrated in [164]. A major issue with such systems is that they cannot be miniaturized for complete integration into DMF, and hence the on-line detection mode has been performed by interfacing these systems to DMF for real-time detection [45]. Unlike the optical and mass spectrometry detection systems which require external devices (light source, photo detector, etc.) to be integrated into the chip, the electrochemical sensing systems can be patterned and directly integrated into the DMF chip along with the actuating electrodes with a very easy and straightforward fabrication method [165, 166]. An example of such systems is shown in Figure 1-3 in which the three-electrode sensor is used for the detection of different concentrations (down to 500 nM) of ferrocenemethanol (FcM) and dopamine (DA) [165]. One main problem associated with the integrated biosensors into DMF is the hydrophilic nature of their sensing surface, which hinders droplet actuation. Multiple studies addressed such a problem by limiting the size of the sensing surface to minimize the amount of the sample liquid left on the biosensor [157, 165]. Recently, integration of a field effect transistor (FET) biosensor into DMF was performed. The results showed that the FET biosensor is a highly selective and sensitive on-chip detection method for such an ultra-small scale [139]. The high selectivity and sensitivity, along with the miniaturized geometry are the features that are pursued for the development of many label-free nano-biosensors, particularly for electrical- and optical-based sensors. The ultra-small size of these sensors along with the use of biological receptors immobilized on their surface make them very attractive for the fabrication of an array of sensors [167] for multiplexing and for integration onto DMF. A review of the label-free biosensors can be found in [168].

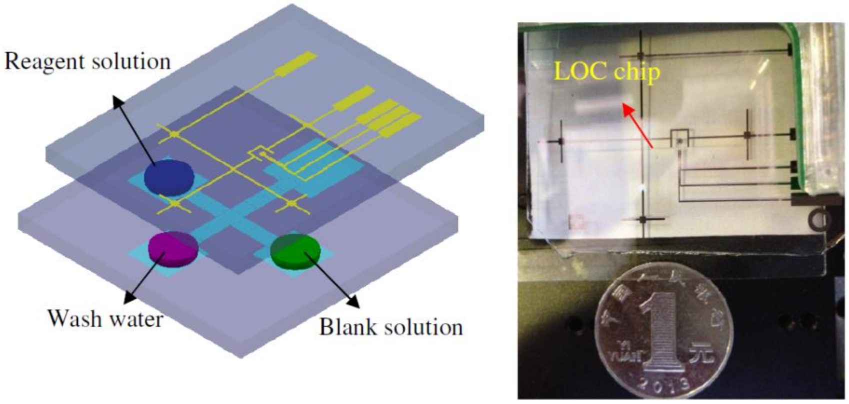

Figure 1-3 Integrated electrochemical detection electrodes fabricated on the top plate of a DMF setup. (Reproduced from [165] with permission from Institute of Physics Publishing).

1.2.7 Biological applications

Since the introduction of DMF, the remarkable functionality of these devices and their high controllability regarding sample manipulation motivated the development of devices compatible with various biological applications [11, 45, 169, 170]. In general, these applications can be categorized as clinical diagnostic applications, enzymatic assays, tissue engineering and cell-based applications, DNA-based applications, immunoassays and proteomics [45].

For the clinical diagnostic applications, DMF was employed in some studies only for partial sample preparation (e.g. for detecting Mycoplasma DNA [171]), and in several studies, it was further developed for performing a larger portion of the diagnostic assay for lysosomal storage diseases [172, 173], dried blood spot (DBS) analysis [174] and estradiol detection [175]. In the study conducted by Ng et al. [176], a complete sample preparation was performed on the chip for the detection of rubella infection and immunity, and the chip was placed under a chemiluminescence device for detection. For this purpose, rubella virus immobilized on the magnetic beads were used for capturing the analyte from the sample. Specific antibodies with linked enzymes were used for generating the chemiluminescence signal upon antibody-analyte binding. Most recently, Li et al. [177] developed a DMF package for multiple detection from the extracts of DBS for point-of-care applications. In this study, the entire sample preparation and detection processes were performed on the DMF using colorimetric and fluorometric techniques.

DMF has widely been employed for chemical and enzymatic assays for analysis of the reaction kinetics and developing new compounds. The notable enzymatic assays were performed for glucose detection [58], environmental applications [178], diagnostics [179], studying the kinetics of reactions [152, 160], synthesis of new compounds [180, 181], and chemical synthesis [182, 183]. Several studies have been conducted for DNA-based assays such as DNA purification [184, 185], detection of DNA hybridization [186], DNA sequencing [187], and PCR [188].

Application of DMF in tissue engineering and cell-based assays has been reported in multiple studies [189-193]. DMF was used in [189] for cell culture in which a DMF device is developed with the capability of performing a complete set of processes for mammalian cell culture. A DMF device was also developed with a microwell array for trapping single non-adherent yeast cells in femtoliter droplets which was used for cytotoxicity assays [192]. Bender et al. [194] used DMF for performing cell invasion studies for spheroid-based invasion assays. They showed human fibroblast spheroids invade collagen gels, and one can improve or hinder their invasion by delivering exogenous migration modulating agents.

Immunoassays have extensively been performed using DMF systems [195, 196]. Multiple particle-based immunoassays were performed on a DMF platform [197]. The assay includes parallel 17β-estradiol (E2) and thyroid stimulating hormone (TSH) immunoassays using magnetic beads followed by chemiluminescence detection of the analytes using a well-plate reader.

DMF has also been widely used for proteomics [196, 198, 199]. Luk et al. [200] used enzyme immobilized hydrogels patterned on a DMF chip as microreactors for proteolytic digestion. In this study cylindrical agarose discs were used as a platform for immobilizing trypsin and pepsin used for proteomic digestion, and mass spectrometry was used to analyze the assay products. Mok et al. [199] developed a DMF platform for protein biomarker detection for quantifying protein abundance and activity. In this study, interleukin-6 abundance and Abelson tyrosine kinase activity were quantified with a detection limit as low as 50 pM for interleukin-6 and 100 pM for kinase.

1.2.8 Packaging and portability

The devices developed by Gong et al. [48] and Gong and Kim [15] are likely the earliest attempts for a portable DMF package. A 2D array of electrodes was fabricated using a multi-layer printed circuit board (PCB) and used land grid array sockets for packaging the system. Although they performed multiple fluidic operations, these devices lacked a detection system required for biological applications. Sista et al. [131] fabricated a portable DMF platform, capable of performing immunoassays, enzymatic assays and DNA amplification. The device had a PCB chips and integrated reservoirs for sample delivery using a pipette as well as waste buffer removal. Magnetic and heating units required for performing the assays were embedded in the chip deck. Optical detection was integrated using chemiluminescence detection and fluorimetry units. Finally, an electrical controller unit was integrated into the device for controlling the on-chip processes. This study showed a successful attempt in developing a DMF-based portable package for point-of-care applications. Similarly, Kim et al. [201]

fabricated a DMF hub for DNA applications with a capillary-based interface for straightforward sample delivery to and from the hub. Most recently, Millington et al. [177] reported a portable device with the capability of performing different biomarker assays on the extracts of a DBS. Most recently, a prototype of a smart-phone-controlled low-cost portable DMF platform was fabricated with integrated chemiluminescence detection system [202]. A controller was integrated into the device to enable droplet manipulation as well as on-chip chemiluminescence detection using a smart phone.

1.3 Motivation

After reviewing the main recent progresses and advances made in DMF technology, the development of a DMF platform capable of performing the entire assay processes (from sampling to sensing) is still under question. Certainly, for applications such as clinical diagnostics, enzymatic assays and immunoassays, this goal is achievable but certain obstacles in the areas of sample manipulation, detection, and portability must be overcome. The aspects related to fabrication, basic sample manipulation, and automation are well advanced in the field. For instance, high-resolution chips with the electrodes as small as 21µm, capable of droplet formation with a volume as small as 5pL have been reported in [68]. Other robust fabrication techniques such as micro-contact printing [203] have also been well developed for patterning different substrates. Conversely, multilayer chip fabrication has provided a large number of electrodes in a 2D array resulting in a high throughput platform [72]. Significant advances have been made in regards to control algorithms permitting full automation and parallelization on DMF devices [16]. Despite these advances, there are still aspects of the DMF technology for which further studies are required to promote this technology for performing the entire assay processes. While several studies have used off-line detections tools for biosensing on DMF, a limited number of studies show on-chip biosensing [45]. Therefore, DMF can benefit from the integration of recently developed electrochemical biosensors. For on-line detection methods, the sensing surface of the sensor (functionalized with biological receptors) is in direct contact with the sample. This requires the removal of certain parts of the hydrophobic layer on the DMF device [45, 159]. This consequently limits droplet manipulation. In essence, there are two main challenges associated with the integration of biosensors into DMF that need to be addressed: 1) sample removal from the hydrophilic surface of the biosensor; and 2) biochemical regeneration of the biosensor (detaching the target analyte from the receptor) after each round of sensing. While the latter is case dependent and the remedy can vary from one application to another, the solution found for the former problem can be applied to all types of biosensors. There are a few studies addressing this issue [139, 159, 165]. However, there is a need for a systematic study to characterize the biosensing surfaces and find an optimum solution for droplet removal after the detection process.

While biosensing is a very important part of the biochemical assays on the DMF devices, prior to that sample preparation has to be performed. This includes accurate manipulation of different samples, proper mixing of different samples and reagents, and manipulation of the cells and microbeads inside the droplets. The current droplet dispensing method is not efficient enough, as the size of the dispensed droplets are limited to the size of the actuating electrodes. This will be problematic for the cases in which different volumes of samples are to be mixed. Therefore, developing a robust method for accurate generation of a wide range of the volumes of samples will promote DMF for enhanced operation of biochemical assays.

The mixing process is also a very important part of the biochemical assays, and the efficiency and speed of the biochemical reactions are a function of the mixing process. The current mixing method which is widely used on DMF is based on the cyclic transport of the droplet over a 2D array of electrodes [84]. This might be time consuming in some cases, and the process occupies a portion of the chip (the 2D array). Also, multiple cycles of droplet transport over the chip increases the chance of cross contamination and also chip breakdown. Therefore, DMF can benefit from a more rapid and stationary mixing method.

Currently, there are a few methods for cell and microbead manipulation and concentration on DMF and all of them are limited to the geometrical modification of the chip or adding external modules, such as magnets, to the chip [116, 125, 127]. This requires specific spots on the chip for particle/cell focusing, and the range of application is limited to the geometrical design of the operator. Also, magnetic methods require the manipulation of an external magnet which might not be sufficiently compatible with the size of the DMF devices. This also hinders the automation of the process. Therefore, the development of a method without such limitations for concentrating cells and microbeads will be beneficial for automated and high throughput DMF devices.

1.4 Objectives

This thesis aims at the development of advanced operators to improve sample preparation, on chip biosensing, and post biosensing droplet removal (see Figure 1-4). This includes development of techniques for i) accurate sample dispensing with a wide range of volumes, ii) rapid and efficient mixing of the droplet content, iii) pre-concentration of micro-beads and cells and iv) characterizing and optimizing the geometry of the integrated biosensors for post sensing droplet removal. Such techniques will improve the entire sample preparation and post sensing droplet removal. Primarily, a technique was developed for accurately dispensing variable volumes of droplets, which is based on the geometrical modification of an actuating electrode, and does not require any feedback control or sensing system (see Step 1 in Figure 1-4). This technique is favorable for sample preparation in which different volumes of samples and reagents are to be mixed accurately. Mixing is a crucial process for sample preparation which is frequently used in biochemical assays. An electrohydrodynamic technique has been developed for rapid mixing within the stationary droplets (Step 2 in Figure 1-4). The developed technique provides proper mixing within the droplet in a fraction of a second and eliminates the need for cyclic transport of the droplet over a 2D array of electrodes. Therefore, the durability of the chip will be enhanced and the chance of cross contamination will significantly decrease. For the concentration and manipulation of cells and microbeads inside the samples a dielectrophoretic-gravity-driven (DGD) technique has been developed, which does not require addition of any external modules to the device or geometrical modification of the chip (Step 3 in Figure 1-4). Sample manipulation using DGD can therefore be performed at any spot on the chip only by modulating the frequency of the applied voltage.

A capacitive biosensor has been developed and integrated to the DMF platforms, and biosensing has been performed by the detection of different concentrations of *Cryptosporidium* (as a proof of concept). Since the hydrophilic nature of the biosensors hinders droplet removal from their surfaces, a systematic study has been performed to characterize these hydrophilic surfaces, and some strategies have been developed for optimized designing the biosensing surfaces, for successful droplet removal after biosensing (Step 4 in Figure 1-4). Finally, all the developed techniques have been used for a biosensing assay on a DMF platform for the detection of different concentrations of *Cryptosporidium*.

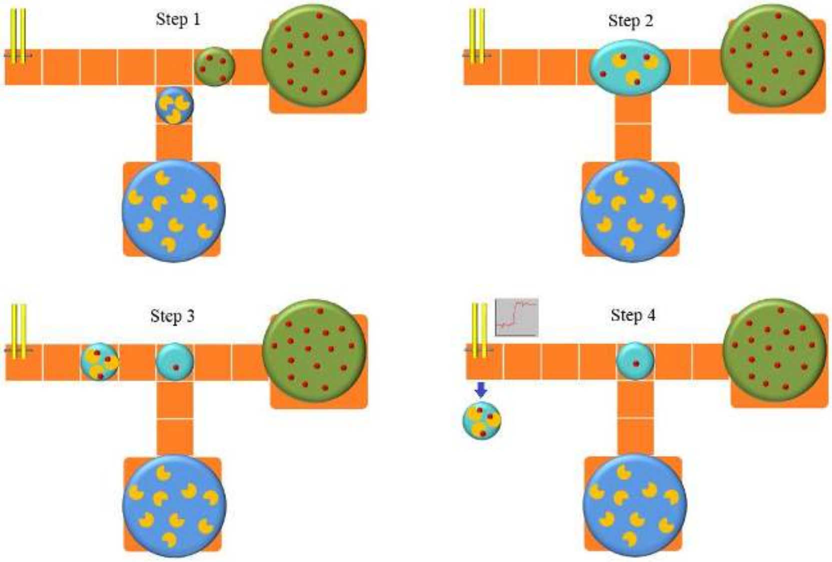

Figure 1-4 Schematic of the steps of the objective operators. Step 1) accurate dispensing samples with desired volumes. Step 2) rapid and stationary mixing inside the merged droplet. Step 3) concentrating the analytes to one side of the droplet, followed by splitting the droplet. Step 4) removal of the sample from the biosensor after detection.

1.5 Thesis organization

This thesis is comprised of 8 chapters which are organized as follows:

Chapter 1: A review of digital microfluidics (DMF) has been presented. The advantages and the shortcomings of this technology was discussed, and the objective of the present thesis was presented.

Chapter 2: The experimental setup, the equipment and the steps used for performing the experiments are presented. Afterwards, the fabrication methods for different components of the DMF platform used for the experiments are explained.

Chapter 3: The details of the developed technique for accurate dispensing and splitting variable volumes of droplets are explained. This method is based on the geometrical modification of an actuating electrode, and provides a wide range of droplet volumes with an over 99% accuracy.

Chapter 4: This chapter explains the electrohydrodynamic technique developed for rapid mixing inside the stationary droplets on DMF. This technique is based on the modulation of the frequency and the amplitude of the applied voltage and does not require any modification of the chip or additional external modules. The main advantages of this technique are the high mixing rate and the elimination of the need for cyclic transport of the droplet over a 2D array of electrodes.

Chapter 5: The dielectrophoretic-gravity-driven technique developed for manipulation and concentration of the microbeads and cells inside the sample droplets is presented. This technique also functions based on modulating the frequency and amplitude of the applied voltage to the electrodes, and can isolate over 90% of the beads/cells inside the droplet. This method can again be performed on any conventional electrode on the chip and does not require the addition of any external module to the chip.

Chapter 6: This chapter presents the systematic study on the characterization of the hydrophilic surface of the biosensors and optimizing their geometry for successful droplet removal after biosensing. The optimized geometry is used for the development and integration of a capacitive biosensor to DMF for the detection of different concentrations of *Cryptosporidium*. The droplet removal after biosensing is successfully performed.

Chapter 7: In this chapter, all the techniques and strategies developed in this thesis were used together for the detection of two different concentrations of *Cryptosporidium* (as a proof of concept) on a DMF platform to show their applicability in the enhancement of the biochemical assay processes.

Chapter 8: Finally, the summary and a list contributions, and the suggestions for future studies are presented.

Chapter 2 Experimental setup and device fabrication

This chapter explains the experimental setup, equipment, the procedures used for performing the experiments, and the different processes used for the fabrication of the devices used for the tests.

2.1 Experimental setup

The studies performed in this thesis are based on the manipulation of the droplets of samples on DMF devices. Therefore, a setup including the DMF chip and the equipment used for the actuation and visualization was used to carry out the experiments. For the cases requiring the characterization of the surface properties, contact angle measurement was performed which required a different setup for actuation and modifications to the imaging system. For the case of biosensing, the sample preparation was performed on the DMF setup, and then the chip was moved to a probing station for performing the biosensing process.

2.1.1 Digital microfluidics

Figure 2-1 shows the schematic of the DMF experimental setup. The DMF device is a closed system, including the bottom and the top plates for most of experiments, and for some other tests, the open system is used which only includes the bottom plate. The bottom plate contains the actuating electrodes, covered with an insulating and a hydrophobic layer, and is fixed on a linear translation stage (Newport Corp.). The top plate is a glass slide covered with a transparent electrode (Indium-Tin Oxide) and a hydrophobic layer placed over the bottom plate, separated either using a pair of spacers (tapes with known thickness) or attached to a manual vertical motion control stage. The applied voltage for droplet actuation is an alternating (AC) voltage generated by a signal function generator (Tektronix AFG 3021B0), amplified to the desired magnitudes using an amplifier (TREK PZD700). An Arduino micro-controller based circuit (Arduino Nano Version 3.0) is used to convert the single output from the amplifier to 40 outputs with individual on/off control for automated actuation of up to 40 electrodes. For the experiments requiring manual actuation, a similar convertor is used with manual control on the output signals. The electrical connection between the controllers and the DMF chips is achieved using edge connectors. A camera with the resolution of 2592×1944 pixels connected to an Apo-zoom microscope (Leica Z6 APO) was used for acquiring the top-view images and videos of the experiments.

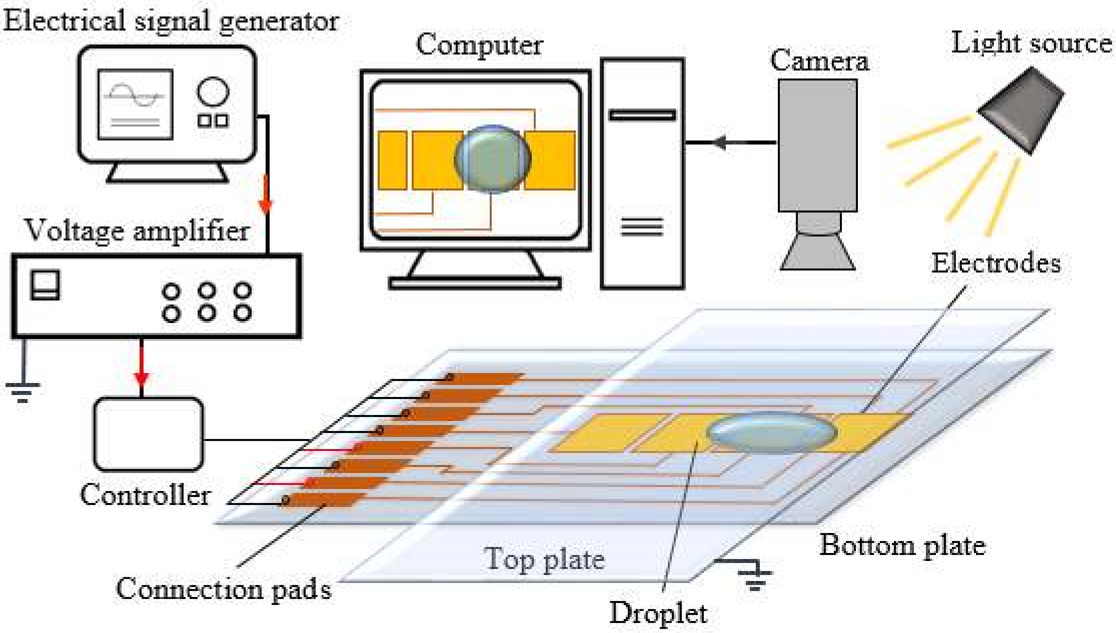

Figure 2-1 Schematic the DMF experimental setup.

2.1.2 Contact angle measurement

The wettability of the surfaces is determined by contact angle measurement [204]. The advancing (θ_{adv}), the receding (θ_{rec}), the change in the receding ($\Delta\theta_{rec}$), and the difference between the advancing and receding (θ_{hys}, contact angle hysteresis) contact angles are used for the comparison of the surface properties. An experimental setup shown in Figure 2-2 is used for the contact angle measurement. Using a syringe pump (KDS LEGATO 270, KD Scientific) water is injected on to the surface through the needle (with hydrophobic surface) in multiple steps. For each step, a volume of $100\ \mu L$ is injected. After each injection the contact angle is measured from the side-view image. The process continues until the contact angle does not change anymore; at that stage the measured contact angle is presented as θ_{adv}. Afterwards, the liquid on the surface is taken back into the needle using the same approach. The contact angle continues to decrease while the three-phase contact line pins on the surface. At the verge of the motion of the three-phase contact line, the contact angle measured is defined as the initial receding contact angle (θ^*_{rec}). The receding contact angle continues to decrease by further removal of the liquid until its value reaches a plateau, which is defined as the final receding contact angle (θ_{rec}). The change in the receding contact angle is calculated as $\Delta\theta_{rec} = \theta^*_{rec} - \theta_{rec}$. The contact angle hysteresis is also calculated by subtracting the receding from the advancing contact angle, $\theta_{hys} = \theta_{adv} - \theta_{rec}$.

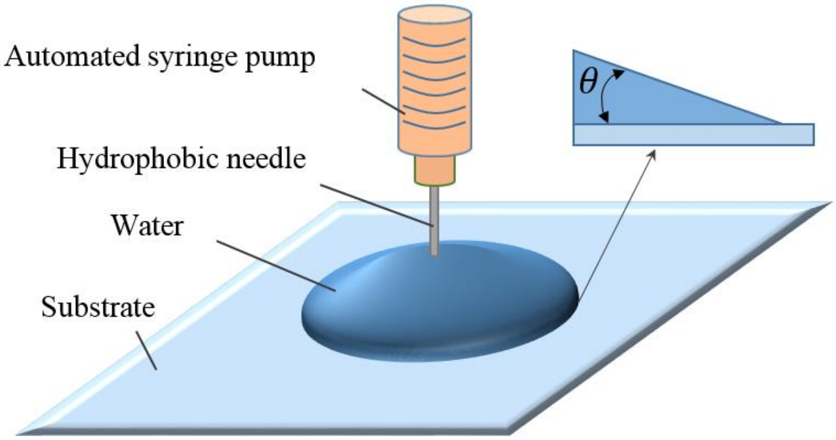

Figure 2-2 Schematic of the contact angle measurement setup.

2.1.3 Capacitive biosensing

For the detection part of the study, the biosensor was patterned on the top plate of the DMF setup to perform on-line biosensing. Therefore, the top plate containing the transparent electrode was replaced with a glass slide containing the patterned ground electrodes used for droplet actuation and the capacitive biosensor (Figure 2-3a). The capacitive measurement is performed using a network analyzer (N5241A, Agilent Technologies). The connection of the network analyzer was performed using Z-Probes (Cascade Microtech) on a probe station (Figure 2-3b).

2.2 Device fabrication

The processes used for the fabrication of the devices include substrate preparation, conductive layer deposition, electrode patterning, dielectric layer deposition, hydrophobic layer deposition, selectively hydrophobic layer removal, and biosensing surface functionalization. To avoid contamination of the chip and achieve the highest possible resolution, all the fabrication processes were performed in a class 100 cleanroom.

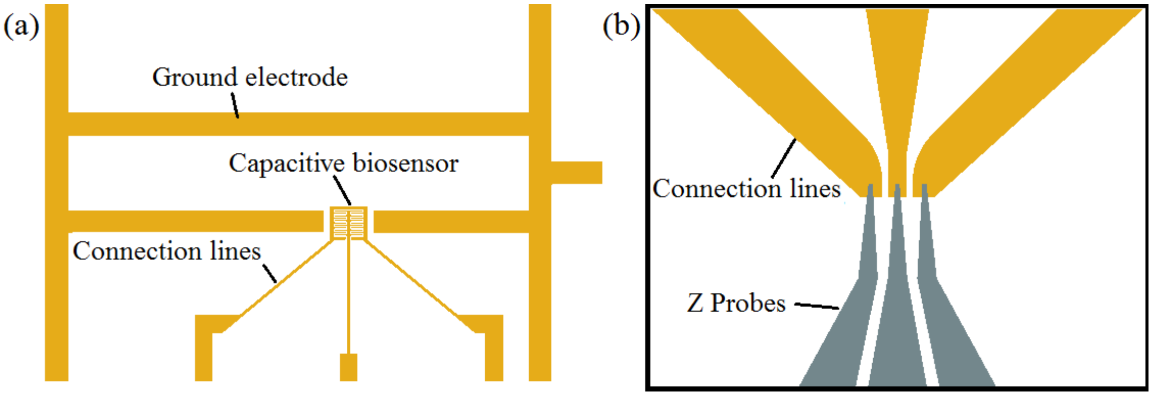

Figure 2-3 (a) Schematic of the top plate containing the patterned ground electrodes and the capacitive biosensor. (b) Schematic of the probing for the capacitive measurement.

2.2.1 Substrate preparation

The substrates used for chip fabrication are $38mm \times 75mm$ or $50mm \times 75mm$ glass slides (Corning Inc.). The substrates were initially wiped with particle-free cloth soaked in acetone (Sigma Aldrich Co.) and then rinsed with a stream of acetone for $10s$ using a squirt bottle. Following that the substrates were rinsed with ethanol and isopropanol (Sigma Aldrich Co.) each for $10s$, and dried using a high pressure air stream. After drying with air, the substrates were baked on a hot plate at $200℃$ for $15\ min$ to remove all washing agents. Prior to the fabrication process, the substrates were treated using oxygen plasma (PM313, Plasma Etch Inc.) to increase the surface adhesion for the subsequent depositions.

2.2.2 Conductive layer deposition

For majority of the devices, gold was used for the fabrication of the electrodes for the DMF and biosensing chips. However, since the adhesion of gold to the substrate is very weak, a chromium layer was primarily deposited to increase the surface adhesion for the deposition of the gold layer. The chromium and gold layers were consecutively deposited on the substrate using a magnetron sputtering system (Angstrom Sciences Inc.). For some devices copper was used as the conductive layer to fabricate the actuating electrodes. For these devices, commercially available copper coated slides were purchased (CU134, Evaporated Metal Films Corp.). ITO coated glass slides (SiO_2 passivated, Rs = 4–8 V, Delta Technologies LTD) were used as the transparent top plates.

2.2.3 Electrode patterning

The electrodes were patterned on the slide using standard photolithography: first, a layer of photoresist S1805 (MicroChem Corp.) was spun on the copper layer at the speed of 3000 rpm for $60s$ and baked for $2\ min$ at $95°C$. Then, the slide aligned with the mask containing the design was exposed to the UV light (365 nm wavelength) for 6s. This was followed by placing the substrate in MF-319 developer (MicroChem Corp.) for 30s. For the case of copper, a diluted solution of ferric chloride was used as the copper etchant to pattern the electrodes. For the case of chromium-gold, the electrodes were patterned using chromium and gold etchants. The remaining of the photoresist on the slide was then removed using acetone and the substrate was rinsed with deionized (DI) water. The schematic of the process is shown in Figure 2-4.

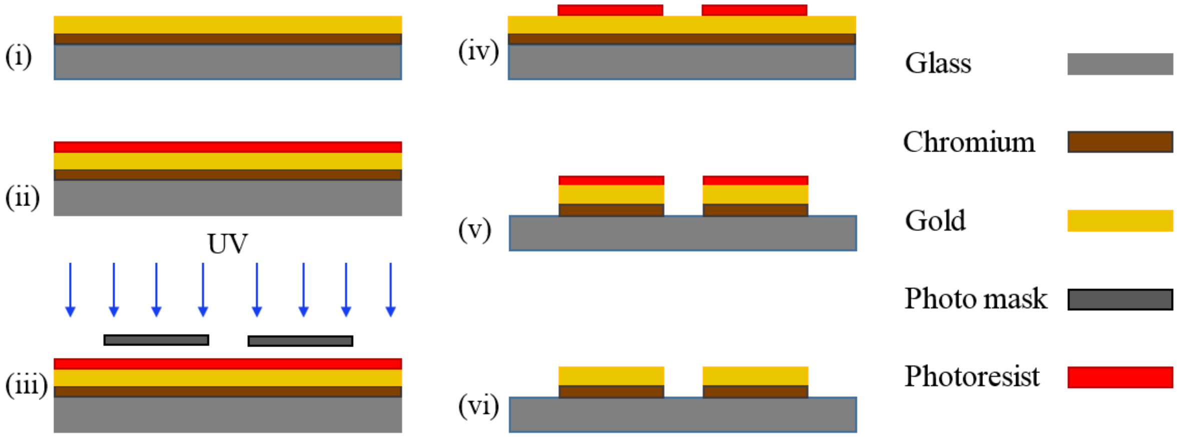

Figure 2-4 Schematic of the photolithography process.

2.2.4 Dielectric layer deposition

In electrowetting-on-dielectric (EWOD) DMF devices, the actuating electrodes are coated with a dielectric insulating layer. Two types of dielectric materials were used here as the insulating layer: photoresist and parylene C. For the case of photoresist, two layers of S1805 and S1813 photoresists were spun (2000 rpm for 60s) consecutively to make a dielectric layer on the patterned electrodes. In essence, the photoresist was used as the dielectric layer as it can simply be deposited using a spin coater. S1805 was first coated to make a uniform layer on the substrate. Then, the S1813 layer was applied to provide enough thickness for the dielectric layer. Each of the layers was post baked for $30\ min$ at $95°C$. The thickness of the combined layer is approximately $2.5\ \mu m$ ($650\ nm$ for S1805 and $1850\ nm$ for S1813). The dielectric constant of the combined photoresist layers was determined using the impedance measurement (VersaStat 4, AMETEK Corp.), and the value is estimated as $\epsilon = 2.54$.

Parylene C was also used as the insulating layer which provides a more uniform and durable layer than photoresist. A parylene deposition system (SCS Labcoater® 2) was used to deposit the parylene C layer on the substrate. The thickness of the layer was controlled by the weight of the parylene C dimer. For every $1\mu m$ thickness of the layer, $1.2g$ of dimer should be used (based on the SCS Labcoater® 2 catalogue).

2.2.5 Hydrophobic layer deposition

The final layer in EWOD-based DMF devices is the hydrophobic coating, which enables transport of the droplet on the chip surface. Two types of fluoropolymer-based materials were uses as the hydrophobic layer: Teflon AF 1600 (DuPont), and cytop (PFC 1603V, Cytonix Co.). For both cases the concentration of the polymer to the solvent was $3\%\mathrm{wt/v}$, and the deposition was performed using a spin coater ($3500\ rpm$ at $60s$) followed by baking for $30\ min$ at $150°C$.

2.2.6 Selective removal of hydrophobic layer

In order to generate hydrophilic spots on the top plate or to expose the surface of the biosensor, a rectangular portion of the hydrophobic coating has to be removed. The following method was developed for this purpose: first, the cytop-coated slide was treated using oxygen-plasma for $2s$. This way the hydrophobic surface of the cytop becomes hydrophilic temporarily. A layer of the photoresist S1813 is coated and patterned (using photolithography) in a way that the entire cytop layer is protected by the photoresist layer except for the rectangular area, for which the photoresist is removed. The slide is then treated using oxygen plasma for $2\ min$ to remove the cytop layer. For the case of the biosensor, after the removal of the cytop layer the sensing surface will be exposed. For the case of the hydrophilic spots with different surface properties, the hydrophilic material (Au or SiO_2) is sputtered on the slide with the thickness of $10\ nm$ and then the slide is immersed in acetone to lift-off the deposited layer and the photoresist layer from the cytop portion of the slide. This way, the slide is covered with cytop except for the hydrophilic spots which is coated either with Au or SiO_2. Finally, the slide is post baked at $200°C$ for $1\ hr$ to recover the hydrophobicity of the cytop layer.

2.2.7 Functionalization of biosensing surface

For the biosensing part of the experiments, a top plate covered with layers of Cr and Au is used. The interdigitated electrode (IDE) capacitive biosensor along with the ground electrodes is patterned on the slide using standard photolithography, as explained in Section 2.2. The substrate is then coated with cytop. A rectangular part of the cytop is removed from biosensor using oxygen-plasma (explained in the previous section) to expose the IDE area to the target.

Monoclonal antibodies (IgG3) were purchased from AbD Serotec (USA). Purified antigen, *Cryptosporidium* from Waterborne (USA), was used as the target. Recombinant Protein G/thiol was purchased from protein MOD (Canada). All other reagents and solvents were of the analytical grade and purchased from Sigma Aldrich.

The immobilization of anti-*Cryptosporidium* antibodies on the gold surface of the interdigitated electrodes (IDE) was carried out in the following steps: first, the IDE surface was subjected to plasma cleaning (for $10\ min$). Then, it was immersed in a recombinant protein G/thiol solution for $24\ hr$ where a self-assembled monolayer (SAM) was formed. This process was followed by thoroughly rinsing the chip with DI water and drying using pure nitrogen. The formation of SAM is a natural reaction occurring by adsorption of protein G/thiol on to the gold surface of IDE through the thiol sulfide linkage. In essence, sulfur has a high affinity towards gold atom leading to formation of high self-assembly monolayer with a high stability in water, air and also organic solvents at room temperature [205, 206]. The free (uncoated) regions on the IDE surface were blocked by adding 0.5% bovine serum albumin (BSA) (wt/v) in the phosphate-buffered saline (PBS) for $3\ hr$ at $4℃$ and then washed with the PBS buffer. The protein G/thiol activated IDE was then covered by $5\mu L$ of anti-*Cryptosporidium* antibodies (with the concentration of $0.1 mg/mL$ in PBS (pH 7.4)) for $24\ hr$ at $4℃$. In the final step, the functionalized IDE surface was washed twice with the PBS buffer and once with the DI water. The immobilization of the anti-*Cryptosporidium* antibodies was confirmed by two methods: the capacitance, and the contact angle measurement before and after immobilization (see Chapter 6).

2.3 Error of measurement

Each of the measurement processes used in this thesis is associated with a measurement error, which is related to the resolution of the device and data. The following table presents the measurement errors for the results in the following chapters.

Table 2-1 The measurement errors for the parameters used in this thesis.

Parameter	**Error of measurement**
Area of droplet	$\pm 1\%$
Gap height (tape)	$\pm 5\ \mu m$
Gap height (motorized jack)	$\pm 1.5\ \mu m$
Threshold splitting voltage	$\pm 0.05\ V$
Color intensity	$\pm 0.1\%$
Mixing time	$\pm 0.066\ s$
Local number of particles	$\pm 1\%$
Contact angle measurement	± 0.5º
Capacitance	$\pm 10\ fF$

Chapter 3 Development of a geometrical-based technique for accurate unequal droplet splitting[2]

3.1 Overview

Among the basic operations in DMF devices, splitting and dispensing are less straightforward and require specific geometrical and electrical criteria to be performed successfully [14]. In essence, for splitting a mother droplet into two daughter droplets (or dispensing a droplet from a reservoir), necking and breakup of the droplet is crucial. Berthier et al. [90] studied dispensing a droplet from a reservoir droplet by taking into account the relation between the required applied potential and the system parameters (such as the initial apparent contact angle, the droplet and electrode sizes, and the gap between the two plates). In their analytical study, they showed that for a DMF device there is a limit for the gap size above which droplet splitting is impossible. Cho et al. [14] also studied droplet manipulation and splitting under different conditions. Their results demonstrated that splitting a droplet is facilitated by lowering the gap between the two plates, increasing the size of the droplet and/or electrodes, and the reduction of the apparent contact angle (which is related to the applied voltage). They also obtained a limit for the ratio of the gap over the droplet radius, above which splitting cannot be achieved. Banerjee et al. [91] showed that the accuracy of droplet splitting/dispensing is increased by ramping down the applied voltage instead of turning it off suddenly. Liu et al. [19] also illustrated that accurate droplet dispensing could consistently be achieved by using a continuous reservoir instead of a reservoir droplet. They also developed an image-processing-based technique for the accurate measurement of the droplet size which was related to the

---

[2] Parts of this chapter have been published in Journal of Micromechanics and Microengineering (E. Samiei and M. Hoorfar, *J. Micromech. Microeng.*, (2015), 25, 055008).

electrode size. Lin et al. [68] reported dispensing droplets of several pico-liters on EWOD-based DMF platforms using small size electrodes and gap heights.

Splitting plays an important role in diluting, concentrating or separating particles in a droplet which are important for promoting DMF platforms in biological applications. Using electrophoresis, Cho and Kim [207] separated two types of particles mixed in a mother droplet which was split into two daughter droplets containing different particles. Splitting has also been used in the cell concentration applications conducted based on dielectrophoresis [114, 115, 130] and particle focusing in a liquid droplet based on traveling wave dielectrophoresis [208]. Droplet splitting is also important in preparing different biological samples for applications such as proteomics [46], glucose assays [108], and clinical diagnostics from body fluids [108]. In all these examples (involving separation, dilution, and concentration), however, the ordinary method of equal splitting (with the ratio of 1:1) has been performed. Despite the ease of performing equal splitting, the final ratio of 1:1 is not efficient for applications in which a high concentrated droplet or a high accurate separation of particles/cells is desired. Also, to reach a high ratio of dilution, either a large quantity of diluting agent must be mixed with the sample (which hinders droplet actuation), or the dilution process must be repeated consecutively. In order to overcome these problems, unequal splitting with the volume ratio of $1: x$ $(x \neq 1)$ has been implemented by applying different voltages to the adjacent electrodes [18]. For this purpose, capacitance measurement along with a real-time feedback control system has been integrated into the DMF platform to determine the droplet volumes and control the volume of the split droplets, respectively. Unequal splitting has been performed successfully using this method with high precision; however, the need for sensing and feedback control makes the fabrication of the device complicated and expensive.

This chapter presents a new operator for unequal droplet splitting (based on the principle of 1: x splitting) and dispensing droplets with a wide range of sizes by geometrical modification of the conventional electrodes in DMF devices. As the main features of this operator, unequal splitting and variable volume dispensing can be performed on an area as small as a conventional electrode without the need for a closed loop control system. For this purpose, one of the actuating electrodes is divided into several smaller sub-electrodes, which can be actuated individually, and splitting is performed by different combinations of the sub-electrodes actuated simultaneously. The actuation of the electrodes is similar to that of droplet dispensing. Droplets with small sizes (comparable to the area of the electrode) can be split unequally. This operator can also be used for the extraction of droplets from a reservoir, which is the act of dispensing. However, the advantage of using the proposed operator is that droplets with a wide range of sizes can be dispensed from a reservoir, while the conventional method of dispensing provides only one size of the dispensed droplet (based on the electrode size and the gap height between the two electrodes).

The robustness of the proposed method is examined by showing a relation between the surface area of the simultaneously actuated sub-electrodes and the volume of the split droplet. The effects of the sub-electrode geometry, the applied voltage and the gap height between the two plates on the performance of the device are studied thoroughly. Different configurations for sub-electrodes are tested to analyze the dependency of the proposed technique on the geometrical configuration, and to find the geometry providing higher reliability and a wider range of the sizes for the split droplet accordingly. For this purpose, the applied voltages ranging from the threshold splitting voltage to significantly higher values is studied to analyze the effect of the voltage on the size and reproducibility of the split droplets. In addition, the relation between the threshold splitting voltage and the gap height is studied to obtain the limits of splitting. Dependency of the size of the split droplet to the initial size of the mother droplet, which is crucial for consistent droplet generation, is also taken into account.

3.2 Experimental procedure

The schematic of the experimental setup used in this study is shown in Figure 3-1. A motorized jack is used to adjust the gap height between the two plates. In this study, the electrode geometry is used as a mean to perform unequal splitting and generate droplets with different volumes. Figure 3-2 shows three configurations studied as the sub-electrodes. In the first configuration (Figure 3-2a) the electrode is striped along its length (referred to as SL). In the second configuration (b), the electrode is striped along its width (SW). Finally, in the last configuration (c), the electrode is striped in both ways to form square sub-electrodes (SQ). The study is conducted with the electrode size of $2.5\,mm \times 2.5\,mm$. The distance between the two adjacent electrodes is set as $20\,\mu m$. Two sets of chips are designed, as shown in the first and second rows of Figure 3-2. In the first set (first row in Figure 3-2), all three configurations include 4 sub-electrodes resulting in an equal area of the sub-electrodes for all three configurations. In the second set (second row in Figure 3-2), however, different numbers of sub-electrodes were included in each configuration (5 sub-electrodes for the SL and SW configurations, and 9 sub-electrodes (3×3) for the SQ configuration) to study a wide range of droplet sizes generated using this method. To be able to address the middle electrodes in the 3×3 arrays of the SQ configuration, the sub-electrodes in the middle row have been connected to their adjacent sub-electrodes at the bottom row (see configuration (c) in the second row in Figure 3-2).

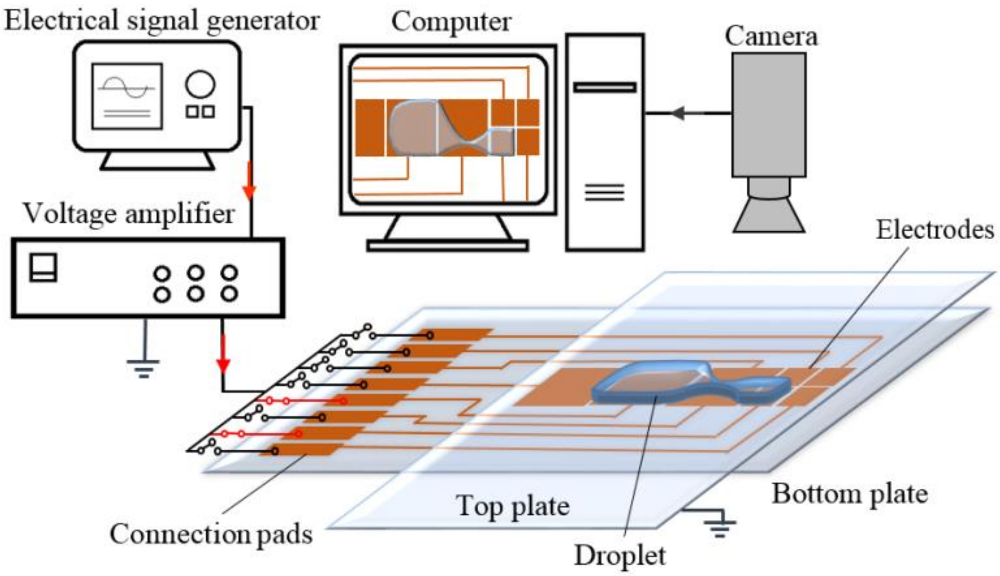

Figure 3-1 Schematic of the experimental set up.

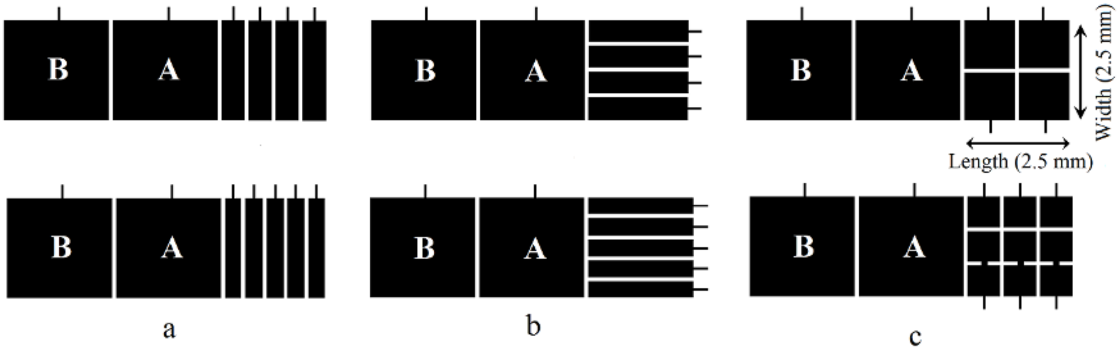

Figure 3-2 (a) SL, (b) SW and (c) SQ configurations. The first row includes all the configurations with 4 sub-electrodes and the second row includes SL and SW configurations with 5 sub-electrodes and SQ configuration with 9 sub-electrodes.

The method adopted here for splitting the droplets unequally is the sequential actuation of the electrodes, similar to that of droplet dispensing from a reservoir. In essence, the droplet is moved to the electrode adjacent to the sub-electrodes, e.g., the electrode A shown in Figure 3-2. Based on the desired volume, one or several sub-electrodes are then activated, upon which a part of the droplet is pulled over the activated sub-electrodes, and then the electrode A is turned off. Finally, to split the droplet the farthest electrode (the electrode B in Figure 3-2) is activated while the sub-electrodes are still active. The activation time varies based on the voltage applied to the system, i.e. the activation continues until the droplet is split. The surface area of the droplet (S_d) is chosen as the criterion representing the droplet size. The approximate volume can simply be calculated by multiplying S_d and h. This method produces a very small error for the gap heights considered in this study. In fact, Cho et al. [14] introduced a limit for the gap height as $h/\acute{r}_2 < 0.22$ in which h is the gap height and $\acute{r}_2$ is the radius of the droplet interface in the neck region. They have shown that with a good approximation $\acute{r}_2$ can be replaced by $w/2$, where w presents the width of the electrode. In this study, we introduce a relationship for the calculation of $\acute{r}_2$ (in Section 3.3). Based on the maximum gap height used in this study (see Section 3.4), the ratio of $h/\acute{r}_2$ is 0.14 which is much smaller than the limit introduced by Cho et al. [14]. The surface area of the droplet was measured using the ImageJ software package. The initial gap height between the two plates was first set by a set of spacers of a known size, and then controlled by the side-view images captured by the camera. The gap was then changed using a motorized motion stage. To double check the accuracy, the gap size was again measured from the side view of the platform. The mother droplet was dispensed on the platform by a calibrated manual pipette (with standard deviation (SD) of ± 1.4% for a 5-µL range). However, the droplet size was measured from the top view using the method described above. A frequency of $f = 1kHz$ was chosen for the applied voltage for all experiments. The threshold voltage for droplet splitting is defined as a voltage upon which the surface area of the split droplet is equal or larger than the size of the actuated sub-electrodes. All experiments were repeated at least five times and the average and SD values were calculated.

3.3 Analytical approach

In this study, a qualitative analytical model has been developed based on the Laplace equation (see Equation 3-1). A few assumptions were implemented: the first assumption is that the centerline of the sub-electrode and the actuated electrode are aligned (see the schematic in Figure 3-3), ensuring symmetrical neck formation. The second assumption is that the droplet pins at the corners of the sub-electrode and farther electrode. The study by Berthier et al. [90] shows this assumption does not generate significant errors, while it simplifies the equations. The third assumption considers that the interface at the neck is in a circular form.

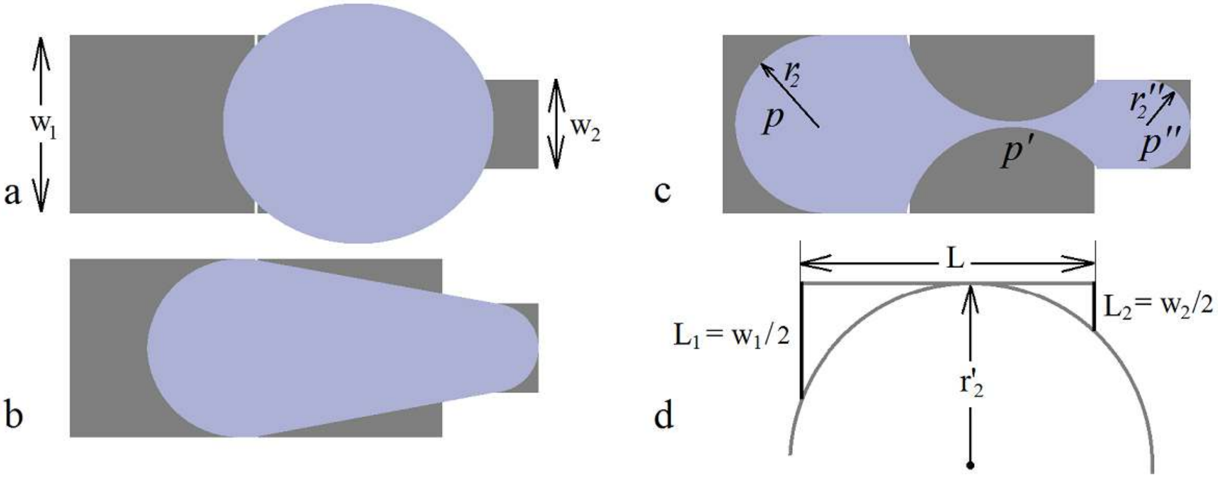

Figure 3-3 (a)The initial location of the droplet between the actuated and the sub-electrodes; (b) activation of the sub-electrode and the farthest electrode (before neck formation); (c) neck formation at the verge of splitting; and (d) estimated curve for the interface at the neck.

Three pressure terms are considered in three regions inside the droplet: the pressure at the left side of the droplet or the mother droplet (p), the pressure at the middle of the droplet or the place where the neck forms (p'), and the pressure at the right side of the droplet or the daughter droplet (p"). In each region, the pressure difference with the surrounding air is calculated from the Laplace equation:

$$\Delta p = \Gamma\kappa = \Gamma\left(\frac{1}{r_1}+\frac{1}{r_2}\right) \tag{3-1}$$

in which Γ is the interfacial tension between the liquid and the gas phases; κ is the curvature of the liquid-gas interface; and r_1 and r_2 are the principle radii. r_1 is the radius at the interface observed from the side view and calculated as [89, 90]:

$$r_1 = \frac{h}{-cos\theta_1 - cos\theta_2} \tag{3-2}$$

where h presents the gap height; θ_1 is the apparent contact angle with the top plate and is assumed to be equal to θ_0 which is the contact angle of water on Teflon. θ_2 is the apparent contact angle with the bottom plate which is also equal to θ_0 when no voltage is applied to the local electrode. When the voltage is applied, θ_2 is equal to $\theta(U_{rms})$.

After activating the two side electrodes, the radius of curvature r_1 in three regions (the mother droplet, the middle where the neck forms, and the sub-electrode) can be calculated from the following relations:

$$r_1 = \frac{h}{-cos\theta_0 - cos\theta(U_{rms})} \tag{3-3}$$

$$r_1' = \frac{h}{-2cos\theta_0} \tag{3-4}$$

$$r_1'' = \frac{h}{-cos\theta_0 - cos\theta(U_{rms})} \tag{3-5}$$

To determine r_2 (i.e., the radius of curvature from the top view), it is assumed that the interface of the mother droplet is semicircular with the radius equal to the half of the size of the local electrodes (i.e. $r_2 = w_1/2$). This radius at the interface on the sub-electrode, however, depends on the amplitude of the applied voltage, and hence can range from a semicircle ($r_2^{''} = w_2/2$) to a flat shape ($r_2'' = \infty$) for low and high voltages, respectively (this will be shown experimentally later on). The middle part of the droplet in which the neck forms is located on the middle electrode which is grounded at the time of splitting. Thus, it is assumed that the interface at the neck has a circular form (with the dimensions shown in Figure 3-3d). Considering this and the assumption that the droplet pins at the corners of the sub-electrode and farther electrode, the following analytical relation can be obtained for the radius r_2' (at the neck):

$$r_2' = -L_1/Z^2 \tag{3-6}$$

where Z is the solution to the following fourth order equation:

$$aZ^4 + bZ^2 + c = 0 \tag{3-7}$$

in which:

$$\begin{aligned} a &= L^4 + 2L^2L_1^2 + 2L^2L_2^2 + L_1^4 - 2L_1^2L_2^2 + L_2^4 \\ b &= -4L^2L_2^2 - 4\,L^2L_1L_2 - 4L_2^4 + 4L_1L_2^3 + 4L_1^2L_2^2 - 4L_1^3L_2 \\ c &= 4L_1^2L_2^2 - 8L_1L_2^3 + 4L_2^4 \end{aligned} \tag{3-8}$$

Substituting the calculated radii into Equation (3-1) provides the local pressure in each region shown in Figure 3-3c (p representing the local pressure in the mother droplet region; p' presents the local pressure in the neck region, and p'' represents the local pressure in the sub-electrode region). These pressures will be used for analyzing the splitting process in the next section.

3.4 Results and discussion

The main purpose of this study is to evaluate whether modifying the electrode geometry could be used as a controlled method for precise unequal droplet splitting with the ratio of $1{:}\,x$ ($x \neq$

1) and dispensing droplets of variable sizes. As the limiting parameters, the effects of the magnitude of the applied voltage and the gap height between the two plates are taken into account. Two sets of experiments have been designed. The first set of the experiments aims at analyzing the dependency of the proposed technique on the sub-electrode geometry and also finding a reliable activation scheme for precise splitting. The second set of experiments was performed to show the applicability of the proposed method.

3.4.1 Parametric study

In the first set of experiments, a regular electrode is divided into 4 sub-electrodes with three configurations of SL, SW and SQ (see the first row of Figure 3-2). Consequently, all the three configurations have sub-electrodes with equal surface area. To extract various volumes of the droplet using these designs, splitting is performed with different numbers of actuated sub-electrodes (i.e. $n = 1, 2$ and 4). Two gap sizes of $h = 140\mu m$ and $h = 180\mu m$ are considered to take into account the effect of the gap height. Splitting with one sub-electrode and $h = 140\mu m$ was performed and threshold splitting voltages of $U_{rms} = 72\ V$, $91V$, and $69V$ were measured for SL, SW and SQ configurations, respectively. These voltages were considered to determine the range of the voltages that can be used for this study. Since the lowest threshold voltage obtained is 69 V, the range chosen here starts from 70 V. Also, for obtaining the results for voltages significantly higher than the threshold values, a maximum value of 110 V was considered and the range was divided into 70, 80, 90, 100 and 110 V. This way splitting is performed with voltages close to and significantly larger than the threshold voltage to have a conclusive set of results about the effect of the voltage. Figure 3-4 showing the result of this analysis presents the normalized surface area of the split droplet ($S_d^* = S_d/$ (area of one sub-electrode)) as a function of the applied voltage. Each point in this figure presents the average of 5 replications. The error bars present the standard deviation (SD) from the average. It should be noted that for a certain number of actuated sub-electrodes (such as $n = 2$) different combinations of the sub-electrodes can be used (such as a vertical or a horizontal pair). However, at this stage, the present study focuses on proving the feasibility of the proposed method rather than the choice of the actuated sub-electrodes.

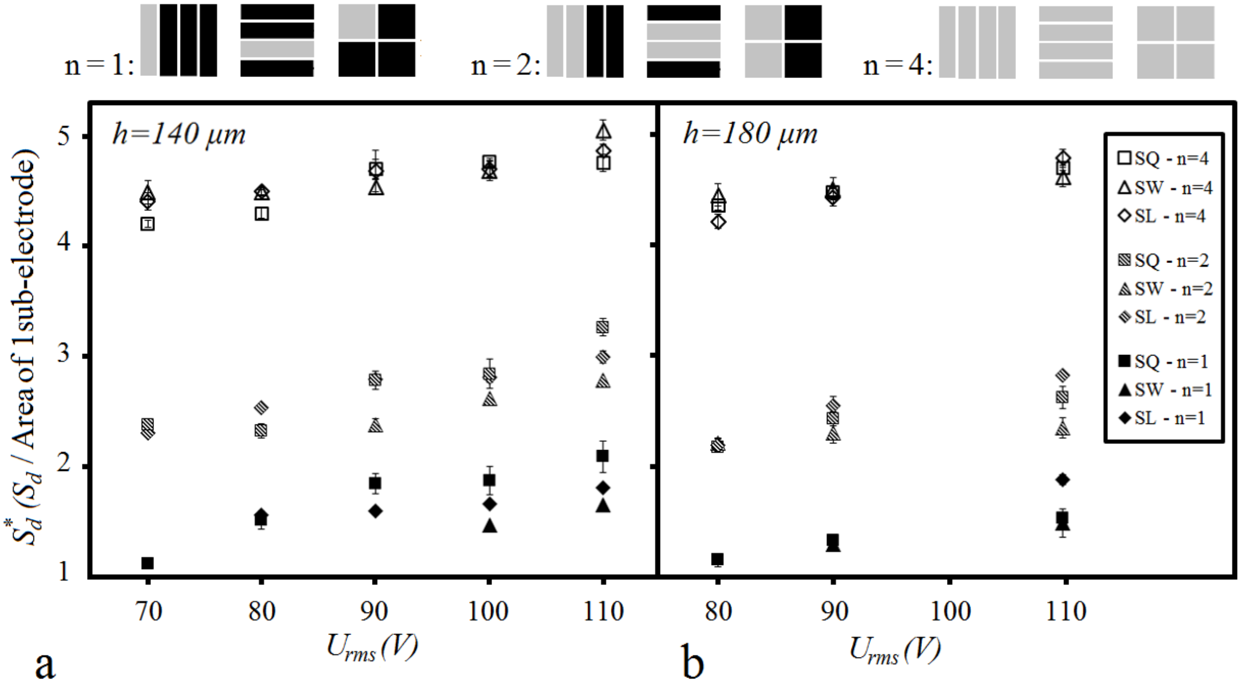

Figure 3-4 Normalized surface area of the split droplet as a function of the applied voltage. The results were obtained for different numbers of activated sub-electrodes (with three configurations of SL, SW and SQ) for the gap sizes of (a) $h = 140\mu m$ and (b) $h = 180\mu m$. All the configurations have 4 sub-electrodes. On the top of the figure, the actuated sub-electrodes are shown in gray for each number of actuated sub-electrodes.

The following sections discuss the conclusions from Figure 3-4, which illustrates the effects of the configuration, the gap height and the applied voltage on the size and reproducibility of the split droplet.

3.4.1.1 Effect of configuration

Figure 3-4 illustrates that when the applied voltage is higher than the threshold value, the electrode configuration affects the size of the split droplet. For $n = 1$ and 2, the size of the split droplet for the SW configuration is smaller than those obtained from the SQ and SL configurations. This could be related to the size of the neck forming at the verge of splitting: in essence, at the moment of splitting, the droplet covers not only the sub-electrode, but also a portion of the middle electrode where the neck is formed. This portion of the liquid (i.e., the neck) causes the area of the split droplet to be larger than the area of the actuated sub-electrodes (this can be observed in the results presented in Figure 3-4 for all configurations and combinations of sub-electrodes). However, the neck size is different for different configurations of sub-electrodes. Figure 3-5 shows the split droplets (using the SQ, SL and SW configurations) right after the breakup of the neck while the sub-electrodes are still activated. The number of the activated sub-electrodes for all configurations is $n = 2$ and the applied voltage and the gap height are $U_{rms} = 100V$ and $h = 140\mu m$, respectively. It is observed that the extra liquid on the middle electrode (circled by white lines) is larger for the SQ and SL configurations due to a wider actuated area (resulting in the formation of a neck with a wider base). On the other hand, the droplet generated by the SW configuration has a smaller size in comparison with the other two configurations, due to the formation of a thinner neck resulting in a smaller amount of extra liquid on the middle electrode. While this discrepancy in the droplet size is observed for high voltages, it has been found that when the applied voltage is close to the threshold value, the area of the split droplet for all configurations approaches the same value (see Figure 3-4).

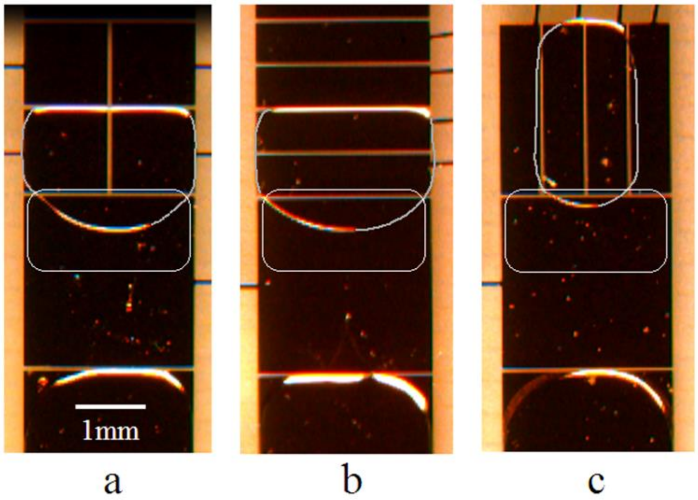

Figure 3-5 Split droplets right after breakup of the neck for (a) SQ, (b) SL and (c) SW configurations while the electrodes are still actuated. For all cases $h = 140\mu m$ and $U_{rms} = 100V$.

It is noted that for the number of the sub-electrodes $n = 2$ the normalized surface area of the split droplet (S_d^*) for the SQ configuration is similar to that obtained for the SL configuration. This is due to the fact that when the first two sub-electrodes of SQ are activated the actuated area becomes the same as the SL configuration (which has the complete width but half of the length of the regular electrode). The same case is true when all 4 sub-electrodes are activated for all the configurations (i.e., for $n = 4$ all three configurations have the same results).

3.4.1.2 Effect of the gap height

Figure 3-4a and b show the results obtained for two gap heights of $h = 140\mu m$ and $h = 180\mu m$, respectively. It was observed that as the gap height is increased the applied voltage must also be increased (i.e. the threshold splitting voltage increases once the gap height increases). Thus, the results presented for $h = 180\mu m$ are for the applied voltage of $U_{rms} = 80V$, $90V$ and $110V$. Nevertheless, the general trend of the area of the split droplet (S_d^*) as a function of the applied voltage is the same for both gap heights (i.e., as the voltage increases the area of the split droplet increases). However, for the larger gap height, the droplet sizes (S_d^*) are slightly smaller than those obtained for the smaller gap height. When the applied voltage is decreased to the values close to the threshold value the sizes of the split droplets for $h = 180\mu m$ approach to those obtained for $h = 140\mu m$. To analyze further this effect, droplet splitting was performed using the SQ configuration (with $n = 1$) with the gap height of $h = 100\mu m$, for which $S_d^* = 1.138$ was measured for the size of the split droplet. Comparing this value to those obtained for $h = 140\mu m$ and $h = 180\mu m$ ($S_d^* = 1.172$ and $S_d^* = 1.122$, respectively) shows that the difference between these areas is less than 5%. This means that the effect of the gap height on the droplet surface area can be insignificant when the electrodes are activated using a voltage close to the threshold splitting voltage. However, this error might not be within an acceptable range for some applications.

3.4.1.3 Effect of the applied voltage

In general, as the number of the activated sub-electrodes (n) increases from 1 to 2 and to 4, the surface area of the split droplet becomes larger. Of course, the ideal case for generating controlled volumes of the droplets is when the normalized surface area of the droplet is equal to the number of the activated sub-electrodes (i.e., $S_d^* = 1,2,4$ for $n = 1, 2, 4$, respectively). This means that the contact area of the split droplet is equal to the size of the actuated area. However, as shown in Figure 3-4, the droplet size is bigger than the area of the actuated electrode. As described in the “Experimental procedure” section (Section 3.2), the activation scheme here is similar to that of droplet dispensing, i.e. the droplet is pulled on the sub-electrode and then split by pulling it from the farthest electrode (B). Using this activation scheme, it is shown (see Figure 3-4) that for all the configurations (SL, SW and SQ) and number of the activated sub-electrodes the droplet size increases as the applied voltage increases beyond the threshold splitting voltage (an ascending trend). For low voltages (slightly higher than the threshold splitting voltage) the split droplet area is much closer to the activated area (S_d^* is close to the n value) with a small SD; whereas for high voltages the area of the split droplet deviates from the activated area with a higher SD. For high voltages, the S_d^* value for SL, SW and SQ configurations also differs from each other: as described in the previous section, when the voltage decreases S_d^* for different configurations becomes quite similar. The error bars also show that for low applied voltage the SD value from the average value is smaller (less than 2% for SW and SL, and less than 1% for SQ). These results suggest that using this scheme of electrode activation the size of the split droplet is more controllable (and reproducible) and more independent from the configuration. Splitting was also conducted with the SQ configuration for different initial volumes (ranging between $V_d = 3 - 4\ \mu L$) and a sequence of extraction (5 times). The variation in the size of the daughter droplets was less than 1% for $h = 140\mu m$ and less than 2% for $h = 180\mu m$. This high accuracy was obtained for the case in which the mother droplet is large enough to cover the sub-electrode and the width of the farthest electrode (electrode B); otherwise the accuracy slightly decreases.

To study further the effect of the applied voltage on the size of the split droplet, splitting was conducted with the SQ configuration with the applied voltages of $U_{rms} = 70\ V$, $80\ V$ and $110V$ for $h = 140\mu m$ (Figure 3-6 a-c) and $U_{rms} = 80\ V$ and $110V$ for $h = 180\mu m$ (Figure 3-6 d and e). In Figure 3-6 a-e, the left images show the neck at the verge of splitting, and the right images show the moment right after splitting. However, due to the limitation in the speed of the camera (15 frames/second) it was only possible to capture the neck for the lowest possible voltages (see Figure 3-6a and d). As it is observed from Figure 3-6 and discussed previously, increasing the actuation voltage increases the size of the split droplet.

This could be due to the fact that for higher voltages splitting occurs faster due to the larger EWOD force, and hence liquid inertia affects the split droplet size. Therefore, for the cases with the smallest voltage (i.e., (a) and (d) which show splitting for $h = 140\mu m$ and $h = 180\mu m$, respectively) the liquid has enough time to travel away from the neck and make a thinner neck; whereas for higher voltages (for which breakups occur much faster) the liquid does not have enough time to be pulled away from the neck by the activated electrodes, resulting in an increase in the size of the split droplet. As the applied voltage increases, this effect becomes more significant.

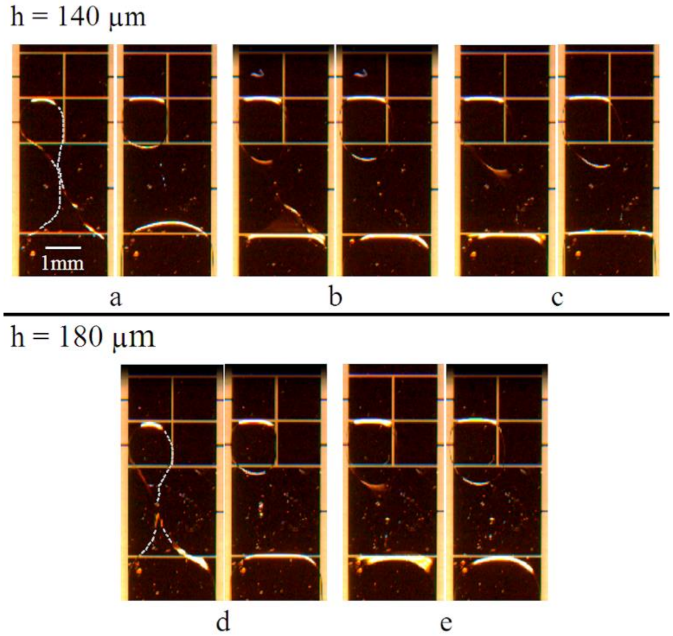

Figure 3-6 Droplet splitting with the SQ configuration for $h = 140\mu m$ (a) $U_{rms} = 70V$, (b) $U_{rms} = 80V$, (c) $U_{rms} = 110V$, and $h = 180\mu m$ (d) $U_{rms} = 80V$ and (e) $U_{rms} = 110V$. For all cases, the left image shows the neck at the verge of splitting, and the right images show the moment right after splitting.

Another point observed from the results in Figure 3-6 is the curvature of the droplet interface before splitting in the cases of the low voltages (a and d) compared to the cases of high voltages (b, c and e). In essence, for low voltage cases (a and d) the liquid covered the sub-electrode has a round interface before splitting. This is due to the fact that for low voltages the EWOD force on the sub-electrode cannot overcome the surface tension force at the liquid-gas interface, and hence cannot pull the droplet and make it align with the entire electrode. However, as the applied voltage increases the interface of the liquid on the sub-electrode becomes more flat at the end part.

The analytical model presented in this study is used to verify qualitatively the effects observed in Figure 3-6. To find a relation between the curvature at the interface and the applied voltage, two extreme cases of low and high voltages will be considered. For the extreme case with a low applied voltage, the shape of the droplet interface at the end of the sub-electrode is assumed to be circular (similar to Figure 3-6a). Therefore, the radius of curvature at the interface will be $r_2'' = w_2/2$ (See Figure 3-3c). For the other extreme case with the high voltage, on the other hand, the shape of the interface is flat, resulting in the radius of curvature of $r_2'' = \infty$. Also, the radius at the side of the mother droplet is considered as $r_2 = w_1/2$ (Figure 3-3c). A series of experiments were performed to find the relation between the applied voltage and the apparent contact angle. The results are presented in Figure 3-7a. Based on the other radii from Equations (3-3) to (3-6) and the contact angle-vs-applied-voltage curve, the pressure at the three regions (the mother droplet side (p), the neck (p'), and the sub-electrode side (p'')) can be calculated. Based on this analysis, it is considered that at the splitting moment the driving force for liquid motion from the neck to the other two sides is the internal pressures. Since the pressure in the neck is higher than the other two sides, the liquid moves from the neck to the sides, resulting in the breakup of the neck. In this study, $\Delta p_1 = p' - p$ presents the driving force for liquid motion from the neck to the mother droplet and $\Delta p_2 = p' - p''$ is the driving force from the neck to the sub-electrode. Figure 3-7b shows Δp_1 and Δp_2 as a function of the applied voltage for two extreme cases of the interface shapes studied here (i.e., circular ($r_2^{''} = w_2/2$) and flat ($r_2^{''} = \infty$)). As shown in Figure 3-7b, if the interface of the split droplet (at the end of the sub-electrode) has a circular shape (low actuation voltage), $\Delta p_1 > \Delta p_2$, meaning that the driving force, and hence, the liquid motion towards the mother droplet is stronger than that towards the sub-electrode. Therefore, the split droplet will cover an area not much larger than the area of the sub-electrode. However, for the extreme case of the droplet with a flat interface at the sub-electrode (high activation voltage), $\Delta p_1 < \Delta p_2$ which means the driving force and the resultant liquid flow is more towards the sub-electrode, making the size of the split droplet larger.

The two conditions which were considered above were the two extreme cases. The real cases fall within these two cases, i.e. for low applied voltages the interface at the sub-electrode is circular, but as the voltage is increased the interface will turn gradually from circular to flat. Hence, the size of the split droplet will be an ascending function of the applied voltage (as it is observed in Figure 3-4).

3.4.2 Applicability of the proposed method

The first set of the experiments suggested the superiority of the SQ configuration over the SL and SW (in terms of precision and the range of the applied voltage) for unequal splitting. Also, an actuation scheme was used for reproducible and precise droplet splitting based on the sequential activation of the electrodes using a voltage slightly larger than the threshold splitting voltage. In the second set of experiments the threshold splitting voltage (U_{rms}) versus the gap height will be studied, along with assessing the feasibility of the proposed technique for a wide range of splitting ratios and droplet sizes.

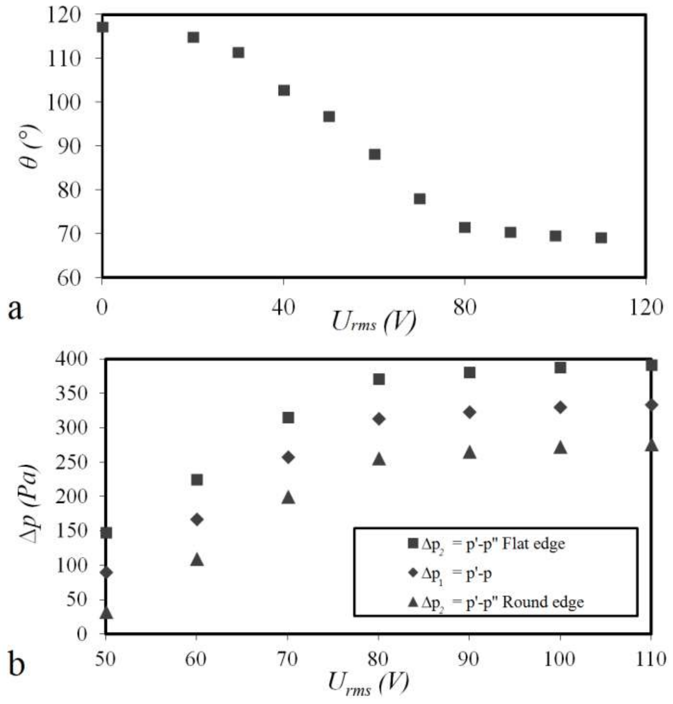

Figure 3-7 (a) Apparent contact angle versus the applied voltage measured experimentally for $h = 140\mu m$. (b) Δp_1 and Δp_2 versus the applied voltage for two extreme cases of interface shapes, i.e. circular (low voltage) and flat (high voltage) at the end side of the droplet on the sub-electrode. The results were obtained for the gap height of $h = 140\mu m$. For other gap heights the trend will be the same but the absolute values for Δp_1 and Δp_2 will be different from those presented in this figure.

For this set of experiments the modified electrode is divided into 5 sub-electrodes for the SL and SW configurations and 9 sub-electrodes for the SQ configuration (the designed configurations are shown in the second row of Figure 3-2). It has to be mentioned that more than five sub-electrodes make them too thin to perform robust splitting for the SL and SW cases, and more than nine makes fabrication of the SQ sub-electrodes difficult. Here, the SL and SW configurations are used to study the effect of the reduced length and width of the electrodes on the limits of splitting, respectively; while the SQ configuration, which contains more sub-electrodes and covers a wider range of droplet sizes, facilitates droplet generation with a wider range of splitting volumes.

Figure 3-8 shows the threshold splitting voltage with respect to the gap height with one actuated sub-electrode for the three configurations. Within the range of the gap heights shown in this figure the relation between the threshold splitting voltage and the gap height is linear for the SQ and SL configurations. This linear behavior can basically be used as a reference to choose an appropriate voltage based on the gap height. However, for high applied voltages the threshold voltage for the SW configuration increases exponentially with a larger SD (reflecting irreproducibility of the results). Therefore, a linear curve does not fit well to the data obtained for SW, making this configuration less reliable than the other two configurations. This figure along with Figure 3-4 (see the points for the low voltages and $n = 1$) reflects the fact that the reduced width of the electrode in the case of SW has a negative impact on splitting performance with a limited range of applicability. For the other two configurations, however, the threshold splitting voltage shows a linear trend for the entire range of the gap heights shown here. Beyond this range of the gap heights, this linear trend may also not exist for the SL and SQ configurations. These results are qualitatively in good agreement with the analytical results presented by [90]. This linear relation shown in Figure 3-8 facilitates the selection of the appropriate voltages for extracting droplets with a controlled size for any given gap sizes.

The linear curve (see Figure 3-8) along with the low deviation (less than 1%) obtained for the size of the split droplets in the SQ configuration (see Figure 3-4) suggests that SQ is a reliable design for the proposed unequal splitting operator. Thus, the relation between the number of the actuated sub-electrodes and the size of the split droplets using SQ is studied. The gap height is chosen as $h = 140\mu m$ and the applied voltage is set as the threshold value obtained from

Figure 3-8. For each combination of the sub-electrodes, the experiment has been replicated five times and the average values of the normalized droplet size (S_d^*) and SD from the average values were recorded and plotted in Figure 3-9.

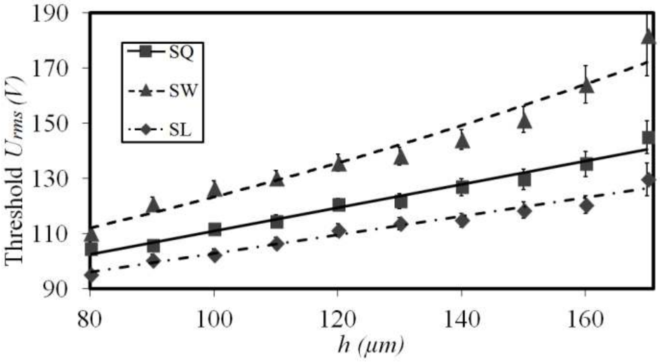

Figure 3-8 Threshold splitting voltage versus the gap height for three configurations of SL, SW, SQ, where the SL and SW configurations have 5, and SQ configuration has 9 sub-electrodes. For all cases, one sub-electrode is actuated to obtain the results.

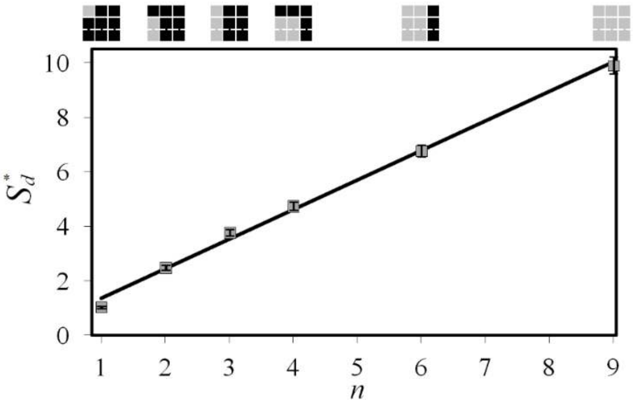

Figure 3-9 Surface area of the split droplet versus the number of the actuated sub-electrodes for the SQ configuration with 9 sub-electrodes. On the top of the figure, the actuated sub-electrodes are shown in gray. Here, $h = 140\mu m$ and the applied voltage equals the threshold splitting voltage.

The results show that there is a linear relation between the size of the split droplet and the number of the actuated sub-electrodes. This linear function allows for the estimation of the volumes of the generated droplets based on the size and number of the actuated sub-electrodes. This linear function is also useful to identify the number of the sub-electrodes to be actuated for generating a desired droplet volume. With a SD value of less than 1% for all different combinations of the actuated sub-electrodes, the proposed method offers great reproducibility for the size of the generated droplets. The droplets split using this configuration are shown in Figure 3-10. A very important feature of the present method is that unequal droplet splitting is performed with a very high precision and reproducibility without the need for feedback controlling the droplet size. This eliminates the need for integration of external modules into the DMF device, facilitating its portability and simplifying the fabrication of the chip.

Using a design with $0.5\ mm$ SQ sub-electrodes and the gap height of $h = 25\mu m$, droplets as small as $7nL$ were generated from a mother droplet with the size of $150nL$. However, this is not necessarily the smallest possible size which could be achieved by this method, as sub-electrodes of smaller sizes could be designed. This shows the high capability of the method for unequal splitting of droplets with a high volume ratio $(1{:}\,x)$. It has to be emphasized that the configurations adopted in this work were simple designs used as a proof of concept. These designs can be optimized geometrically to increase the efficiency of splitting and increase the size range of the split droplet.

3.5 Summary

The results obtained for studying the effect of the voltage on the splitting process showed that the applied voltage must be set close to the minimum voltage required for splitting (referred to as the threshold splitting voltage). This will result in split droplets with a precise volume which is fairly independent of the gap height and the sub-electrode geometries studied here. Also, by applying a voltage close to the threshold splitting voltage, the surface area of the split droplet will be close to the area of the actuated sub-electrodes. The results also showed that the threshold splitting voltage has a linear relationship with the gap height which enables the selection of a proper voltage based on the given gap height.

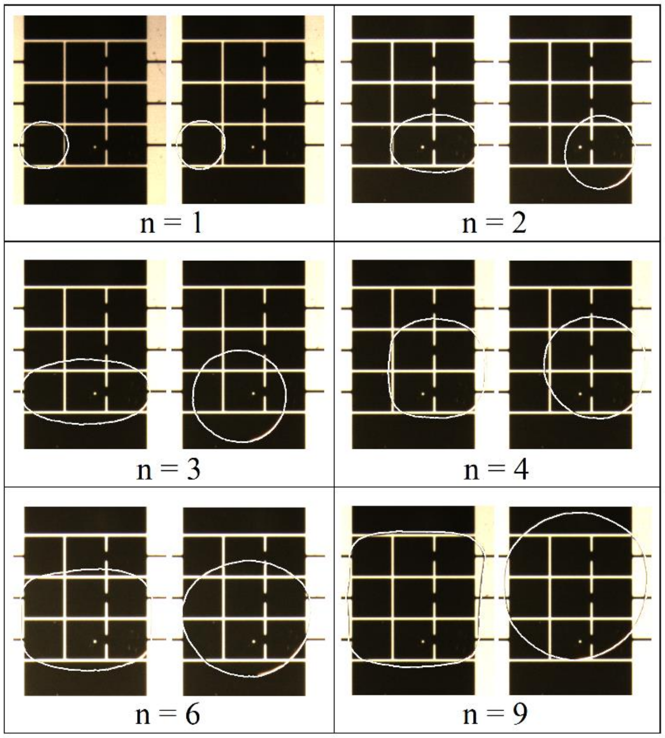
n = 1
n = 2
n = 3
n = 4
n = 6
n = 9

Figure 3-10 Droplets split with different combinations of the actuated sub-electrodes for the SQ configuration with 9 sub-electrodes. For each case, the images on the left show the situation in which the sub-electrodes are still on, and grounded in the images on the right hand side.

Based on the study conducted on the effect of the sub-electrode geometry on the splitting process, it was found that the SQ configuration is more effective than the other two configurations (SL and SW). By using the SQ configuration the droplet sizes are more reproducible, and a larger number of sub-electrodes can be fabricated from a conventional electrode, resulting in a wider range of droplet sizes.

Using the best geometry of the sub-electrodes (the SQ configuration) and the threshold splitting voltage, the results showed a linear relationship between the surface area of the split droplet and the number of the actuated sub-electrodes. This linear function allows for the estimation of the volumes of the generated droplets based on the size and number of the actuated sub-electrodes.

Chapter 4 Development of an electrohydrodynamic technique for rapid mixing in stationary droplets on digital microfluidic platforms[3]

4.1 Overview

Mixing is a crucial step in many biochemical applications requiring a very uniform mixing of two or more samples for achieving a high reaction rate [36]. Mixing on DMF was primarily performed by moving the droplet back and forth on an array of electrodes which could take several seconds [14, 36]. Later on, the mixing efficiency and time were further improved by moving the droplet over a 2×4 array of electrodes, where mixing with a uniformity of 95% could be performed within 1 second [209]. Despite such improvements, mixing using this technique requires a 2D array of electrodes which occupies a considerable portion of the chip. Also, for biological samples containing proteins and other analytes which have the tendency to adsorb on to the chip surface, frequent transport of the sample over the chip increases the chance of biofouling and the consequent cross-contamination and chip breakdown [113]. Therefore, a mixing method that can provide rapid mixing without the need for multiple electrodes or integration of additional modules or patterns in to the chip will significantly improve the range of applicability of the DMF devices for LOC applications.

This chapter presents an electrohydrodynamic technique for rapid mixing of droplets in open and closed digital microfluidic (DMF) platforms. The mixing method presented in this chapter is performed for the first time on DMF devices using an electrothermal effect, similar to the effect studied for sessile droplets in [210], by applying a high frequency AC voltage to the coplanar or parallel electrodes, inducing circulation zones inside the droplet which results in

---

[3] Parts of this chapter have been published in Lab on a Chip (E. Samiei et al., *Lab. Chip.*, (2016, Accepted)).

rapid mixing of the content. The advantages of the proposed method in comparison to conventional mixing methods that operate based on transporting the droplet back and forth and side to side include 1) a shorter mixing time, 2) the use of a fewer number of electrodes, reducing the size of the chip, and 3) the stationary nature of the technique which reduces the chance of cross-contamination and surface biofouling. Mixing using the proposed method is performed to create a uniform mixture after merging a water droplet with another droplet containing either particles or dye. The effects of the amplitude and frequency of the applied voltage, as well as the gap height and the droplet size are studied. The applicability of the developed mixing technique is examined for the samples containing salts and DNA.

4.2 Theory

Mixing within sessile droplets by generating flow circulation has been shown in a few studies. For a configuration shown in Figure 4-1a it was found that applying a low frequency AC voltage between the planar electrode and the wire, which is inserted into the liquid from the top, causes electrowetting-actuated oscillation of the liquid-air interface, and consequently, mixing the content inside the droplet [86, 211]. In another study, such an AC actuation of a sessile droplet was performed for a wider range of frequencies [212]. It was shown that for low frequencies (the values of which depend on the conductivity of the liquid) the liquid-air interface oscillates, resulting in the induced circulation zones within the droplet. Further increases in the frequency reduced the oscillation, and for a range of moderate frequencies, the droplet interface and content were stationary. However, for higher values of frequency, a circulation was induced within the droplet without any oscillation at the interface [212]. This phenomenon was further studied by numerical simulation of the fluid flow, the electric field, and the thermal effects inside the droplet [210, 213]. The simulation results showed that by applying the high frequency voltage the liquid zones with the highest intensity of the electric field (around the vertical wire in Figure 4-1a) are heated up by several degrees of Celsius, resulting in a gradient of temperature through the liquid. The change in the temperature causes a local change in the permittivity and conductivity of the liquid, forming a gradient of such properties through the droplet. Consequently, an electrohydrodynamic effect occurs due to the interaction of the electric field and the liquid with varying electrical properties. This generates a circulating motion such as the streamlines shown in Figure 4-1a. The studies in [210, 213] also showed that this phenomenon depends on the electrical conductivity of the liquid such that for low conductivities, the electrodydrodynamic mixing starts at several kHz, and as the conductivity of the liquid increases a higher frequency is required to generate such an effect. The high frequency electrohydrodynamic flow circulation explained above was shown for sessile droplets to study the physics of the phenomenon. This phenomenon can be implemented as a novel technique for mixing in lab-on-a-chip (LOC) applications.

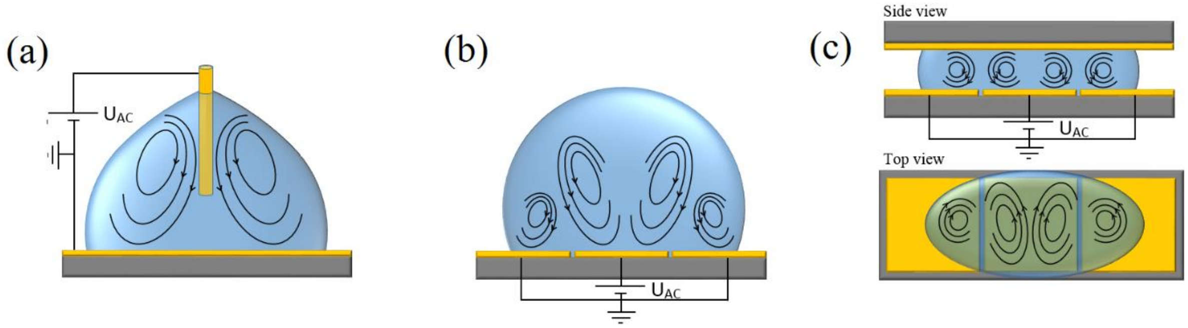

Figure 4-1 Schematic of the fluid flow in electrohydrodynamic mixing of a (a) sessile droplet, (b) droplet in the open DMF system, and (c) droplet in the closed DMF system.

In this chapter, such phenomenon is adopted to perform rapid mixing in DMF platforms. This could be achieved by designing certain patterns of electrodes to imitate the planar electrode-droplet-wire configuration explained above. However, modifying the method by changing the applied voltage and frequency rather than the geometrical modification of the conventional DMF chips makes the technique more versatile, as with no geometrical changes the mixing can be performed on any desired spot on the chip. To achieve this, the adjacent electrodes (with a distance of $\sim 30\mu m$) must be actuated with an applied voltage of opposite polarities in the open DMF systems. In this study, three electrodes are actuated as schematically shown in Figure 4-1b, where the middle electrode is actuated with the opposite polarity of that of the two side electrodes. The fluid circulation will be similar to the streamlines shown in Figure 4-1b. However, other combinations of the electrodes (two or four) have also been tested and successful mixing has been achieved. The choice of the number of the electrodes depends on the size of the droplet to generate a proper gradient of the electric field inside the droplet. For the closed DMF platform, any combinations of the electrodes can also be used for actuation (two or more adjacent electrodes, or the bottom and the top plate electrodes). However, the efficiency of the mixing may decrease if a smaller number of electrodes is chosen for larger droplets. Similarly, for the case of the top and bottom plate electrodes, mixing occurs but with a lower efficiency. In this chapter, three electrodes (Figure 4-1c) are chosen for the majority of the experiments with a similar actuation scheme as the open system. For the closed system, the fluid circulation primarily occurs similar to the streamlines shown in the side view of Figure 4-1c. The small circulations which occur along the axis parallel to the two plates induce larger circulation zones along the axis normal to the two plates (see the top view in Figure 4-1c). For this configuration, the top plate was also actuated with the same polarity as the two side electrodes to form a stronger gradient of the electric field within a larger portion of the droplet, enhancing the mixing process. This configuration will be used for the experiments conducted to study the effect of the salt concentration and the samples containing DNA.

4.3 Experimental setup and device fabrication

The experiments are performed on both open and closed DMF systems with air as the surrounding medium. For both cases, the bottom plate contains the actuating electrodes, covered with a $7\mu m$-parylene C and a $\sim 100nm$-cytop layer as the insulation and the hydrophobic layers, respectively. The electrodes are $1.5mm \times 1.5mm$ with a spacing of $\sim 30\mu m$, and were fabricated using standard photolithography (see Section 2.2). The parylene C layer was deposited using SCS Labcoter® 2 (PDS 2010), and the cytop layer (PFC 1603V, Cytonix Co.) was spun at $3000\ rpm$ and baked at $150°C$ for $10\ min$. The top plate for the closed system was an ITO slide coated with a cytop layer (spun at $3000\ rpm$ and baked at $200°C$ for $1\ hr$). The open system is schematically shown in Figure 4-2, with the droplet containing cells/particles (i) before and (ii) after mixing. The closed system is shown in Figure 4-3, where the dye and DI water droplets are initially placed separately (Figure 4-3a). Then, the two droplets are merged by moving them using electrowetting on dielectric (EWOD) with an applied voltage at $1kHz$ (square waveform) and $U_{rms} = 100V$ (Figure 4-3b). Finally, the droplets are mixed using the proposed electrohydrodynamic method (Figure 4-3c). A sine waveform AC voltage was used for mixing. A signal function generator (Tektronix AFG3021B0) connected in series with an amplifier (TREK PZD700 for frequencies up to $250kHz$ and Electronics & Innovation 325LA for the frequency range of $500kHz$ - $25MHz$) was used for applying the voltage.

The experiments were monitored under a microscope (Leica Z6 APO) and recorded using a Leica DFC420 camera (at the rate of 15 frames/sec with the resolution of 2592×1944 pixels).

Image processing was used for the quantification of mixing. For the case of the experiments with the beads, the number of the beads in 15 randomly distributed small boxes ($200\mu m \times 200\mu m$) were counted and the standard deviation was calculated to determine the percentage of uniformity of mixing. The boxes were selected from the entire region of the electrodes to provide an accurate representation of sample distribution. For the case of dye, the intensity of red color was measured using ImageJ software in 15 randomly chosen points on locations where are transparent (e.g., the gap between and the sides of the electrodes), and the standard deviation was calculated. For both bead and dye cases, 95% uniformity was used as the criterion for proper mixing (similar to the value used in [209]), for which the time elapsed to achieve such a value was estimated from the videos.

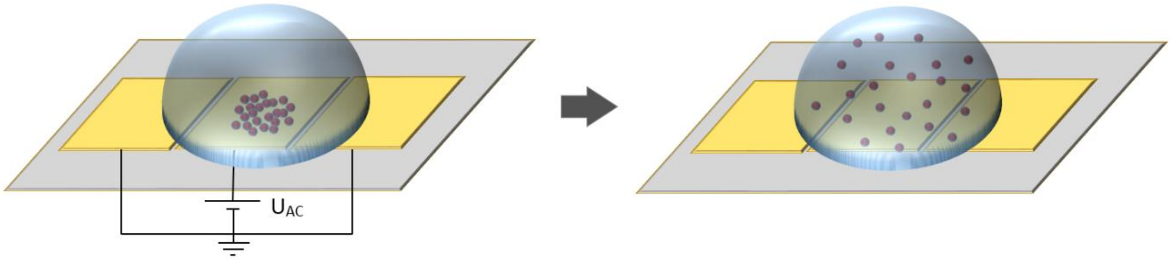

Figure 4-2 Schematic of a droplet in an open DMF system containing micron-sized particles before and after electrohydrodynamic mixing.

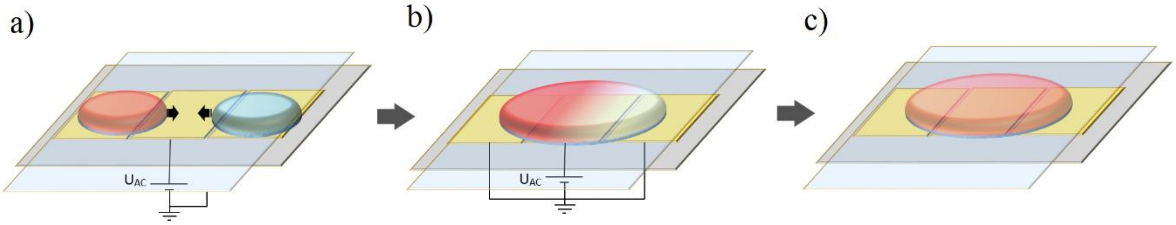

Figure 4-3 Schematic of electrohydrodynamic mixing of two droplets in a closed DMF system. The images show the sequences of (a) dispensing two different droplets on an array of electrodes, (b) merging the two droplets using EWOD, and (c) electrohydrodynamic mixing inside the merged droplet.

4.4 Materials and solutions

The solutions used for the experiments and their electrical conductivities are as follows: DI water $\sigma_{DI} = 5\mu S/cm$, DI water containing 5-μm polystyrene microbeads (Bangs Laboratories, Inc.) with a concentration of $5000\ \text{particle}/\mu l$, $\sigma_{Bead} = 50\mu S/cm$, red dye solution (Safranin-O-counterstain, Thermo Electron Co.) $\sigma_{Dye} = 400\mu S/cm$ (10 times diluted), solutions for different pH measurements $pH = 4, 7$ and 10 (Micro Essential Laboratory Inc.), $\sigma_{pH} = 1000\mu S/cm$ ($1g$ of the powder in $400mL$ of DI water), and pH measurement dye (Micro Essential Laboratory Inc.) $\sigma_{pH\,dye} = 100\mu S/cm$ (10 times diluted). A phosphate-buffered saline was used for the solutions containing salt, as it is the buffer used for the majority of the biological samples. The original sample includes $8g/l$ of NaCl, $0.2g/l$ of KCl, $1.42g/l$ of Na_2HPO_4, and $0.24g/l$ of KH_2PO_4, with a conductivity of $\sim 10mS/cm$. For the experiments including biological samples, a solution of nuclease-free water containing $250\mu g/ml$ of yellow fever mosquito DNA was used.

4.5 Results and discussions

4.5.1 Proof of concept

The electrohydrodynamic mixing was first performed for the open DMF system. The experiments were only performed with beads, as generating non-uniform dye concentration in open system was difficult. A $12\mu l$-droplet of DI water was placed on the array of electrodes such that it covered one electrode and was in touch with the two side electrodes (Figure 4-2). Then, a $0.5\mu l$-droplet containing a high concentration of $5\mu m$ polystyrene beads ($\sim 30{,}000\ \text{particle}/\mu l$) was gently injected into the DI water droplet in a way that the beads were accumulated in the center of the droplet (left image of Figure 4-4a). Afterwards, a voltage with the frequency of $f = 50kHz$ and the amplitude of $U_{rms} = 75V$ was applied to the electrodes (the circuit shown in Figure 4-2a). It was observed that mixing happened almost instantly. Figure 4-4a shows the droplet containing the beads before (left image) and after mixing (right image). A variety of voltages with frequencies between $f = 25kHz$ to $f = 250kHz$ and the amplitudes between $U_{rms} = 50V$ to $U_{rms} = 200V$ were used for the experiment, and for all cases very rapid mixing was observed. Since the mixing time for all cases was less than $t = 1s$, a characterization curve was not included here.

For the closed DMF system, the experiments were performed for both bead and dye cases. The gap height between the top and bottom plates was set to $h = 250\mu m$. As shown in Figure 4-4b and c, the droplets of beads or dye, and the water droplet were placed separately. By actuating the middle electrode and the top plate, both droplets were pulled towards the middle electrode using EWOD (see the circuit shown in Figure 4-3a), which resulted in merging them (middle frame in Figure 4-4b and c).

Afterwards, the three electrodes on the bottom plate were actuated ($f = 50kHz$ and $U_{rms} = 75V$), using the circuit shown in Figure 4-3b, to perform electrohydrodynamic mixing. The 95% mixing happened for the case of the experiment with dye in $t = 1s$ and for the beads in $\sim 0.9s$. For other frequencies and amplitudes of the applied voltage, the mixing time was observed to be less for the case of experiments with the beads (as compared to the experiments with dye), which is possibly because of forming a higher gradient of the electric field due to the presence of the beads, as well as the lower electrical conductivity of the solution of beads. Therefore, the parametric characterization is performed only for the dye case, shown to have longer mixing time. The results presented below were repeated three times to ensure reproducibility, and a standard deviation of less than 3% were observed for all cases.

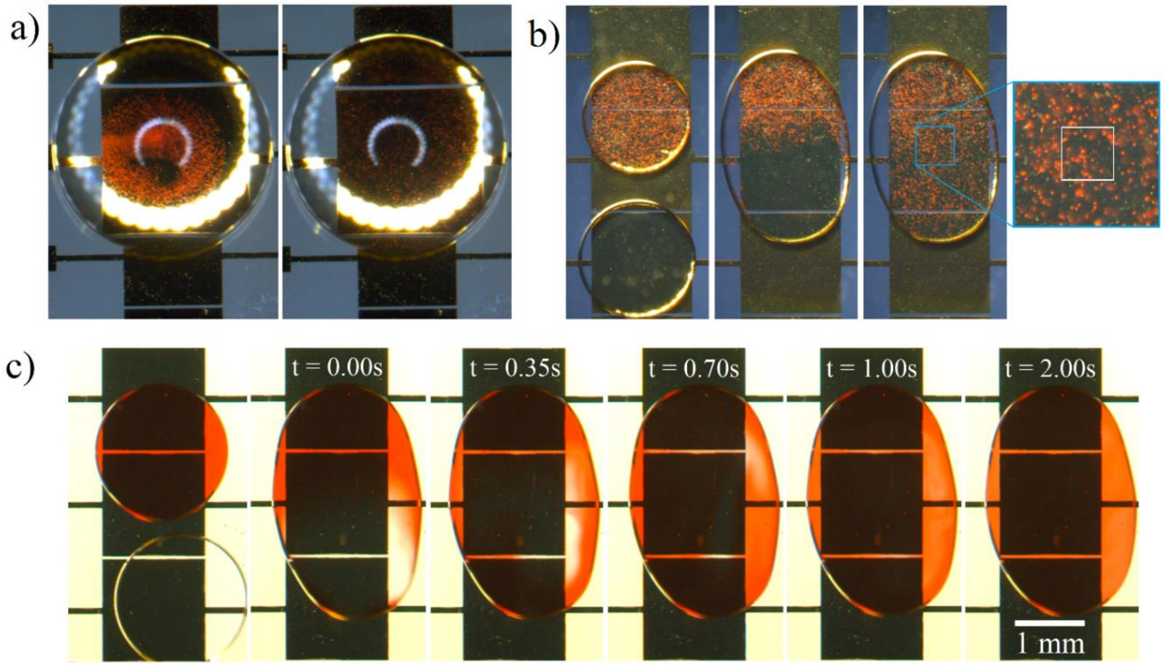

Figure 4-4 Experimental images of electrohydrodynamic mixing on DMF devices. a) Sequences of images taken prior and after droplet mixing in an open DMF system. b) Sequences of merging and mixing of a droplet containing 5-$\boldsymbol{\mu m}$ polystyrene microbeads and a droplet of DI water in a closed DMF system. The white square in the zoomed image shows a sample box used for particle counting. c) Sequences of merging and mixing a droplet of dye with DI water in a closed DMF system. The 95% mixing was achieved within $1s$.

4.5.2 Parametric study

4.5.2.1 Effect of applied voltage

The effects of the frequency and the amplitude of the applied voltage were first studied for the gap height of $h = 250\mu m$, and the 95% mixing time was measured. The results are illustrated in Figure 4-5. For frequencies less than $f = 10kHz$ no mixing was observed (regardless of the amplitude). For values higher than $f = 10kHz$ the increase in the frequency and/or the amplitude of the applied voltage enhances the mixing effect, requiring a shorter time for the applied voltage (down to around $t = 0.25s$). For a low range of frequency (between of $f =$

$10kHz$ and $f = 25kHz$) the mixing time was fairly long except for very high voltages ($U_{rms} = 175V - 200V$) which resulted in mixing time of more than $t = 1s$. However, at these high voltages the droplet sheds pico-liter satellite droplets due to high accumulation of electric charges around the three-phase contact line [36]. For a higher range of the frequencies ($f = 50kHz$ and $f = 100kHz$), on the other hand, a mixing time of less than $t = 1s$ was achieved for $U_{rms} = 75V$ or higher. For these cases the pico-liter satellite droplets were started to shed for the applied voltages higher than $U_{rms} = 125V$. This means that a rapid mixing effect can be achieved with such frequencies when the amplitude is kept within $U_{rms} = 75V - 125V$. For the case of $f = 250kHz$, the 95% mixing time was achieved in less than $t = 1s$ for the whole range of the applied voltage ($U_{rms} = 15V - 200V$). However, for this frequency the pico-liter satellite droplets were observed for the voltages around $U_{rms} = 75V$.

4.5.2.2 Effect of gap height between two plates

The effect of the gap height on the mixing time was also studied. For this purpose, three gap heights of $h = 150, 250$ and $350\mu m$ were tested while the applied voltage was kept at $U_{rms} = 75V$ which was low enough for all studied frequencies without observing pico-liter satellite droplets. For these experiments, the droplet volume was adjusted ($\sim 0.9, 1.5$ and 2.1 μl for $h = 150, 250$ and $350\mu m$, respectively) to keep the contact area constant ($\sim 5.9mm^2$). It is expected that for larger gap heights a shorter mixing time is achieved, as an increase in the gap height decreases the viscous effect exerted by the two plates (due to the no-slip condition). As a result, the circulation zones can be formed easier.

The results, which are shown in Figure 4-6, confirm that the mixing time decreases when the gap height increases. For the gap height of $h = 150\mu m$ the shortest mixing time is $t = 1.8s$ which occurs at $f = 250kHz$. Shorter mixing times (less than $1s$) are achieved at much lower frequencies for the gap heights of $h = 250\mu m$ and $h = 350\mu m$ (e.g., at $f = 100kHz$, the mixing times are around $t = 4.5s$, $t = 1s$ and $t = 0.25s$ for $h = 150\mu m, h = 250\mu m,$ and $h = 350\mu m$, respectively). For the gap height of $h = 350\mu m$ the mixing time ranges between $t = 0.25s$ to $t = 0.4s$ for the entire range of frequency.

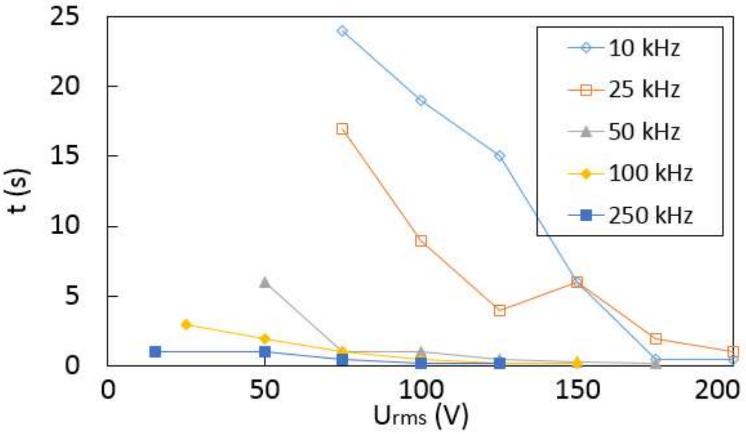

Figure 4-5 Experimental results of droplet mixing for the case of the dye using the electrohydrodynamic effect in a closed DMF system. The time required to achieve 95% mixing versus the amplitude of the applied AC voltage for different frequencies ranging between $10kHz$ to $250kHz$ is shown. The gap height is set to $250\mu m$ and the dimension of the square actuating electrodes is $1.5mm$.

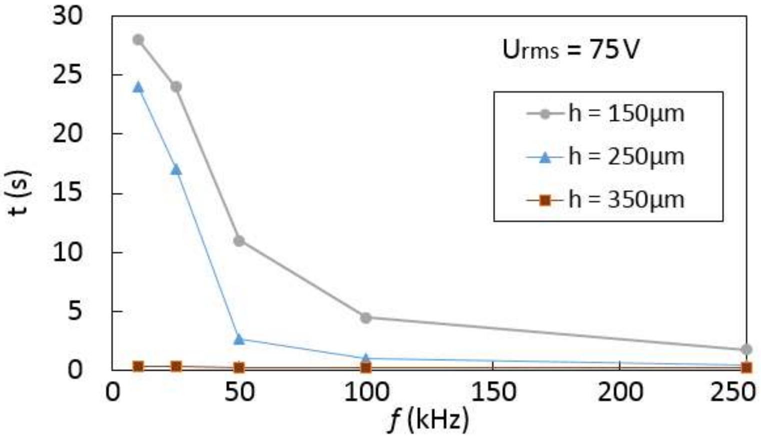

Figure 4-6 The effect of the gap height between the two plates on the mixing time is presented. Three gap heights of $150, 250$ and $350\mu m$ were tested for which the droplet volume was adjusted to keep the contact area constant. For all cases the amplitude of the applied voltage is $75V$.

4.5.2.3 Effect of droplet size

The effect of the droplet size (contact area) on the mixing time was also studied. For this purpose two different droplet volumes (merged droplets) of $0.65\mu l$ and $0.45\mu l$ were used which resulted in the contact areas of $5.95mm^2$ and $3.94mm^2$, respectively. These areas are 2.62 and 1.73 times the area of one actuating electrode, respectively. The mixing was performed with the voltage of $f = 100kHz$ and $U_{rms} = 25V$. The mixing time for the larger droplet was $t = 3s$ while it was around $t = 1s$ for the smaller droplet. To double check this effect in a different range of the voltage, the applied voltage was set to $f = 50kHz$ and $U_{rms} = 100V$. This resulted in a mixing time of $t = 1s$ for the larger droplet and $t = 0.5s$ for the smaller droplet. This shows that the electrohydrodynamic mixing is more efficient for droplets with smaller volumes.

4.5.2.4 Effect of salt concentration

Adding salts to the solution, which increases the concentration of ions, may affect the electrothermal and consequently mixing process inside the droplet. This effect depends on the solubility and dissociation rate of the salt and may be different for different salts. In this section, a series of experiments were performed for the case of beads to study the effect of the salt concentration on mixing using phosphate-buffered saline (PBS). PBS was used as the solution for both droplets, with and without beads, which contains around $10mg/ml$ of different salts. Solutions with different concentrations of PBS were prepared for the experiments (from $0.5mg/ml$ to $10mg/ml$). It was observed that for the frequency range of up to $250kHz$, no mixing happened inside the droplet. Therefore, a higher range of frequency (up to $25MHz$) was used for the mixing process. For all ranges of the salt concentrations, there was a certain threshold frequency below which no mixing was observed. Increasing the frequency higher than the threshold value resulted in rapid circulation, and hence mixing within the droplet (below $1s$ mixing time). It was observed that for higher concentrations of the salt solution, the threshold frequency was higher. For all experiments, the mixing happened for the range of the applied voltage of $U_{rms} = 20V - 40V$. Figure 4-7 shows the threshold frequency (f_{min}) versus the salt concentration (c) in the samples.

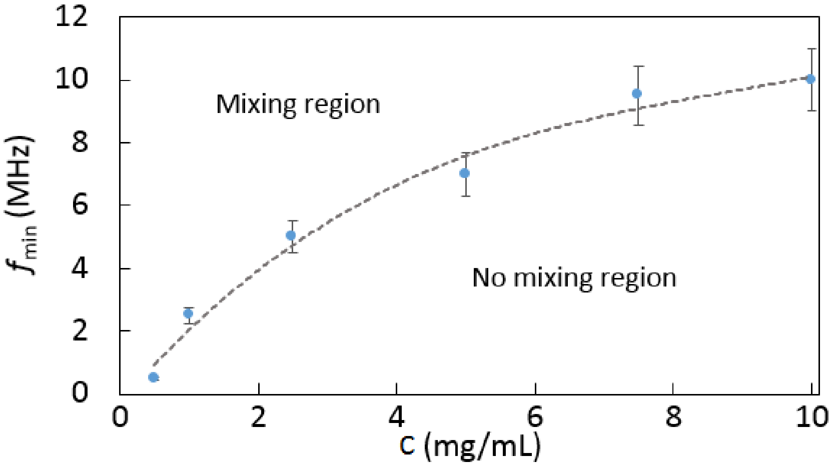

Figure 4-7 The effect of the salt concentration on mixing is shown. Different concentrations of the salt ($0.5mg/ml$ to $10mg/ml$) were added to the samples (including the beads) to identify a minimum required frequency for mixing.

For majority of the cases presented in Figure 4-7 the satellite droplets appeared during the mixing process. It has to be mentioned that the dielectric material used for chip fabrication here (i.e., Parylene C) has weak dielectric properties. Thus, the use of a material with a high dielectric constant and smaller thickness as the insulating layer can potentially decrease the required voltage/frequency for mixing, and hence the chance of the formation of satellite droplets. The use of other surrounding media (such as silicone oil) might also be helpful to avoid satellite droplets.

4.5.3 Applications

In order to show the practicality of the proposed method for DMF-based lab-on-a-chip applications, mixing is performed for two types of samples containing 1) pH indicators, and 2) DNA. The pH test is a simple application, yet very suitable for the current study as the pH measurement is performed in a colorimetric fashion. The measurement is based on mixing the pH measurement dye with a solution of an unknown pH. Depending on the pH value of the solution, the color of the mixed droplet changes. Figure 4-8 shows the experiments for three different colorless buffers with pH values of $4, 7$ and 10 (Figure 4-8a, b and c, respectively). For all cases the left droplet in the top image is the buffer with different pH values, and the right droplet is the measuring buffer. The droplets were merged on the middle electrode using EWOD and mixed using the current electrohydrodynamic method at $f = 250kHz$ and $U_{rms} = 75V$. With a mixing time of less than $1s$, uniform colors of yellow, green and blue were observed for the pH values of $4, 7$ and 10, respectively.

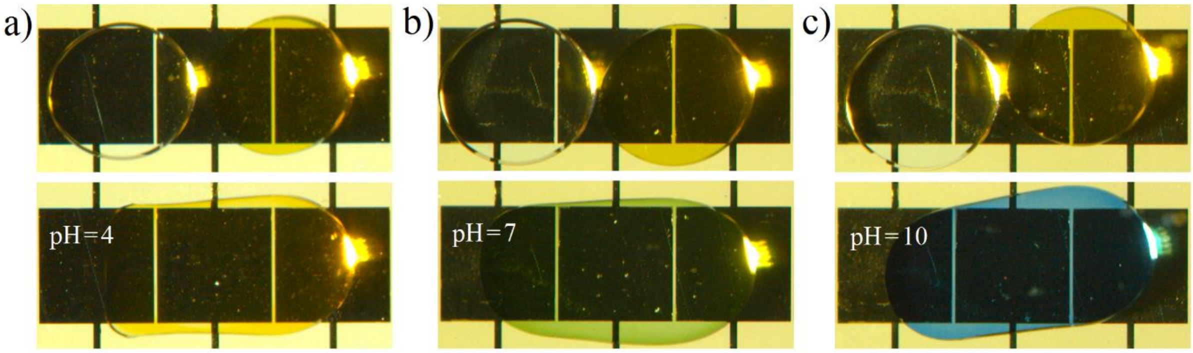

Figure 4-8 Application of the electrohydrodynamic mixing method for colorimetric pH measurement on the closed DMF platform. a) pH $= 4$, b) pH $= 7$ and c) pH $= 10$. For all cases the top image shows the colorless liquid with specific pH (left) and the pH measurement dye (right), and the bottom image shows the merged droplet after electrohydrodynamic mixing.

For the solution containing DNA, the experiment was performed for a droplet of nuclease-free water containing $250\mu g/ml$ of yellow fever mosquito DNA and a droplet of the beads. It was observed that the addition of DNA to the sample has a similar effect as that of the salt, i.e., suppressing the electrothermal effect. Therefore, for the low range of frequencies mixing was not observed. Using a frequency of $f = 25MHz$ and amplitude of $U_{rms} = 40V$ rapid circulation and hence mixing was generated inside the merged droplet. The sequences of the images illustrating the mixing process are shown in Figure 4-9. As it can be observed in the third and fourth frames of Figure 4-9, satellite droplets form around the main droplet. Similar to the salt experiments, this might be solved by fabricating the chip with a high-dielectric insulating layer or using oils compatible with the biological material as the surrounding medium.

This method will be applicable to a variety of biochemical and cell-based applications, for which it has been shown that the viability of the cells is not hampered in moderate to high applied AC voltages (the value of voltage depends on the chip configuration) [210, 212, 213]. In addition, for biosensing purposes the current mixing method has the potential to be used to circulate the liquid on the sensing spot without moving the droplet. This increases the chance of the target analytes (or cells) to be exposed to the bio-receptors. However, for each application, it is required to characterize the range of the applicable voltage and frequency, and also the viability of the biomolecules.

4.6 Summary

An electrohydrodynamic technique for mixing in a stationary droplet in both open and closed digital microfluidic (DMF) platforms was developed. Mixing was generated by applying high frequency voltages to the actuating electrodes (used for droplet manipulation). The advantages of this method are the stationary nature of the technique, a shorter mixing time, and the use of a fewer number of electrodes (1 to 3) as compared to the conventional mixing method, reducing the chance of cross-contamination and surface biofouling. The experimental results showed that the increase in the amplitude and/or the frequency of the applied voltage enhances the mixing effect. However, at high amplitudes, pico-liter satellite droplets were generated due to the high accumulation of electric charges at the three-phase contact line. Therefore, for each frequency there is an effective range of the amplitude of the applied voltage that provides proper mixing without shedding satellite droplets. In addition, for the closed DMF system, the increase in the gap height between the two plates and the decrease in the droplet volume were found to shorten the mixing time significantly. Experiments were also performed with samples containing salts as well as DNA. It was found that the electrothermal effect is suppressed. To generate the mixing effect inside the droplet, the frequency range of the applied voltage has to be increased for these cases.

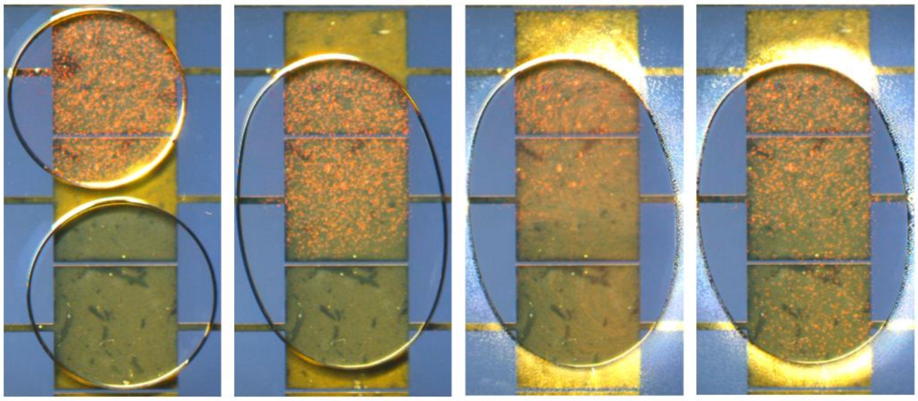

Figure 4-9 The sequences of the images show merging and mixing of a droplet of nuclease-free water containing $250\mu g/ml$ of yellow fever mosquito DNA with a droplet of the beads. At a frequency of $f = 25MHz$ and amplitude of $U_{rms} = 40V$ rapid circulation and hence mixing was observed inside the merged droplet.

Chapter 5 Development of a dielectrophoretic-gravity driven particle focusing technique for digital microfluidic systems[4]

5.1 Overview

Several particle (or cell) manipulation techniques [214, 215] have been developed based on the hydrodynamic [116], magnetic [125], optic [123, 216], electrophoretic [129] and dielectrophoretic [59, 114, 130] effects, as one of the key steps in the use of the digital microfluidic (DMF) devices for the biochemical applications. Among these methods, dielectrophoresis has shown to be effective in manipulation of a wide range of the particles [217, 218] as it does not require any auxiliary elements [59]. Despite the efficiency of DEP in manipulation of particles [217, 219], the current ways of its implementation into the DMF platforms still requires a change in the shape of the conventional square electrodes used for manipulation of droplets.

This chapter presents a dielectrophoretic-gravity driven (DGD) particle focusing approach operating based on the cumulative effects of gravity and DEP. It is shown that this method can efficiently focus the non-buoyant particles (with a density as low as $1.06\ g/m^3$) on the center of the conventional square electrode designs. Therefore, the conventional electrodes used for droplet manipulation can be used to focus the particles using the proposed DGD method without any modifications to the electrodes. The effects of the parameters such as the magnitude of the applied voltage, the particle size and density, and the electrode size on the focusing behavior of the particles are studied. Finally, a potential application of this technique is illustrated for particle concentration in DMF.

---

[4] Parts of this chapter have been published in Applied Physics Letters (E. Samiei et al., *App. Phys. Lett.*, (2015), 106, 204101).

5.2 Theory

In the presence of a non-uniform electric field, a particle and its surrounding medium are polarized. If the dielectric constant of the particle is different than that of the surrounding medium, a dipole moment is created [220] which exerts a force on the particle, moving it toward the high intensity (positive dielectrophoresis (pDEP)) or low intensity (negative dielectrophoresis (nDEP)) part of the electric field [221]. The Clausius-Mossotti factor ($K(\omega) = \left(\varepsilon_p^* - \varepsilon_m^*\right)/\left(\varepsilon_p^* + 2\varepsilon_m^*\right)$) [221] defines the DEP behavior of the particle. Here, ω is the frequency of the applied field, and ε^* is the complex permittivity ($\varepsilon_{p,m}^* = \varepsilon_0\varepsilon_{p,m} - i\sigma_{p,m}/\omega$, where ε_0 is the vacuum permittivity, and $\sigma_{p,m}$ and $\varepsilon_{p,m}$ are the conductivity and relative permittivity of the particle or the medium, respectively). The DEP force acting on the particle is expressed as $\vec{\boldsymbol{F}}_{DEP} = 2\pi\, r^3\varepsilon_0\varepsilon_m\, \mathrm{Re}\left(K(\omega)\right) \vec{\boldsymbol{\nabla}} \left(\left|\vec{\boldsymbol{E}}\right|^2\right)$, where r is the particle radius, Re denotes the real part of the complex number, and $\vec{\boldsymbol{E}}$ is the electric field (see Figure 5-1) [114]. A particle in a quiescent fluid also experiences the gravitational force which is expressed as $\vec{\boldsymbol{F}}_g = (4/3)\,\pi\, r^3\left(\rho_p - \rho_m\right)\vec{\boldsymbol{g}}$, where ρ_p and ρ_m are the density of the particle and the surrounding liquid, respectively. In the present technique, the gravitational force is used to sediment the particles inside the droplet located on the electrode; while the nDEP force is used to push away the particles from the edges of the electrode and concentrate them in the center of the electrode. The nDEP force acting on the particles has two components: a horizontal component that drives the particles away from the edges of the electrode, and a vertical component that levitates the particles located on the electrode (acting against gravity) and repels the particles toward the area outside of the electrode. Therefore, to focus the particles on the center of the electrode, the vertical component of the nDEP force should be less than the gravitational force on the electrode area to avoid particle levitation.

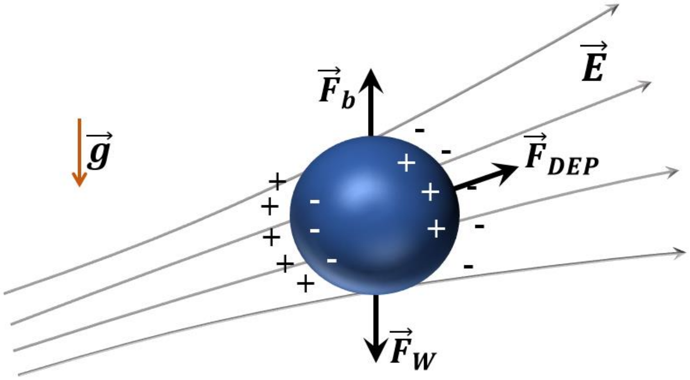

Figure 5-1 Schematic of the forces acting on a particle in a non-uniform electric field.

The total vertical force acting on the particles is expressed as

$$F_v = \vec{\boldsymbol{F}}_{DEP_v} - \vec{\boldsymbol{F}}_{g_v} = r^3\,(\mathrm{A} - \mathrm{B} \times \Delta\rho) \tag{5-1}$$

where $\mathrm{A} = 2\pi\,\varepsilon_0\varepsilon_m\,\mathrm{Re}(K(\omega))\left(\vec{\nabla}\left(|\vec{\boldsymbol{E}}|^2\right)\right)_v$, $\mathrm{B} = (4/3)\,\pi\,\vec{\boldsymbol{g}}_v$ and $\Delta\rho = \rho_p - \rho_m$. Equation (5-1) can be used to describe the effect of the particle radius and density on the focusing behavior of the particles. In the Equation (5-1), the size of the particle (r) only acts as a gain factor. In other words, if the particles are focused, increasing the particle size enhances the focusing behavior, and if the particles are repelled away from the electrode, increasing the particle size accelerates the process. On the other hand, the density difference between the particle and the medium ($\Delta\rho$) not only acts as a gain factor, but also determines whether the particle can be focused.

5.3 Experimental procedure

The experiments were performed using samples of DI water (measured conductivity of 2 µS/cm) containing micro-particles. Three different particles used were silica particles (ρ =

$2.5\ g/cm^3$) with the diameter of $5\ \mu m$ (SI-5) and polystyrene particles ($\rho\ =\ 1.06\ g/cm^3$) with the diameters of 5 and $15\ \mu m$ (PS-5 and PS-15, respectively). The samples of SI-5 and PS-5 contain around 2.7×10^4 $\text{particles}/\mu L$, and the PS-15 sample contains around 10^3 $\text{particles}/\mu L$. For all experiments, a $20\mu L$ droplet (containing 5.4×10^5 particles for PS-5 and SI-5 and 2×10^4 particles for PS-15) was dispensed on the chip and squeezed with the top plate held by a set of spacers at the gap height of $h = 320\ \mu m$. The diameter of the squeezed droplet is significantly larger than the electrode so that the droplet interface is away from the electrode edges to minimize the effect of the interface on the distribution of the electric field around the test region.

The schematic of the experimental setup is shown in Figure 5-2. A square-wave AC (alternating current) voltage with a variable amplitude was applied to the system using a signal function generator (Tektronix AFG3021B0) and amplifier (TREK PZD700). The frequency was chosen $1\ kHz$ for droplet transport using electrowetting on dielectric [36] (EWOD) and then increased to $10\ kHz$ when particle manipulation was performed using the dielectrophoretic-gravity driven (DGD) method. When $1\ kHz$ voltage is applied for droplet manipulation, a slight DEP force will be applied to the particles. However, the duration of electrode actuation for droplet transport is $0.5\ s$ which is very short for the particles to be moved by DEP. Also, the magnitude of DEP force on the particles will not be significant until the frequency is increased to $10\ kHz$. The chosen frequency of $f = 10\ kHz$ results in nDEP for all particles used here. The experiments were monitored using a camera connected to an Apo-zoom microscope (Leica Z6 APO).

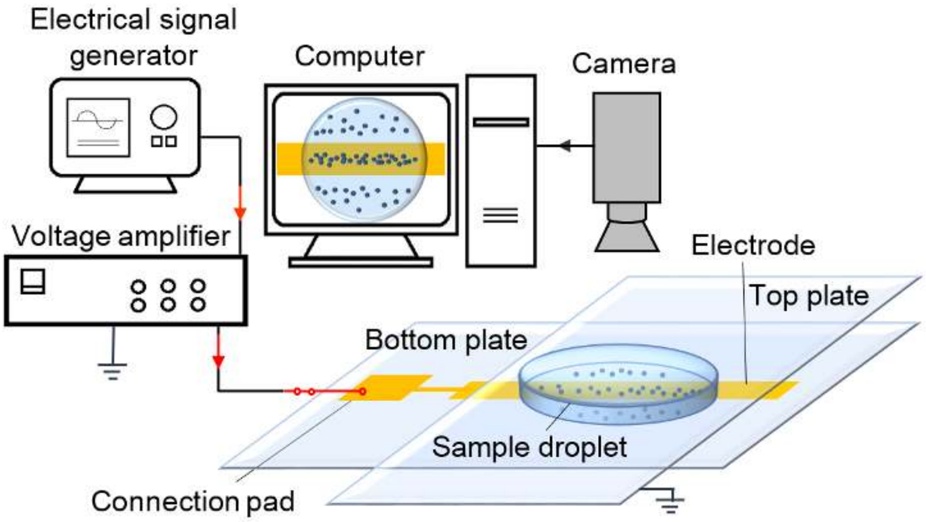

Figure 5-2 Schematic of the experimental setup.

5.4 Numerical simulation

A numerical model has been developed to study the particle motion in the liquid due to the DEP and gravitational forces. The geometry and boundary conditions for the model are shown in Figure 5-3. To study the motion of the particles, the Laplace equation for the electrostatic condition of the electromagnetic field [59] is solved using the finite volume method.

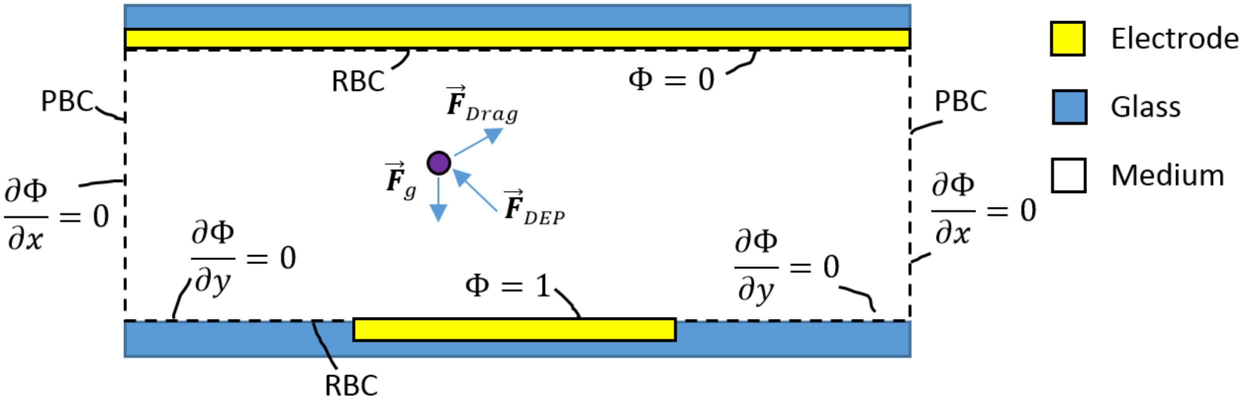

Figure 5-3 The solution domain and boundary conditions for the numerical method.

$$\nabla^2\Phi = \frac{\partial^2\Phi}{\partial \mathrm{x}^2} + \frac{\partial^2\Phi}{\partial \mathrm{y}^2} = 0 \tag{5-2}$$

here, Φ is the electrostatic potential. The Dirichlet boundary condition is use for the top and bottom electrodes. The Neumann boundary condition is applied to other boundaries surrounded the domain [59]. In the simulation, the particle–particle interaction is not considered. Also, the effect of particle polarization on the electric field is assumed to be negligible.

The electric field in the simulation domain is calculated by

$$\vec{\boldsymbol{E}} = -\vec{\boldsymbol{\nabla}}\Phi \tag{5-3}$$

To predict the motion of the particles in the droplet, the Newton's equation of motion is solved with the velocity Verlet algorithm [222]. The equation that describes the motion of the particles can be written as follows:

$$m_p \frac{d\vec{\boldsymbol{u}}_p}{dt} = \sum \vec{\boldsymbol{F}} \tag{5-4}$$

where, m_p and $\vec{\boldsymbol{u}}_p$ are the mass and the velocity of the particles. In the simulation, 200 particles are considered, which are randomly distributed in the domain. The top and bottom boundaries are considered as a reflective boundary condition (RBC) and all other boundaries are considered periodic boundary condition (PBC) [222]. The particles in the liquid experience three major forces including: DEP, the gravitational force and the viscous drag force. These forces can be calculated based on the following equations:

$$\vec{\boldsymbol{F}}_{DEP} = 2\pi\, r^3 \varepsilon_0 \varepsilon_m \,\mathrm{Re}\big(K(\omega)\big)\, \vec{\boldsymbol{\nabla}}\left(\left|\vec{\boldsymbol{E}}\right|^2\right) \tag{5-5}$$

$$\vec{\boldsymbol{F}}_g = (4/3)\,\pi\, r^3 \big(\rho_p - \rho_m\big)\, \vec{\boldsymbol{g}} \tag{5-6}$$

$$\vec{\boldsymbol{F}}_{Drag} = -6\pi\mu r \vec{\boldsymbol{u}}_p \tag{5-7}$$

where r is the radius of the particle, ρ_p and ρ_m are the particle and medium density, respectively, and μ is the medium viscosity. The term $\vec{\nabla}\left(\left|\vec{\boldsymbol{E}}\right|^2\right)$ in the DEP force is calculated based on the electric field predicted in the domain using the Equation (5-3).

5.5 Results and discussion

5.5.1 Proof of concept

Here, it is shown that it is possible to focus the particles inside the sample droplet in the center of the electrode using DGD. As shown in Figure 5-4, a $20\mu L$ sample of PS-15 is deposited on a $1.5mm$ square electrode, covering an area much larger than the electrode.

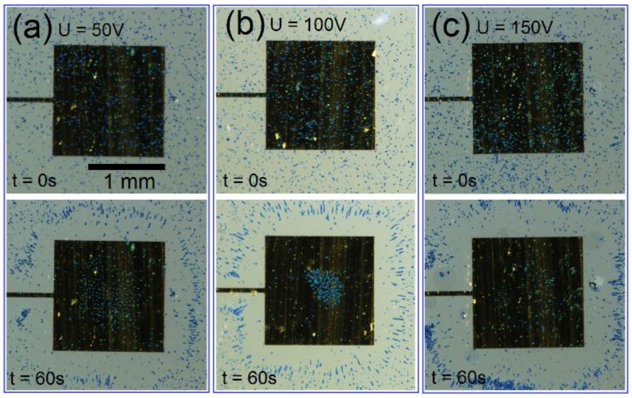

Figure 5-4 Manipulation of PS-15 particles inside the $20\mu L$ sample on a square electrode of $1.5mm$ using voltages with a frequency of $f = 10kHz$ and amplitudes of (a) $U = 50V$, (b) $U = 100V$, and (c) $U = 150V$. For each case, the top image is the initial position of the particles and the bottom image is after $t = 60s$.

Three different voltages of $U = 50, 100$ and $150\ V$ (Figure 5-4a, b and c, respectively) are applied to the system. For the case of $U = 50\ V$ (Figure 5-4a), the particles are repelled away from the edges. Thus, the particles which are initially in the region above the electrode move toward the center of the electrode, and the particles initially outside the electrode are moved away from the electrode. The particles initially on the electrode are focused into a region with the normalized area of $\alpha_f = 33.3\%$ (where α_f is the ratio of the focused area over the area of the electrode), which corresponds to the normalized number of the focused particles of $N = 3$ ($N = n_f/n_i$, where n_f and n_i are the final and initial number of particles on the focused region, respectively). When the voltage is increased to $U = 100\,V$ (Figure 5-4b), the focusing behavior will be more significant as particles are focused into a smaller region. In this case, $\alpha_f = 8\%$ and $N = 12.5$. On the other hand, when the voltage is further increased to $U = 150\,V$ (Figure 5-4c), the particles initially located on the electrode are lifted up from the bottom plate and repelled away from the electrode, leaving the region on the electrode with a very low (or no) concentration of the particles.

5.5.2 Physics of phenomenon

To understand the physics of the phenomenon, particle focusing using the proposed technique is simulated using an in-house code (see Figure 5-5). The properties of PS-15 were used in the simulation. The simulations were performed for $U = 100$ and $150\,V$, as shown in Figure 5-5a and b, respectively.

For each case, the top image shows the contour of the sign of the difference between the gravitational and the vertical component of the DEP forces ($e = sign\{|\vec{\boldsymbol{F}}_g| - |\vec{\boldsymbol{F}}_{DEP,v}|\}$). This contour also reflects the effect of the magnitude of the electric field, since $\vec{\boldsymbol{F}}_{DEP,v}$ is proportional to $|\vec{\boldsymbol{E}}|^2$. The other three images show the position of the particles at $t = 0s,\ 30s$, and $60s$ and the contour of the magnitude of the electric field ($|\vec{\boldsymbol{E}}|$). Based on the parameter e, two regions are defined in the simulation domain: lifting (white) and sedimentation (grey) regions. In the lifting region (white) $e < 0$. Thus, the net force is upward and the particles which are initially in this region will be lifted. On the other hand, in the sedimentation region (grey) $e > 0$, and hence, the particles initially located in this region will sediment due to the dominant effect of the gravitational force.

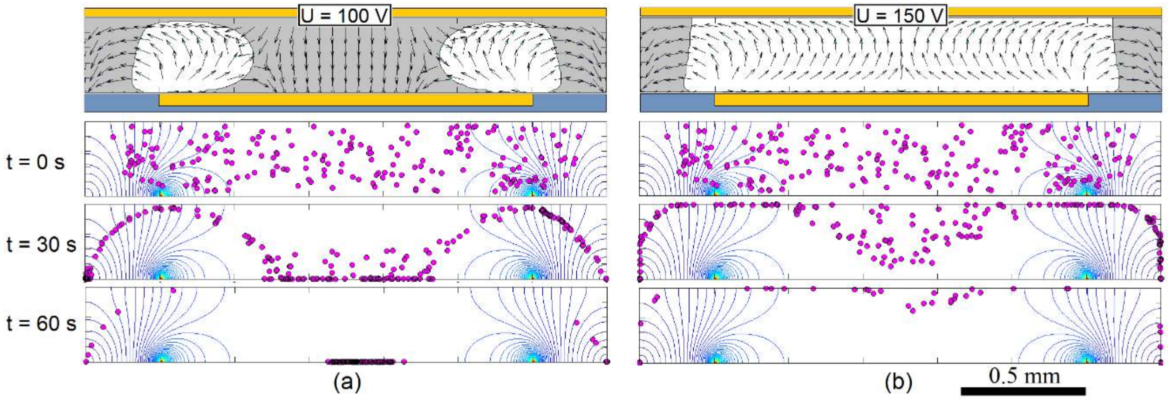

Figure 5-5 The simulation results for particle focusing are presented. The electrode size at the bottom plate (with golden color and the size of $1.5mm$) is 5 times the gap height between the two plates and the properties of PS-15 are used for the particles in the simulation. (a) $U = 100V$ and (b) $U = 150V$. For both cases the top image shows the contour of the sign of the difference between the gravitational force and the vertical component of the DEP force ($e = sign\{|\vec{F}_g| - |\vec{F}_{DEP,v}|\}$), where in the white region $e < 0$ and in the grey region $e > 0$. The vectors on the top images show the direction of the net force (not in scale). The lower three images show the position of the particles at $t = 0s, 30s$ and $60s$. The contour of the magnitude of the electric field is also shown in the three lower images.

When the voltage of $U = 100\ V$ (Figure 5-5a) is applied, e becomes positive in the major part of the region over the electrode; thus, over time, most of the particles which are initially in the area over the electrode will sediment (mostly between $t = 0s$ to $t = 30s$). The horizontal component of the nDEP force repels the sedimented particles from the edge and focuses them on the center of the electrode (more noticeably between $t = 30s$ to $t = 60s$) where the width of the focused region decreases (α_f reduces from 33% to 13%). For the case of $U = 150\ V$

(see Figure 5-5b), e is negative in the whole region over the electrode, showing the dominant effect of the vertical component of the nDEP force. As a result, the particles over the electrode are lifted up and scattered in the region outside the electrode. As shown in $t = 60s$, most of the particles have been pushed out of the domain. If the electrode activation continues over $60s$, all particles are expected to leave the region above the electrode. This shows that it is important to keep the applied voltage within a range to have an efficient focusing behavior. In essence, the magnitude of the applied voltage must be large enough to manipulate the particles towards the desired direction, but not too large to remove the particles from the desired region.

5.5.3 Parametric study

The effects of the magnitude of the applied voltage, the particle size and density, and the electrode size on the focusing behavior of the particles are studied. An electrode is fabricated with the width and length of 1.5 mm and $50mm$, respectively. All the three types of particles (SI-5, PS-5 and PS-15) are focused using this electrode with three different magnitudes of the voltage. The results of the experiments after $t = 60s$ are shown in Figure **5-6** and Table **5-1**. The parameter N in the graphs represents the normalized number of the particles. To obtain N, the electrode is divided to 15 smaller stripes, in each of which the number of the particles were counted. As a result, each data point in Figure **5-6** represents the average value for the local stripe ($N = n_f/n_i$ where n_f and n_i are the final and initial number of particles on each stripe). In general, for low applied voltages the focusing behavior is not significant, and for voltages with a very high magnitude the particles are repelled away from the electrode. Therefore, for each particle type an effective range is chosen. The maximum values of N and the relevant α_f are presented in Figure **5-6** for all cases. For the SI-5 particles, which have a relatively high density ($2.5\ g/m^3$) the voltages are chosen as $U = 45\ V, 60\ V$, and $75\ V$. As shown in

Figure **5-6**a, for the low voltage ($U = 45\ V$) the focused region is wide ($\alpha_f = 45\%$) with $N_{max} = 4$. As the voltage is increased, the width of the region of the focused particles decreases and the local concentration in the central region increases. It can be observed that $N_{max} = 10.8$ is achieved in $\alpha_f = 8\%$ after applying the voltage for $60s$. Figure **5-6**b shows the results for PS-15 for $U = 45\ V, 75\ V$ and $100\ V$. The density of these particles is very low ($\rho_p = 1.06\ \mathrm{g/m^3}$) while they have a large diameter ($D = 15\ \mu m$).

The focusing behavior for PS-15 is similar to that observed for SI-5. However, the concentrated region is wider ($\alpha_f = 25\%$) and $N_{max} = 4.5$ which is smaller by 58.3% . For slightly higher voltages, the particles start to be lifted up and moved away from the electrode. Figure **5-6**c shows the results for PS-5 for $U = 45\ V, 60\ V$, and $75\ V$. The density of these particles is similar to that of PS-15; however, they have a smaller diameter ($D = 5\mu m$). Based on the results shown, N barely exceeds unity. Even for low applied voltages, a considerable portion of the particles are repelled away from the electrode. A focusing region is observed for $U = 75\ V$. However, $N_{max} = 1.5$ and the size of the focused region is very thin ($\alpha_f = 4\%$). For applied voltages higher than $U = 75V$, almost all the particles are repelled away from the electrode. As explained in Theory Section (see Equation (5-1)), the particle size solely acts as a gain factor. Here, by decreasing the size of the PS particles from $15\mu m$ to $5\mu m$, particle focusing can still be observed, but the focusing behavior is suppressed adversely. On the other hand, the comparison between the results obtained for PS-5 and SI-5 shows that by increasing the density difference between the particles and the medium ($\Delta\rho$ for SI-5 is 25 times higher than that of PS-5) the normalized number of the focused particles (N) was improved by a factor of 7.5.

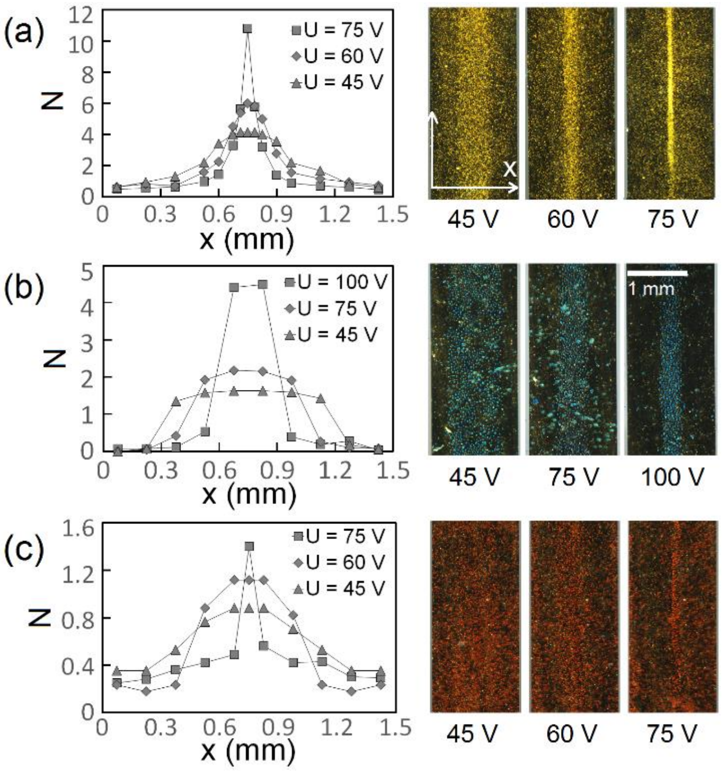

Figure 5-6 Particle focusing using long electrodes with the length of $50mm$ and the width of $1.5mm$ (here only $3.3\ mm$ of the length of the electrodes are shown). (a) SI-5, (b) PS-15, and (c) PS-5 particles. For each case, the right images show the focused particles at $t = 60s$ and the left graphs are the normalized local number of the particles ($N = n_f/n_i$) along the width of the electrode ($0 < x < 1.5mm$). To obtain the values for N, the electrodes were divided to 15 smaller stripes along x, and N represents the average value of n_f/n_i in each stripe. The sample droplet is $20\ \mu L$ and the gap height is $h = 320\mu m$ for all cases.

The effect of the width of the electrode is studied by fabricating four electrodes with the width of $w = 0.4, 0.6, 1$ and $1.5\ mm$. The PS-15 particles and a constant voltage of $U = 75V$ are chosen for all cases. As shown in Figure 5-7, for the electrode width larger than $0.6\ mm$, a focusing behavior is observed; while for the $0.4mm$ electrode, no focusing region can be seen. Also, for wider electrodes, the distance between the high concentration region and the edge of the electrode does not change significantly for different electrode widths; while the size of the focused region increases significantly as the electrode size increases. This shows that for a certain set of parameters, there is a limit for the electrode size to achieve particle focusing. Below this limit all the particles will be repelled away from the electrode.

Table 5-1 Maximum normalized number of the particles (N_{max}) and the ratio of the focused area over the area of the electrode (α_f) for different voltages and the three particle types shown in Figure 5-6 (SI-5, PS-15, and PS-5).

Particle type	$U = 45V$		$U = 60V$		$U = 75V$		$U = 100V$	
	N_{max}	α_f	N_{max}	α_f	N_{max}	α_f	N_{max}	α_f
SI-5	4	45%	5.9	19.6%	10.8	8%	–	–
PS-15	1.65	63%	–	–	2.15	36.4%	4.5	25%
PS-5	~1	32%	1.15	21%	1.5	4%	–	–

These results are supported by the numerical analysis of the vertical forces on the surface of the electrode (shown in the top row of Figure 5-7). The magnitude of the vertical component of the DEP ($|\boldsymbol{F}_{DEP,v}|$) and gravitational ($|\boldsymbol{F}_g|$) forces are shown by the solid and dashed lines, respectively. The simulation results show that $|\boldsymbol{F}_{DEP,v}|$ at the edge of the electrodes is the same for all electrode sizes ($100nN$); while it decreases toward the center of the electrode. The distribution of $|\boldsymbol{F}_{DEP,v}|$ is such that for the three large electrodes a trapping zone will form (when $|\boldsymbol{F}_{DEP,v}| < |\boldsymbol{F}_g|$); whilst for the $0.4mm$ electrode, $|\boldsymbol{F}_{DEP,v}|$ is always dominant and no trapping region is observed. The simulation results also suggest that the distance between the edge of the electrode, and the trapping region remains constant at $250\mu m$ for $1.5mm$, $1mm$ and $0.6mm$ electrode sizes. However, in these experiments, this distance is larger due to the horizontal component of the DEP force, which respells the particles away from the edge.

As discussed so far, the DGD particle focusing technique concentrates particles inside the droplet over a wide range of the particle density. However, the focusing behavior is limited by the size and density of the particles. When the density is very low (here $\rho = 1.06\ g/m^3$), the diameter has to be large to achieve focusing (here $15\ \mu m$). On the other hand, as shown for SI-5, when the density of particle is high, the focusing behavior improves significantly, and even for small particles (here $5\mu m$) focusing happens efficiently. Focusing can also be improved with increasing the size of the electrode (Figure 5-7). For small and low-density particles, the DGD method can still be used by repelling the particles away from the actuated electrode towards the adjacent electrodes, where they can be collected. This will be demonstrated for $5\mu m$ pathogens with a low density in Chapter 7.

5.5.4 Application

A potential application of the proposed technique is sample concentration on the DMF platform. To show this application, an array of square electrodes is designed with the size of $2\ mm$. The experiment is performed using a $1.5\mu L$ droplet containing the SI-5 particles. Figure 5-8a shows the initial droplet dispensed on the left electrode on the array. A voltage of $U = 75\ V$ and $f = 10\ kHz$ is applied for $60s$ to this electrode and the particles are collected in the center of the electrode. The frequency is then decreased to $f = 1\ kHz$ and by sequential activation of the middle and the right electrodes, the droplet is elongated over the three electrodes (Figure 5-8b). The middle electrode is then deactivated while the two side electrodes are still on, which results in the formation of a neck in the middle of the droplet (Figure 5-8c). The droplet is then split using the left and the right electrodes in the array. Figure 5-8d shows the two daughter droplets, one with a high and the other with a low concentration of the particles. In this particular case, the high concentrated droplet contains around 90% of the particles originally existed in the main droplet. However, upon the application of a slightly higher voltage or a longer duration of the actuation, this concentration will increase over 90%. Splitting the initial droplet without applying DGD will result in an equal number of particles for both of the split droplets (50% of the particles in each droplet).

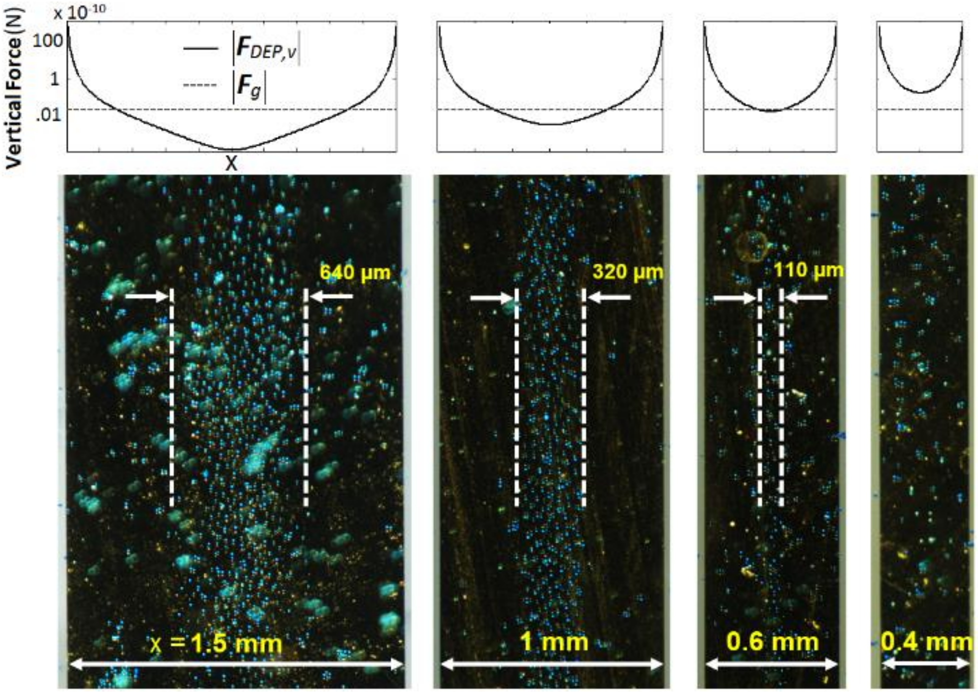

Figure 5-7 Effect of the width of the electrode on focusing behavior of the PS-15 particles. Four widths of $0.4mm, 0.6mm, 1mm$ and $1.5mm$ are used for the electrodes. In each image the width of the electrode is indicated at the bottom of the image. For all cases $U = 75V$ and $h = 320\mu m$. The top row images show the magnitude of the upward vertical component of the DEP force on the electrode surface (solid line) and magnitude of the downward gravitational force (dashed line).

Particle focusing has multiple biological applications, where the particle is a “solid site” used for purification and detection of the target biological molecules [117, 118]. The size of the particles used for these applications ranges from $1 - 15\mu m$ with a density up to $2.5g/cm^3$. Based on the size and the density of these particles, the DGD particle focusing technique presented in this thesis can be used for purification/detection purposes. The advantages of this method would be its high purification efficiency which can be achieved without the need for integrating external modules (e.g. a magnet) to the DMF platform. DGD can also be used on any of the electrodes on the DMF platform which distinguishes this technique from other methods which are dependent on the geometry.

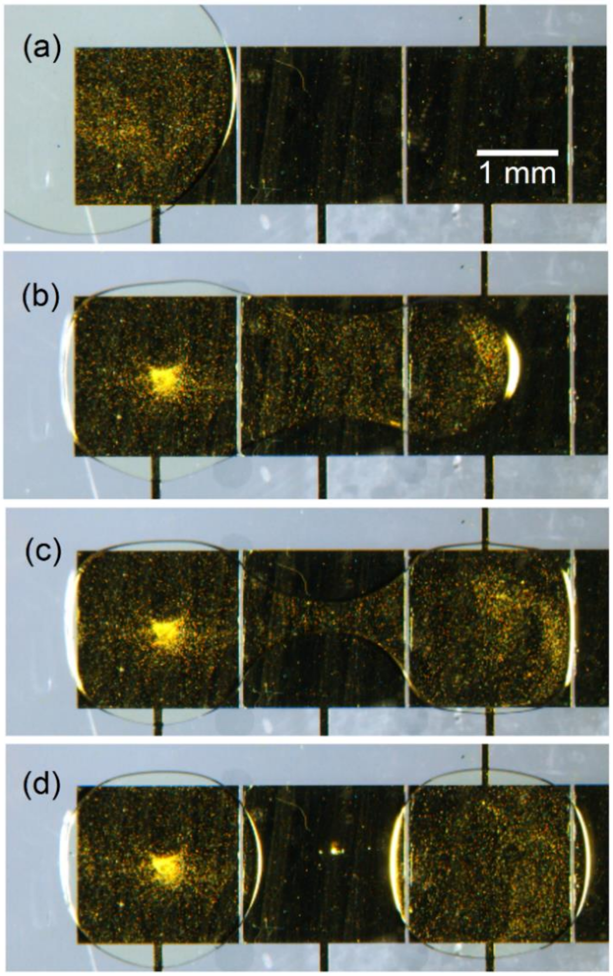

Figure 5-8 Particle concentration using the proposed technique. (a) Initial droplet deposited on the array of electrodes, (b) the collection of the particles on an electrode and elongation of the main droplet on the array of 3 electrodes, (c) Necking of the droplet by actuating the two side electrodes and turning off the middle electrode, and (d) the main droplet split into two daughter droplets, one with a high and the other with a low concentration of the particles.

5.6 Summary

A technique for particle focusing in digital microfluidic (DMF) platforms is introduced based on the combined effects of gravity and negative dielectrophoresis (nDEP). Non-buoyant particles are focused on the center of an electrode actuated with an AC voltage. The gravitational force sediments the particles while the horizontal component of the nDEP force focuses them on the center of the electrode. To efficiently focus the particles, it was shown that the applied voltage must be within a range, below which focusing is not significant and above which the vertical component of the nDEP force repels the particles away from the electrode. The size and the density of the particles were shown to be the key parameters, affecting the focusing behavior significantly. For high density particles, focusing is performed with a very high efficiency while the low density particles are more difficult to concentrate. However, it was shown that the larger the size of the particle the larger the focusing efficiency. Therefore, low density particles could also be focused if they have a relatively large diameter. Even for small and low-density particles, the DGD method can still be used by repelling the particles away from the actuated electrode towards the adjacent electrodes, where they can be collected (see Chapter 7). The size of the electrode was also shown to be important for particle focusing. For a certain gap height and applied voltage, the width of the electrode should be higher than a certain value to be able to concentrate the particles on the center of the electrode.

Chapter 6 Geometrical optimization of hydrophilic surface of biosensors for successful on-chip droplet manipulation[5]

6.1 Overview

DMF has been widely used in biochemical applications due to the recent advances made in applying antifouling techniques to these devices [70]. In general, biochemical applications, found in numerous studies [11, 12, 41], require detection of one or multiple targets in a medium. While in the off-line mode [45], the detection has been performed off the chip, in the on-line mode, which is of particular interest for performing the entire assay on the chip [134, 139] especially for point-of-care applications, the detection is performed on the chip. For the on-line detection methods, the sensing surface of the sensor (functionalized with biological receptors) is in direct contact with the sample. This requires the removal of certain parts of the hydrophobic layer on the DMF device [45, 139, 159]. This consequently limits droplet manipulation. On-chip detection of multiple different analytes has been successfully shown in several studies [45]. However, two main challenges associated with the integration of biosensors into DMF are yet to be addressed: 1) sample removal from the hydrophilic surface of the biosensor; and 2) biochemical regeneration of the biosensor (detaching the target analyte from the receptor) after each round of sensing. While the latter is case dependent and the remedy can vary from one application to another, the solution found for the former problem can be applied to all types of biosensors. In multiple studies in which such detection methods have been adopted, the sensing surface has been kept small enough to enhance droplet transport over the sensing surface [139, 159, 165]. For instance, Yu et al. [165] limited the area of the

---

[5] Parts of this chapter have been published in Biosensors and Bioelectronics (E. Samiei et al, *Biosensors and Bioelectronics*, (2016), 81, 480-486).

sensing surface to 9.6% of the area of the actuating electrodes for successful droplet removal from the sensing zone. However, the performance of the sensor might be hindered by limiting its surface area. Therefore, a systematic study is required to find the optimum geometry for such detection systems on DMF to use the largest possible area for sensing surface.

In this chapter, a thorough study is performed to characterize the hydrophilic surfaces of the biosensors, resulting in finding the optimum configuration of the sensing surface for successful droplet manipulation. The hydrophilic spots (HS) which represent the sensing surface of the biosensors are patterned in a rectangular configuration on the top plate (a possible location for patterning the sensor) and positioned on the top of the array of electrodes on the bottom plate. Three common surface materials in biosensors are selected for HS: gold (Au), silicon dioxide (SiO_2) and Au with immobilized antibodies (Au_m). The main goal is to find the best configuration of HS and the DMF system (resulting in largest size of the sensor) for which droplet transport is performed with the notion of negligible sample residual on HS. As a proof of concept, the optimized geometry found for the HS and the best configuration for the DMF device are used to fabricate a capacitive-based biosensor [223] for detection of *Cryptosporidium*. Two main criteria used for evaluating the success of the biosensor developed are the removal of the sample from the sensing area after detection and the capability of the sensor to detect the target.

6.2 Experimental procedure

In this study, the detection system is integrated on the top plate of the DMF device and positioned on top of the array of electrodes patterned on the bottom plate. A rectangular shape is chosen for the hydrophilic spot (HS), representing the sensing surface of the sensor. The schematic of the device is illustrated in Figure 6-1. To perform a thorough characterization of

HS, the experiments have been performed in three stages. First, the surface properties of different surfaces chosen for HS (i.e., Au, SiO_2 and Au_m) are studied by contact angle measurement using the setup and procedure explained in Section 2.1.2. In the next step, droplet transport on a DMF device is performed over HS areas with different geometrical and surface properties to find the best geometry over which a droplet can be transported with no or a negligible residual volume on HS. Finally, based on the optimum configuration found for HS, a capacitive biosensor is fabricated for the detection of a target (*Cryptosporidium* in this case) on a DMF device such that after the detection process the droplet can be transported away from the biosensor.

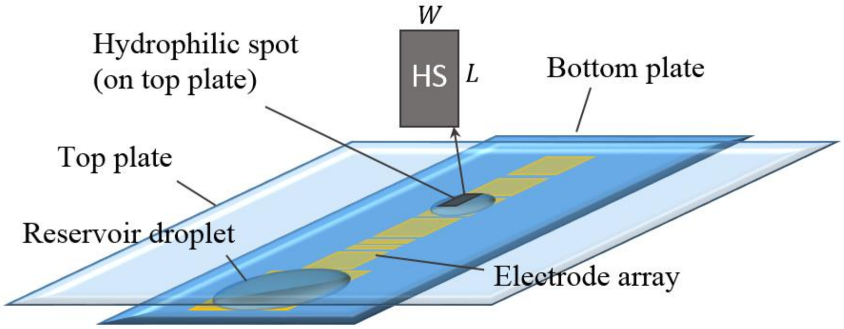

Figure 6-1 Schematic of the DMF setup for droplet transport over a hydrophilic spot (HS), patterned on the top plate and located on the array of electrodes.

Droplet actuation was performed using EWOD. A frequency of $f = 1kHz$ was used for the applied potential. The voltage was generated using a signal generator (Tektronix AFG3021B0) in series with an amplifier (TREK PZD700). The experiments were monitored under a microscope (Leica Z6 APO) and recorded using a high speed camera (2592×1944 resolution). For all experiments, the threshold voltage (U_{th}) required for removing the droplet from the hydrophilic spot (HS) was applied. In fact, U_{th} is used to compare the results obtained for different sets of experiments. The duration of the applied voltage varies between $1-3s$ for different cases.

6.2.1 Experiments on hydrophilic spot (HS)

The hydrophilic spot (HS) is patterned in a rectangular shape with different aspect ratios ($\gamma = 0.4, 0.667, 1, 1.5$ and 2.5) where the aspect ratio is defined as $\gamma = L/W$ (length/width of HS, Figure 6-1). A dimensionless surface area (A_{HS}^{*}) for HS is defined as the ratio of the area of HS (A_{HS}) to that of the actuating electrodes (A_d). Several values of A_{HS}^{*} are considered as $A_{HS}^{*} = 0.089, 0.133, 0.178$ and 0.222 which represent 8.9%, 13.3%, 17.8% and 22.2% of the area of the actuating electrodes, respectively. For the DMF system, square electrodes with two different dimensions of $L_d = 1.5$ and $2mm$ and the gap heights (between the top and bottom plates) of $h = 150,\ 220$ and $280\ \mu m$ were chosen, while the normalized gap height is defined as $h^{*} = h/L_d$. Also, the sensitivity of the results to the volume of the droplet is studied with three different volumes of the droplet. To generate variable, but accurate, volumes of droplets, two of the electrodes are patterned with a smaller width (0.185 mm) (Figure 6-2) and droplet dispensing from the reservoir electrode is performed by actuating different combinations of a normal electrode and the two thinner electrodes (similar to the method presented in Chapter 3). Two possible locations are studied for HS: 1) the HS on the top plate is aligned on the middle part of the bottom electrode (referred to as M in Figure 6-2), and 2) the HS is aligned with the edge of the bottom electrode (referred to as E).

6.2.2 Detection

As the last stage, the droplet transport is performed over a biosensor integrated into the DMF platform for the detection of *Cryptosporidium.* This part is conducted to show the use of the optimum configuration for the sensing surface found in this study.

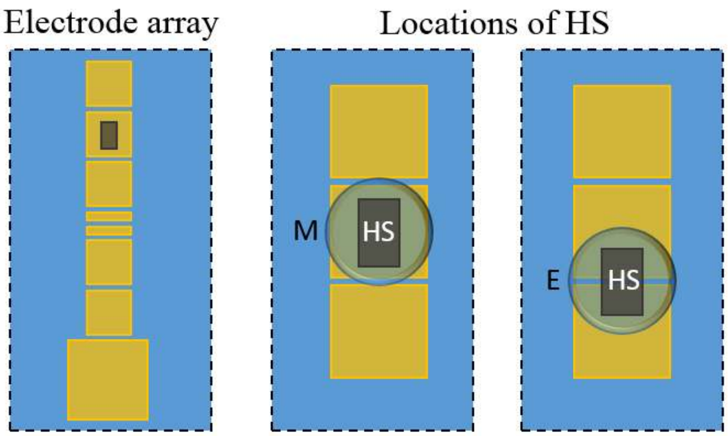

Figure 6-2 Configuration of the array of electrodes for droplet manipulation and the two considered locations for the HS (aligned with the middle (M) and the edge (E) of the bottom electrode).

A capacitive biosensor is patterned on the top plate (Figure 6-3), which is formed of two interdigitated electrodes (IDE) made of gold (Figure 6-3) with the immobilized antibodies specific to *Cryptosporidium*. A window of the cytop layer is removed from the IDE surface to expose the biosensor to the target (see the details in Section 2.2.6). The capacitive measurement is performed using a network analyzer (N5241A, Agilent Technologies) in the frequency range of 4 GHz to 7 GHz. After detection, the droplet is moved away from the sensing zone to show the feasibility of the study presented here.

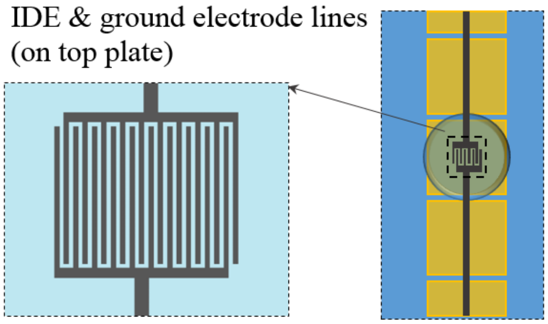

Figure 6-3 Schematic of the interdigitated electrodes (IDE) and the ground electrode located over the array of electrodes. The configuration of IDE is shown in the inset of the image.

6.3 Device fabrication

The bottom plate contains the actuating electrodes for droplet manipulation, and the top plate contains the ground electrode. The hydrophilic spot (HS) under study is patterned on the top plate by partially removing the hydrophobic layer and depositing the desired material. The sensing system is patterned on the top plate and placed over the array of actuating electrodes.

6.3.1 Bottom plate- actuating electrodes

The array of electrodes includes a reservoir electrode, followed by two regular (square) electrodes, two thin electrodes, and five regular electrodes (schematically shown in Figure 6-1 and Figure 6-2). The regular electrode along with the two adjacent thin electrodes is used for accurately dispensing droplets (from the reservoir) with different sizes. The substrate is a glass slide covered with $50\ nm$ of Cr and $100\ nm$ of Au sputtered (Angstrom Engineering) on the surface. Standard photolithography is used to pattern the electrodes on the substrate (see Section 2.2.3). Parylene C was then deposited on the substrate as the insulating layer with a thickness of $7\ \mu m$ (using SCS Labcoter® 2 (PDS 2010)). To form the hydrophobic layer, a 3% solution of cytop (PFC 1603V, Cytonix Co.) was spun on the substrate and post baked at $150\ °C$ for $30\ min$.

6.3.2 Top plate-hydrophilic patterns

The top plate used for the hydrophilic experiments is an ITO-coated glass slide (SiO_2 passivated, $R_s = 4–8\ \Omega$, Delta Technologies, LTD) which is coated with a hydrophobic layer of cytop (as explained in the previous section) and post baked at $200^\circ\ C$ for $1\ hr$. The rectangular hydrophilic spot (HS) is patterned on the ITO slide (Figure 6-2) by removing the cytop and replacing it with the three different hydrophilic materials (Au, SiO_2 and Au_m).

Following the procedure explained in Section 2.2.6, the cytop coated ITO slide was first removed and then the hydrophilic material (Au or SiO_2) is sputtered on the slide. For the case of Au_m, antibodies specific to *Cryptosporidium* are immobilized on the Au part of the slide using the method explained in the next section.

6.3.3 Top plate - capacitive biosensor

For the biosensing part of the experiments, a top plate covered with layers of Cr and Au is used. The interdigitated electrode (IDE) capacitive biosensor is patterned on the slide using standard photolithography. The biosensor includes two IDEs (Figure 6-3), each of which contains 10 fingers with the length of $640\mu m$ and the width of $20\mu m$. The distance between each pair of fingers is $20\mu m$. The substrate is then coated with cytop. A rectangular part of the cytop is removed from IDE using oxygen-plasma (explained in the previous section) to expose the IDE area to the target. The size of the rectangular area is determined based on the results of the HS experiments ($0.76mm \times 0.76mm$).

The immobilization of anti-*Cryptosporidium* antibodies on the gold surface of the interdigitated electrodes (IDE) was carried out following the steps explained in Section 2.2.7.

6.4 Results and discussion

The objective of this chapter is to experimentally characterize the hydrophilic surface of the sensors on DMF platforms such that droplet manipulation is performed over the sensing surface with no or a negligible amount of liquid residing on the surface. Initially, the surface properties of the sensors (HS) will be studied with three surfaces: Au, SiO_2, and Au_m. Then the geometry of HS will be studied for different configurations of the DMF platform. Finally, based on the optimum geometry, an interdigitated electrode (IDE) capacitive biosensor is integrated to the DMF platform for detection of a sample target (*Cryptosporidium*) as a proof of concept.

6.4.1 Surface characterization of hydrophilic spot (HS)

The ability to remove the droplets from the surface of the biosensors on DMF systems depends on the surface properties (wettability) of the biosensing region. Most sensors (e.g., electrochemical and optical) integrated into DMF devices are patterned on a substrate of either glass substrates or a silicon wafer with an oxide layer grown on the surface, and include metal electrodes such as gold. Other plastic-based surfaces are also frequently used, though such materials are significantly less hydrophilic, and hence, less limiting than glass and SiO_2 for droplet manipulation. Therefore, Au and SiO_2 are the most appropriate choices for the hydrophilic spot (HS) in this study. However, the biological sensors are always functionalized using the bio-receptors (e.g., antibodies), specific to a certain type of the target analyte. To consider this, a gold surface with immobilized antibodies (Au_m) is also characterized. Using the experimental setup shown in Figure 2-2 and the procedure explained in Section 2.1.2, the advancing, receding, the change in the receding and the difference between the advancing and receding contact angles (θ_{adv}, θ_{rec}, $\Delta\theta_{rec}$ and θ_{hys}, respectively) are measured for the three surfaces under study. The results are presented in Table 6-1.

Table 6-1 Results of the contact angle measurement for the three surfaces of Au (gold), SiO_2 (silicon dioxide) and Au_m (gold with immobilized antibodies).

Surface	**Au**	**Au_m**	**SiO_2**
$\boldsymbol{\theta_{adv}}(°)$	90	56.48	21.98
$\boldsymbol{\theta_{rec}}(°)$	45.94	3.82	4.22
$\boldsymbol{\Delta\theta_{rec}}(°)$	1.04	10.57	4.64
$\boldsymbol{\theta_{hys}}(°)$	44.06	52.66	17.76

The advancing contact angle for Au, SiO_2 and Au_m are $\theta_{adv} = 90°$, $21.8°$ and $56.48°$, respectively. This suggests that the SiO_2 surface has a high degree of wettability. The comparison between θ_{adv} for Au and Au_m shows that the presence of the antibodies significantly decreases the advancing contact angle which is the result of the change in the surface morphology and wettability caused by the immobilization of antibodies. On the other hand, the comparison between the receding contact angles shows that Au_m and SiO_2 surfaces are superhydrophilic due to their very low receding contact angles ($\theta_{rec} = 3.82°$ and $4.22°$ for Au_m and SiO_2, respectively) while Au surface is relatively hydrophilic. The change in the receding contact angle and the contact angle hysteresis for SiO_2 surface ($\Delta\theta_{rec} = 4.64°$ and $\theta_{hys} = 17.76°$) show that the sputtered SiO_2 has a relatively smooth surface, while the other two surfaces have a rough morphology. Especially, Au_m surface has a large hysteresis ($\theta_{hys} = 52.66°$) which is due to the presence of the antibodies and the rough morphology of the surface. These results suggest that Au_m and SiO_2 surfaces can be considered as the most extreme cases due to their superhydrophilic behavior (extremely low θ_{rec}).

6.4.2 Geometrical optimization of hydrophilic spot (HS)

The geometry of the hydrophilic spot (HS) representing the biosensing area was studied in terms of different geometrical parameters. The parameters studied are the aspect ratio (for the rectangular shape considered here), the surface area and material for HS, and the electrode size and the gap height for the DMF platform.

6.4.2.1 Effect of size and aspect ratio of HS

In the first part, the aspect ratio (γ) and the normalized area (A_{HS}^{*}) of HS are studied. For this purpose, the electrode size of $L_d = 2mm$ and the gap height of $h = 220\mu m$ ($h^{*} = 0.11$) were considered for the DMF platform. Also, a conventional electrode (one electrode after the reservoir shown in Figure 6-2) was used to dispense the droplet of a volume of $V_d = 0.88\mu L$ for all experiments. The results illustrated in Figure 6-4 show the threshold voltage (U_{th}) versus the aspect ratio of HS (γ). The first conclusion drawn from the results is that U_{th} increases as the size of HS increases. Since wettability of the surface is a limiting factor for droplet motion, a large applied voltage is hence required for transport of a droplet over a larger HS area. For the case of the Au surface, we found that even for the largest HS area ($A^*_{HS} = 0.222$) tested here the droplet can be removed from the surface without reaching the maximum possible voltage.

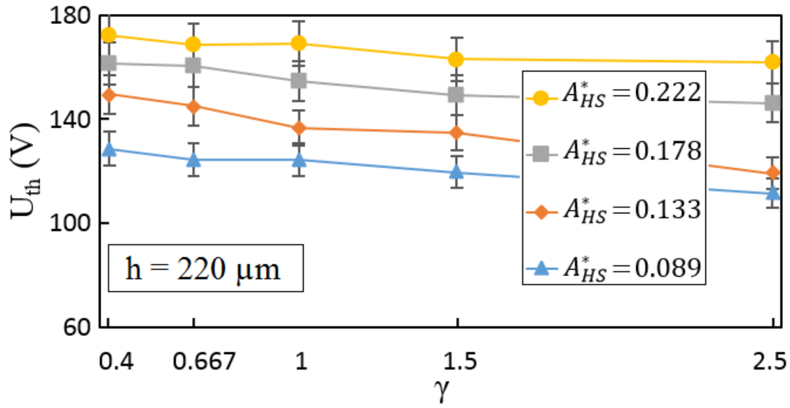

Figure 6-4 Results of the experiments conducted for geometrical optimization of the hydrophilic spot (HS). All the results were obtained for a platform containing a $2mm$-electrode array. The gap height is $h = 220\mu m$ ($h^* = 0.11$) and the Au HS normalized areas are $A^*_{HS} = 0.089, 0.133, 0.178$ and 0.222.

The effect of the HS aspect ratio (γ) can be observed in Figure 6-4. For a certain size of HS, U_{th} is descending with respect to γ. This behavior is observed for all four HS sizes ($A^*_{HS} = 0.089, 0.133, 0.178$ and 0.222). The effect of the aspect ratio on droplet removal can also be observed from the experimental images shown in Figure 6-5. In essence, the EWOD force from the bottom-plate electrode is driving (pulling) the droplet; while HS on the top plate causes resistance in the motion of the droplet (especially around the three-phase contact line). The smaller the width of the HS (i.e., the larger γ) the smaller the resistance and consequently the smaller the value of U_{th} (as observed in Figure 6-4). Therefore, the width of HS has a dominant effect on the required voltage.

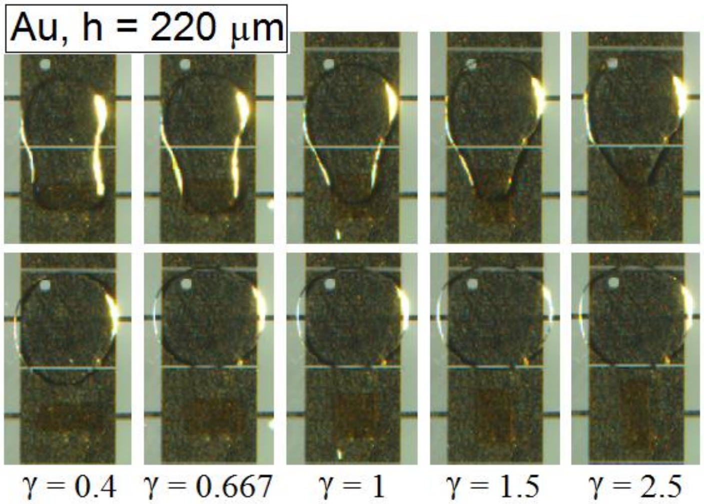

Figure 6-5 Experimental images of the HS areas tested with the electrode size of $L_d = 2mm$. The top row images show the moments that the droplet is on the HS and the adjacent electrode is activated to pull away the droplet, and the bottom row images show the moment right after the droplet is pulled away. The gap height is $h = 220\mu m$ ($h^* = 0.11$) and the Au HS size is $A_{HS}^* = 0.222$.

6.4.2.2 Effect of gap height

To study the effect of the gap height, all the experiments were repeated for the gap height of $h = 150\mu m$ ($h^* = 0.075$) and the results are shown in Figure 6-6. Using a similar method of droplet dispensing, the surface area (observed in the top view) of the droplet was kept similar to that obtained for the case of the gap height of $h = 220\mu m$ ($h^* = 0.11$). The overall trend of the curves is similar to that observed for the case of $h^* = 0.11$ (U_{th} is descending with respect to γ) except for the fact that the required applied voltage is smaller ($10-20\%$ smaller than U_{th} for $h^* = 0.11$). However, it has to be mentioned that decreasing the gap height does not necessarily enhance droplet removal from HS since interfacial stability of the droplet deteriorates as the gap height is decreased. This will be discussed in detail later (see Section 6.4.2.4).

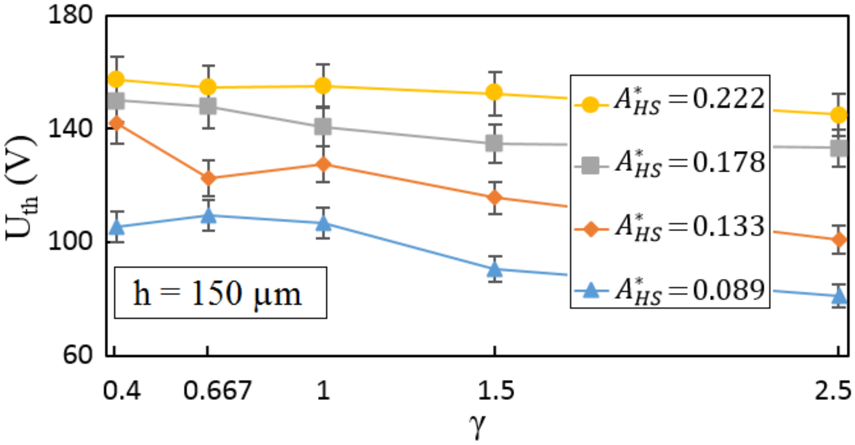

Figure 6-6 Results of the experiments conducted for geometrical optimization of the hydrophilic spot (HS). The results were obtained for a platform containing a $2mm$-electrode array. The gap height is $h = 150\mu m$ ($h^* = 0.075$) and the Au HS normalized areas are $A^*_{HS} = 0.089, 0.133, 0.178$ and 0.222.

6.4.2.3 Effect of electrode size

The effect of the electrode size on the droplet removal has also been taken into account by comparing the results for two electrode sizes of $L_d = 1.5mm$ and $L_d = 2mm$. For this comparison the gap height is set to $h = 150\mu m$ and only the largest HS size is considered ($A^*_{HS} = 0.222$). As it is shown in Figure 6-7, the case with the smaller electrode requires smaller U_{th} ($\sim 20\%$ lower voltage) for droplet removal from HS. This suggests that a smaller size of the electrode array has a better performance for droplet removal. However, it has to be noted that A^*_{HS} is the ratio of the HS surface area to that of the actuating electrode, and hence for a similar A_{HS}^{*} (for both electrode sizes), the HS size is smaller for the smaller electrode length (i.e., $L_d = 1.5mm$). This may not be desirable as the size of the biosensor is in fact independent of the DMF platform. In other words, fabrication of a certain type of the sensor with a desired sensitivity requires a specific surface area which is independent of the size of the DMF actuating electrodes. Therefore, using a smaller electrode array might limit the area available for sensor fabrication.

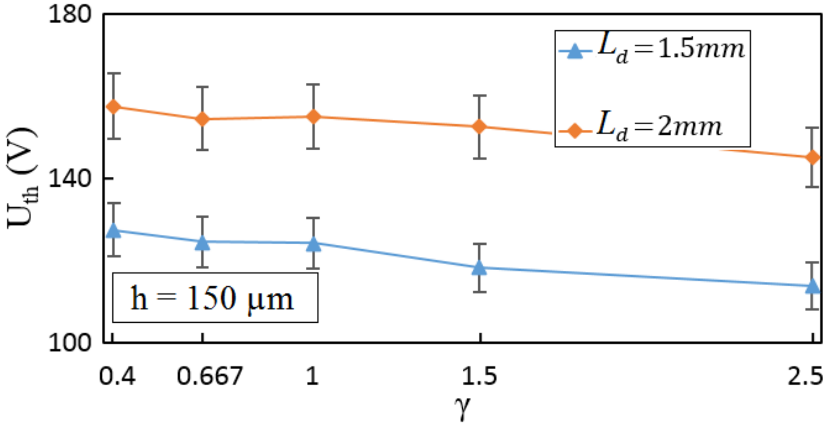

Figure 6-7 Results of the experiments conducted for geometrical optimization of the hydrophilic spot (HS). The graph shows the comparison between the $1.5mm$ and $2mm$ electrodes with the Au surface, $h = 150\mu m$ and $A_{HS}^{*} = 0.222$.

6.4.2.4 Effect of surface properties of HS

The electrode size of $L_d = 2mm$ was chosen for this part since it provided a larger area of HS. Initially, two gap heights of $h = 150\mu m$ and $220\mu m$ ($h^{*} = 0.075$ and 0.11, respectively) were used for this study. Figure 6-8 and Figure 6-9 show the droplet images for the experiments performed with the Au$_m$ surface with the HS size of $A_{HS}^{*} = 0.089$ for the two gap heights. As it can be observed in Figure 6-8 representing the results for $h^{*} = 0.075$, the droplet splits on the HS surface (for all cases of γ) upon pulling motion.

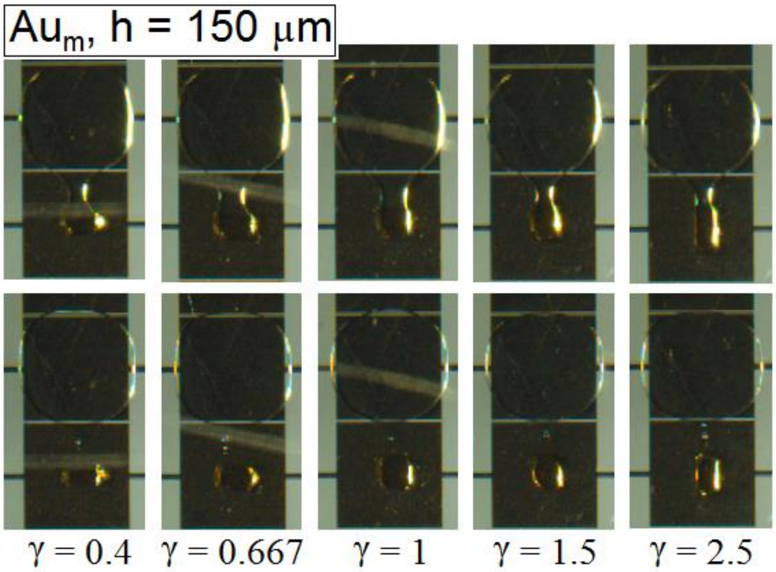

Figure 6-8 Experimental images of the HS areas tested for Au$_m$ for the gap height of $h = 150\mu m$ ($h^* = 0.075$) and the electrode size of $L_d = 2mm$. The top row images show the moments that the droplet is on the HS and the adjacent electrode is activated to pull away the droplet, and the bottom row images show the moment right after the droplet is pulled away. The Au$_m$ HS size is $A_{HS}^* = 0.089$.

This is due to the fact that for the lower gap heights the droplet is less stable, and since the Au$_m$ HS is superhydrophilic, the droplet will split. By increasing the gap height to $h^* = 0.11$, on the other hand, the droplet can be pulled away from the HS surface without splitting (see Figure 6-9). However, a very small volume of liquid (in the range of $< 500pL$) remains on the HS surface (only on the top plate) with a volume less than 0.1% of the original droplet volume. This small size of the liquid can readily be removed by transporting one or two washing droplets over HS. Therefore, for successful removal of the sample droplets from the hydrophilic sensing surfaces on DMF, the gap height should be kept large enough to prevent droplet splitting. However, it has to be considered that for very large gap heights droplet dispensing from the reservoir will be hindered or produce large deviations in the droplet volumes, affecting the reliability of bioassays performed on the chip. Therefore, the choice of the gap height is very crucial to satisfy these two problems.

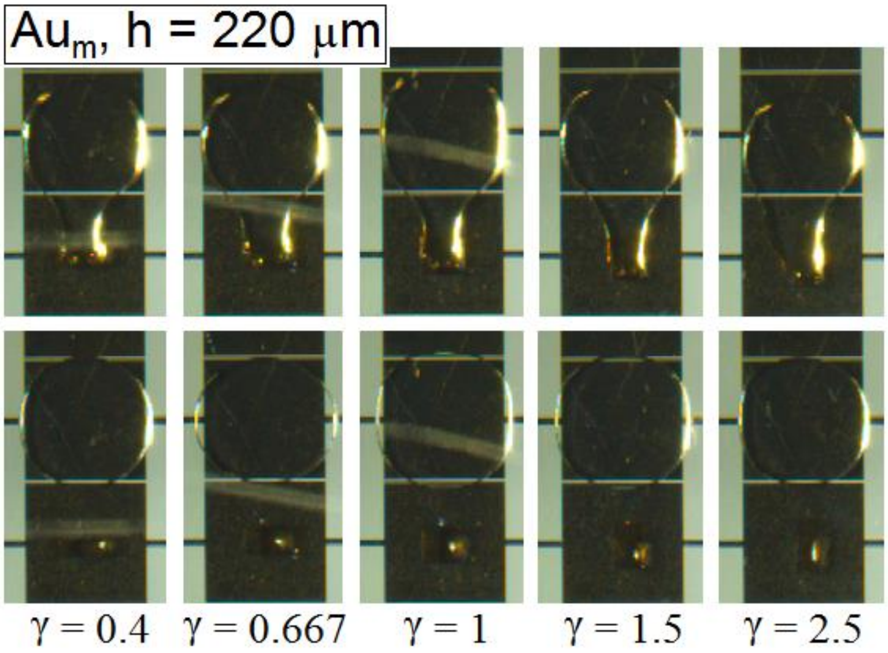

Figure 6-9 Experimental images of the HS areas tested for Au_m for the gap height of $h = 220\mu m$ ($h^* = 0.11$) with the electrode size of $L_d = 2mm$. The top row images show the moments that the droplet is on the HS and the adjacent electrode is activated to pull away the droplet, and the bottom row images show the moment right after the droplet is pulled away. The Au_m HS size is $A_{HS}^* = 0.089$.

Based on the above discussion, the gap height was set to $h^* = 0.11$ for the experiments with HS of Au_m and SiO_2 (superhydrophilic). Droplet removal was successful only for $A_{HS}^* = 0.089$ and it failed for $A_{HS}^* = 0.133, 0.178$ and 0.222. The results for the successful case of $A_{HS}^* = 0.089$ and $h^* = 0.11$ are shown in Figure 6-10 for the three surfaces of Au, SiO_2 and Au_m. It can be observed that the threshold voltage is relatively low for the Au surface ($111 - 129V_{rms}$

for all values of γ) while it is $40 - 60\%$ larger for Au$_m$ and SiO$_2$. In addition, it can be observed that for the two superhydrophilic cases (Au$_m$ and SiO$_2$), the threshold voltage (U_{th}) is very similar. This is due to the fact that the receding contact angles for these two surfaces are very close ($\theta_{rec} = 3.82°$ and $4.22°$ for Au$_m$ and SiO$_2$ surfaces, respectively). To achieve successful droplet removal from a larger HS the gap height was increased to $h = 280\mu m$ ($h^* = 0.14$) and the experiments were performed for both Au$_m$ and SiO$_2$ surfaces successfully with the HS sizes of $A_{HS}^* = 0.089$ and 0.133. This shows that it is possible to transport a droplet over an HS area as big as 13.3% of the size of the actuating electrodes, while the gap height is within an acceptable range for droplet splitting on the actuating electrode of $L_d = 2mm$.

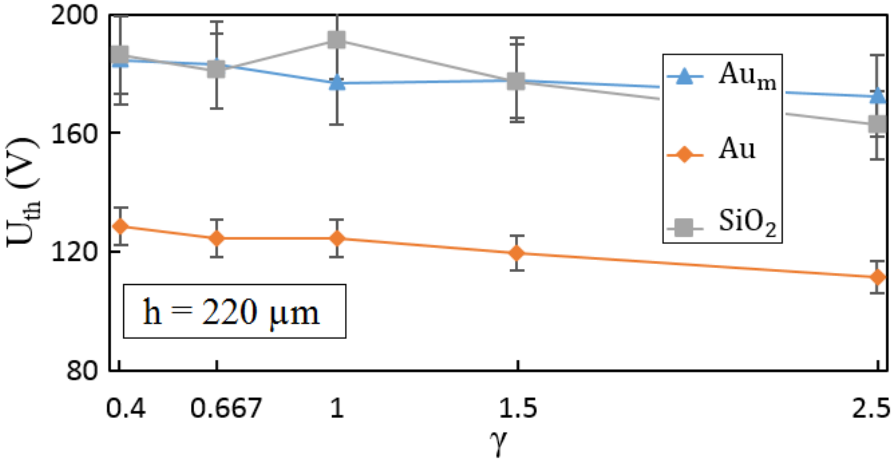

Figure 6-10 Results of the experiments conducted for geometrical optimization of the hydrophilic spot (HS). All the results were obtained for a platform containing a $2mm$-electrode array. The graph shows the comparison of the three surfaces of Au, Au$_m$ and SiO$_2$ with $h = 220\mu m$ ($h^* = 0.11$) and $A_{HS}^* = 0.089$.

For a DMF system with the electrode size of $L_d = 2mm$, this will result in an HS area of $0.73mm \times 0.73mm$, which is large enough for the fabrication of most types of biosensors including interdigitated electrode (IDE) capacitive, surface plasmon resonance (SPR), and amperometric biosensors.

6.4.2.5 Effect of droplet volume

To study the sensitivity of the results to the volume of the droplet, a set of experiments was performed with three different volumes of the droplet. For these experiments, the electrode length of $L_d = 2mm$, the gap height of $h^* = 0.075$, and the HS surface made of Au with the aspect ratio of $\gamma = 1$ (square HS) and the normalized HS surface area of $A_{HS}^* = 0.222$ were used. Three different combinations of the electrodes were used to generate droplets with different volumes using the configuration shown in Figure 6-2.: 1) a square-shaped electrode ($V_1 = 0.71\mu L$), 2) a combination of a square-shaped electrode and a thin electrode ($V_2 = 0.85\mu L$), and 3) a square-shaped electrode and two thin electrodes ($V_3 = 0.98\mu L$). The droplets generated using this method are shown in Figure 6-11. The droplets were transported to HS and then removed from it using threshold voltages of $U_{th} = 154.8, 155.26$ and $155.9V$, respectively. The differences between these three voltages are less than 1% which can be assumed negligible for the droplet volume changes of almost 40%.

6.4.2.6 Effect of HS position with respect to bottom-plate electrodes

The effect of the location of the hydrophilic spot (HS) with respect to the bottom-plate electrode was also studied. For this purpose, two locations of the HS were considered as M (middle) and E (edge). Droplet removal was performed using these two locations and the experimental images are shown in Figure 6-12. The threshold voltage required to remove the droplet was $U_{th} = 150.18$ and $134.76V$ for the M and E locations, respectively.

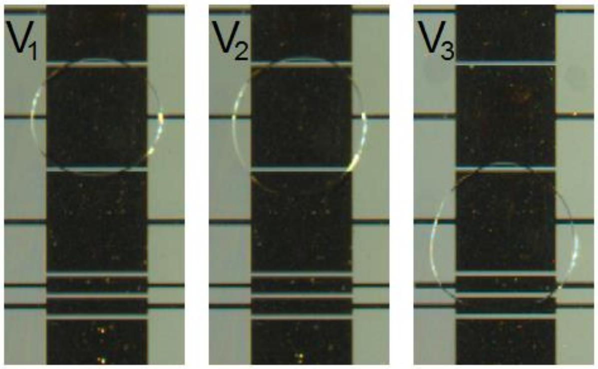

Figure 6-11 Droplets with three different volumes generated using 1) a square-shaped electrode ($V_1 = 0.71\mu L$), 2) a combination of a square-shaped electrode and a thin electrode ($V_2 = 0.85\mu L$), and 3) a combination of a square-shaped electrode and two thin electrodes ($V_3 = 0.98\mu L$).

The smaller voltage for the E location suggests that this location is easier for droplet removal compared to the M location. However, due to a much longer neck formed in the case of the E location (see the left image in Figure 6-12), there is a high possibility of droplet splitting over HS. For the Au surface used for these experiments droplet splitting happened for 20% of the attempts, while for the M location all the attempts were successful and the droplet was completely removed from HS. The splitting issue for the E location will even be more probable for surfaces with higher levels of wettability (such as Au_m and SiO_2). Therefore, the M location is more reliable for placing HS.

6.4.3 Capacitive biosensor for detection of *Cryptosporidium*

Manipulation of a droplet over a hydrophilic spot (HS) was studied thoroughly in the previous parts of this chapter and the effects of multiple parameters including the type and the geometry of HS and the DMF system on the limits of droplet transport were discussed. Considering the optimum dimensions found for HS and the corresponding configuration for the DMF system, a biosensor is fabricated and integrated into DMF to examine the feasibility of performing on-chip sample sensing and removal of the sample from the sensing surface afterwards.

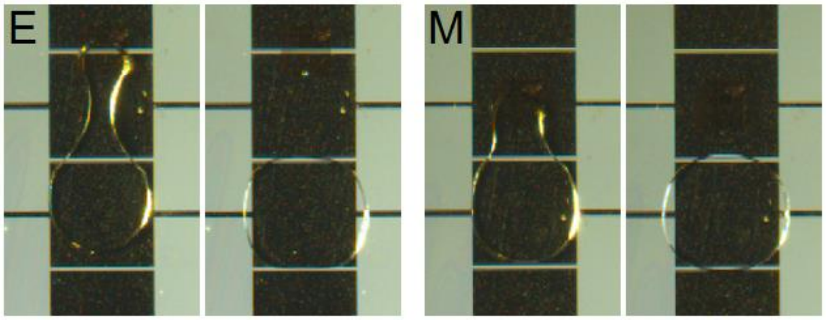

Figure 6-12 Experimental images for two locations of the HS: 1) the HS was aligned with the middle of the actuating electrode on the bottom plate (referred to as the M location), and 2) the HS was aligned with the edge of the actuating electrode on the bottom plate (referred to as the E location). In each of these images (labeled as E and M), the left image shows the droplet before removal and the right image shows the droplet after removal from the HS area.

For the proof of concept, detection of *Cryptosporidium* is performed with an interdigitated electrode (IDE) capacitive biosensor with the geometry shown in Figure 6-13a. Detection of *Cryptosporidium* is chosen for this test because the protein compounds used for the linker along with the immobilized antibodies and incubated cells provide the highest level of wettability which can be considered as an extreme case for droplet removal. The gap height for the DMF device is set to $h = 280\mu m$ ($h^* = 0.14$) and the electrode array with the size of $L_d = 2mm$ is used for the experiment. As explained earlier, the top plate is a glass slide containing the IDE sensor. The top plate is covered with a hydrophobic layer facilitating droplet manipulation. To expose the sensing part (the IDE area), a square window with the size of $0.73mm \times 0.73mm$ (the largest size compatible with $h^* = 0.14$ and the Au_m surface) was removed from the hydrophobic layer. The connection lines of IDE are used as the ground electrode for droplet transport to the sensing zone (IDE). After transporting the droplet to the sensing zone, the connection lines are detached from the signal generator (used for droplet manipulation) and then connected to the network analyzer for sensing.

Capacitive sensing was conducted for a sample of DI water on the IDE in the DMF setup shown in Figure 6-13a. Measurements were performed first for the IDE with immobilized anti-*Cryptosporidium* antibodies (C_0) and then with the IDE incubated with *Cryptosporidium* (C). For each case, the capacitance was measured after delivering a droplet of DI water to the IDE area. Figure 6-13b shows the difference between the capacitance of the IDE with and without the cells, normalized with the capacitance without the cells ($\Delta C/C_0 \times 100\ (\%)$), for five different concentrations of *Cryptosporidium* in a range between $15\ \text{cell}/\mu L$ to $240\ \text{cell}/\mu L$ (C15 to C240). The measurements were carried out for eight replications of each concentration and the average values and the standard deviations from the average were calculated. Since the bound between the antibodies and *Cryptosporidium* is irreversible from the regeneration perspective, each data point was obtained using a different device. The results in Figure 6-13b show that for the chosen range of frequency the difference in capacitance increases as the frequency is increased. Also, the measured signal increases as the concentration of the sample increases. The calibration curve is provided in Figure 6-13c. Based on this graph, the change in the signal by increasing the number of cells is larger for lower concentrations, while the slope of the curve becomes smaller for higher concentrations.

For all measurements, the water droplet was transported to the sensing zone (IDE) and after the measurement the droplet was successfully transported away from IDE (Figure 6-13a). This illustrates feasibility of droplet removal from the hydrophilic biosensing surfaces in DMF systems.

6.4.4 Recommendations

The transport of droplets over hydrophilic spots (HS) was performed for different surface properties and geometry of the HS and DMF platform. It was shown that certain strategies have to be considered for designing the geometry of the sensing surface of the biosensors and setting the parameters of the DMF platform to achieve the largest possible size of the surface for successful droplet removal after biosensing. Based on the results shown in this study, it is recommended to design the sensing surface with a high aspect ratio and align it with the center of the actuating electrode. In fact, the distance between the edge of the sensing surface and the edge of the following actuating electrode should be kept less than half of the length of the electrode to avoid excessive elongation and breakup of the droplet. The gap height for the DMF system is another important parameter. To avoid droplet breakup, it is recommended to keep the gap close to the upper limit of the range required for precise droplet manipulation.

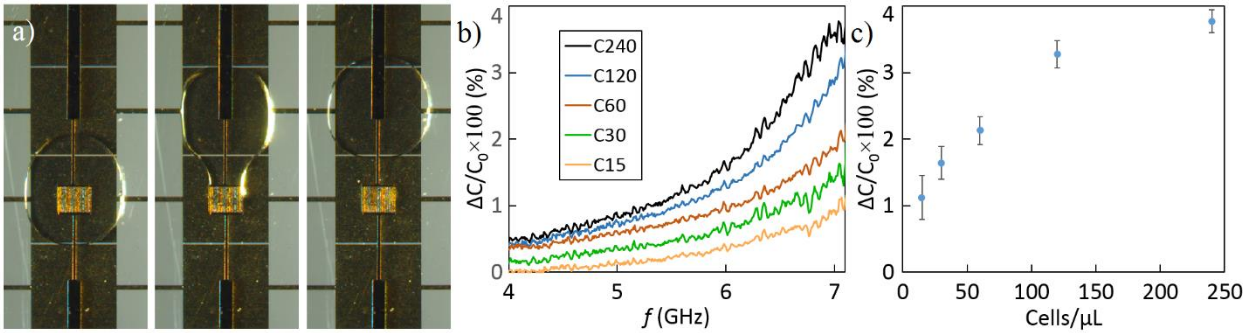

Figure 6-13 Results of the capacitance measurement for detection of *Cryptosporidium*. The measurements are performed with water as the medium and the frequency range of $f = 4GHs$ to $7GHz$. a) A Sequence of images showing detection and droplet removal from the IDE biosensor located on the top plate is illustrated. b) Capacitive measurements for the samples with different concentrations of cells, ranging from 15 cell/μL to 240 cell/μL. ΔC presents the difference between the measured capacitance of the IDE incubated with the solutions of cells (C) and the IDE with immobilized antibodies (C_0). c) The calibration curve for the results is presented for 8 replications conducted for each concentration. The error bars present the standard deviation of the results from the average value.

6.5 Summary

To apply the digital microfluidic (DMF) systems to practical biochemical applications and utilize them in assays requiring the detection of target analytes, one main concern is the ability to restore the sensing surface. This requires that the sample droplet be removed and the sensing surface on the chip be completely cleared with negligible or preferably no residual volume left behind. In practice, this concern has limited the use of DMF systems as a complete micro-total analysis system since liquid manipulation requires hydrophobic surfaces whereas the sensing surfaces of biochemical sensors typically demand hydrophilic surfaces. In this chapter, a systematic study was conducted to find the optimal geometry for a hydrophilic spot (HS), representing the sensing surface of a sensor, and the overall configuration of the DMF platform using which it is possible to remove the droplets from HS. A rectangular geometry is considered for HS with the aspect ratio (γ =length/width) ranging between $0.4 < \gamma < 2.5$. Three different surface materials of gold (Au), silicon dioxide (SiO_2) and gold with immobilized antibodies (Au_m) were tested. The effects of the electrode size and the gap height between the two plates of the DMF system were also studied. The dominant parameters were found to be the aspect ratio of HS, the gap height in the DMF platform, and the location of HS with respect to the actuating electrodes in DMF. Results revealed that the higher the aspect ratio of the HS the lower the threshold voltage (U_{th}). It was also found that a decrease in the width of HS reduces U_{th}. The study of the gap height between the two plates (h) showed that reducing h decrease U_{th}. However, lowering h also decreases the stability of the droplet, increasing the chance of splitting over HS. Therefore, h has to be kept within a certain range (depending on the device properties, here $h^* = h/L_d = 0.14$ where L_d is the electrode size) to enhance droplet removal, and also perform droplet generation with an acceptable precision.

Also, two different locations tested for HS showed that aligning HS with the middle part of the actuating electrode on the bottom plate is the best location. The sensitivity of the results to the volume of the droplet was found to be very insignificant. For the setup used in this study, the optimal configuration for HS and the DMF device found to be a surface area as large as 13.3% of the area of the actuating electrodes for a superhydrophilic (Au_m and SiO_2) and over 22.2% for a hydrophilic surface (Au).

Finally, the best configuration found in the study for the hydrophilic spot (HS) was used for the fabrication of a capacitive biosensor for the detection of *Cryptosporidium*. Detection of different concentrations of *Cryptosporidium* was carried out with successful droplet removal from the surface of the sensor.

Chapter 7 Integration of developed techniques for biosensing in digital microfluidics

7.1 Overview

Throughout Chapters 3 to 6, multiple techniques and strategies were developed to enhance sample preparation, on-chip biosensing, and sample removal after performing biosensing on digital microfluidics (DMF) platforms. This includes the development of i) an unequal splitting method for accurate splitting/dispensing variable volumes of samples on the chip, ii) an electrohydrodynamic technique for rapid mixing in stationary droplets on open and closed DMF platforms, iii) a dielectrophoretic-gravity driven (DGD) method for concentrating and focusing microbeads and cells inside the sample droplets, and iv) surface characterization and geometrical optimization of the hydrophilic surface of biosensors for complete sample removal after sensing. Each Chapter has focused on one of the techniques for which a thorough characterization was performed including sample applications. In order to illustrate the range of applicability of the developed methods, in this chapter a biosensing assay is developed for the detection of *Cryptosporidium* on a DMF platform in which the aforementioned methods have been integrated to perform the entire assay from sample preparation to post detection sample removal. Water samples may contain a low number of *Cryptosporidium* oocysts, where the sample is primarily filtered to increase its concentrate [224]. Following that process, the present platform can be used for selective and sensitive detection of the oocysts. The size and density of *Cryptosporidium* is in the range of the microbeads studied in this thesis for the development of the techniques for mixing and pre-concentration.

More specifically, the developed techniques within this thesis are used as follows: 1) the samples dispensing is performed using the strategies found in Chapter 3 to achieve over 99%

accuracy in the sample volume. As per requirement of the assay, only conventional electrodes were used rather than the geometrically modified operator for variable volume droplet dispensing. 2) To avoid the settlement of the cells and non-uniformity of them in the reservoir droplets, every time before droplet dispensing, the reservoir sample is mixed using the electrohydrodynamic mixing technique. This way the effect of non-uniformity of the initial sample on the results is eliminated. 3) The incubation of cells with the biosensor is performed for two cases: In the first case, incubation is performed using a droplet of the sample with the initial concentration of *Cryptosporidium*. In the second case, using DGD method the cells inside a larger dispensed droplet are concentrated to one side, followed by splitting which results in a high concentration of cells in one of the droplets. Then, the concentrated droplet is used for incubation to increase the number of the captured cells. 4) A biosensor is designed using the results shown in Chapter 6 to avoid the residue of samples on the biosensor after each droplet removal. The removal is critical during the steps involving cell incubation, washing steps, and post sensing. Detection is performed using a capacitive biosensor fabricated on the top plate of the DMF device which also includes the ground electrodes for droplet manipulation.

7.2 Experimental procedure

The detection assay is performed using the DMF chip design shown on Figure 7-1. Reservoir 1 is used to store the sample of *Cryptosporidium* with the concentration of $250\ \text{cell}/\mu L$, and phosphate buffer saline (PBS) is used as the buffer. Reservoirs 2 and 3 are used to store PBS. The PBS sample in Reservoir 2 is used as the washing buffer, and the one in Reservoir 3 is used as the sensing liquid. The capacitive biosensor is located on the top of one of the actuating electrodes in the middle of the chip design, as shown in Figure 7-1. Reservoir 4 is the waste reservoir which is used to collect all the sample droplets used for cell incubation, washing, and sensing.

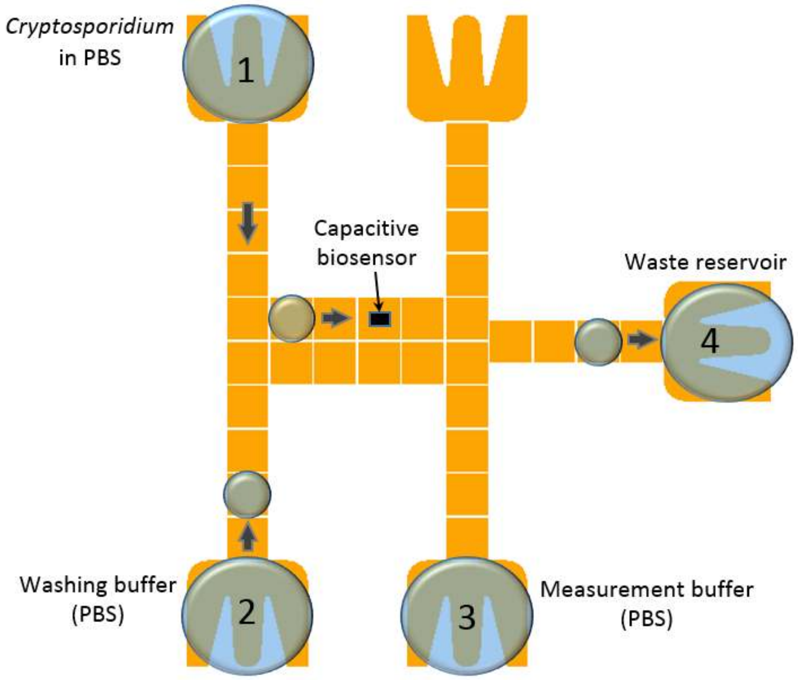

Figure 7-1 Schematic of the DMF chip used for the detection assay.

The bottom plate includes $2mm$ square electrodes fabricated using the procedure explained in Chapter 2. The gap height between the two plates is set to $250\mu m$. The top plate is a glass slide with the pattern of the capacitive biosensor and the ground electrode lines used for droplet manipulation. A part of the top plate located on the array of the electrodes on the bottom plate is shown in Figure 7-2. The top plate is covered with a cytop layer and the region covering the capacitive biosensor is removed using the method explained in Chapter 2 and Chapter 6. The capacitive biosensor includes interdigitated electrodes as shown in the zoomed image in Figure 7-2. The effective dimension of the biosensor (the removed cytop window) is $0.59mm \times 0.72mm$, which has an aspect ratio of $\gamma = 1.22$ and covers 10.6% of the area of an actuating electrode. Based on the results of Chapter 6, his area is within the appropriate range for the gap height of $250\mu m$ for complete droplet removal after biosensing. After opening the window through the cytop layer over the biosensor, the surface was functionalized with anti-*Cryptosporidium* antibodies, as the receptors to detect *Cryptosporidium*.

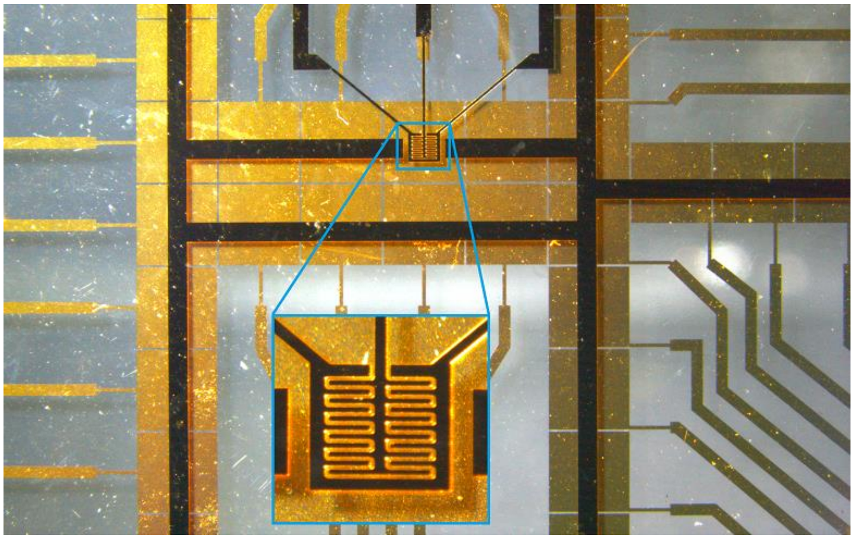

Figure 7-2 Capacitive biosensor and the ground electrode lines patterned on the top plate.

The voltage at a frequency of $1kHz$ and the threshold splitting amplitude (will be determined later on) was used for droplet actuation. This voltage was applied using a signal function generator (Tektronix AFG 3021B0) and amplified to the desired voltage (TREK PZD700). The capacitive measurement is performed using a network analyzer (N5241A, Agilent Technologies).

7.3 Detection results

The detection assay is performed by incubating a droplet of the *Cryptosporidium* sample on top of the biosensor, and then detecting with a droplet of PBS on the sensing surface. Therefore, for this method of detection the change in the volume of the droplets can alter the biosensing accuracy, as such a change can affect 1) the number of the captured cells and 2) the measured capacitance. To eliminate the deviation in the results due to the effect of the droplet volume, droplet splitting is performed using the high accuracy method developed in Chapter 3. For this purpose, first the threshold splitting voltage needs to be determined. For the device used in this Chapter, the threshold splitting voltage was found to be $82V$. The droplet actuation and splitting was performed using this voltage for the entire experiments.

The density of *Cryptosporidium* was found to be slightly higher than PBS, and hence the cells sedimented as the droplet was placed on a surface. This might cause non-uniformity in the distribution of the cells in the reservoir droplet. To avoid such an effect, the content of the *Cryptosporidium* sample was always gently mixed prior to dispensing a droplet for incubation on the biosensor. The mixing was performed using the electrohydrodynamic mixing technique developed in Chapter 4. For the actuation purpose, an applied voltage of $30V$ with a frequency of $5MHz$ was applied for $0.5s$ to levitate and mixed the cells within the sample. The non-symmetric geometry of the reservoir electrode facilitated the generation of non-uniformity, and resultant mixing inside the droplet.

The detection assay was performed for two cases. In the first case, the incubation was performed using the original *Cryptosporidium* sample. For this case, a droplet of PBS was first dispensed from Reservoir 4 and transported to the biosensor. The measurement was then performed to determine the capacitance of the interdigitated biosensor without the cells (C_0). Following this step, a droplet of *Cryptosporidium* is dispensed from Reservoir 1 (Figure 7-3a) and transported to the biosensor (Figure 7-3b). The sample is then incubated on the biosensor for 1 hr. The effect of evaporation of the droplets on the chip was minimized by saturating the air surrounding the device. After the incubation step, the droplet was removed away from the surface of the biosensor (Figure 7-3c) and transported to the waste reservoir. To remove the unbound cells from the biosensor, two droplets of PBS were dispensed from Reservoir 2 (Figure 7-4a), transported to the biosensor and then to the waste reservoir after washing the biosensing surface. Finally, to perform detection, a droplet of PBS was dispensed from Reservoir 4 (Figure 7-4b) and transported to the biosensor. The measurement was performed and the droplet was transported to the waste reservoir. The capacitance of the biosensor with the captured cells was also determined (C). The percentage of the change in the capacitance due to the presence of the cells was calculated as $\Delta C/C_0 \times 100$. The experiment was repeated three times and the standard deviation was calculated. The result is shown in Figure 7-5 and referred to as "Incubation Case I".

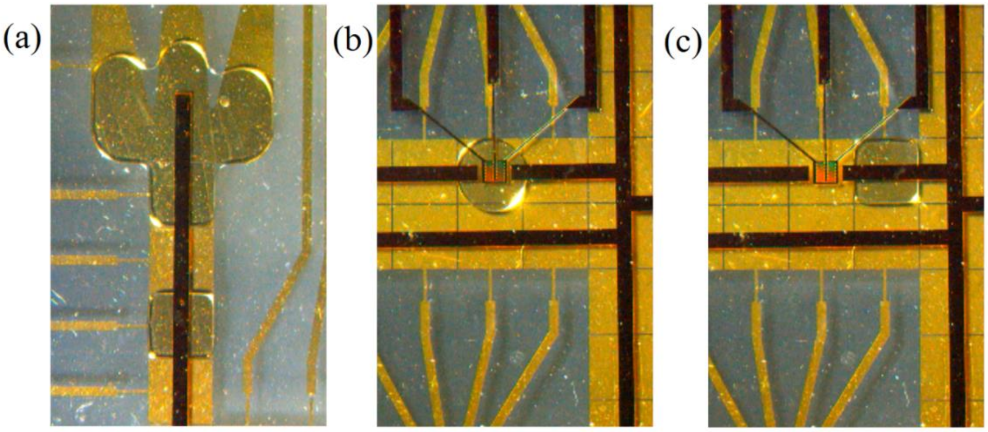

Figure 7-3 a) Dispensing a droplet from the original *Cryptosporidium* sample. b) Incubation of the *Cryptosporidium* sample on the biosensor. c) Removing the droplet away from the biosensor.

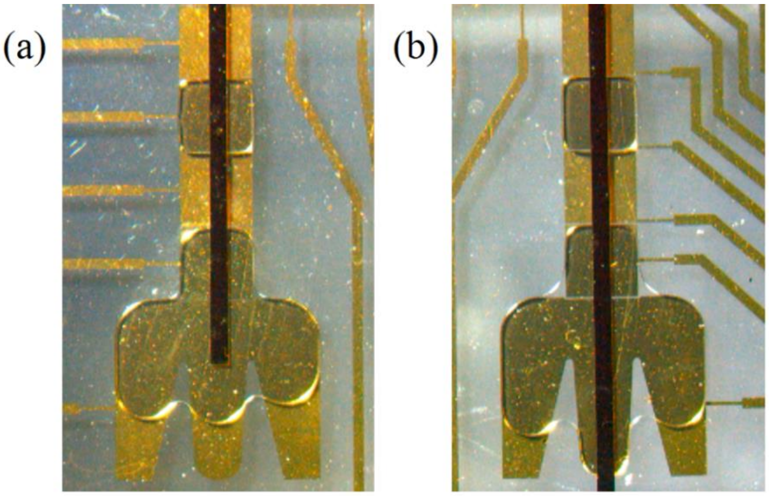

Figure 7-4 a) Dispensing a droplet of PBS from Reservoir 2 as the washing buffer. b) Dispensing a droplet of PBS from Reservoir 4 as the sensing buffer.

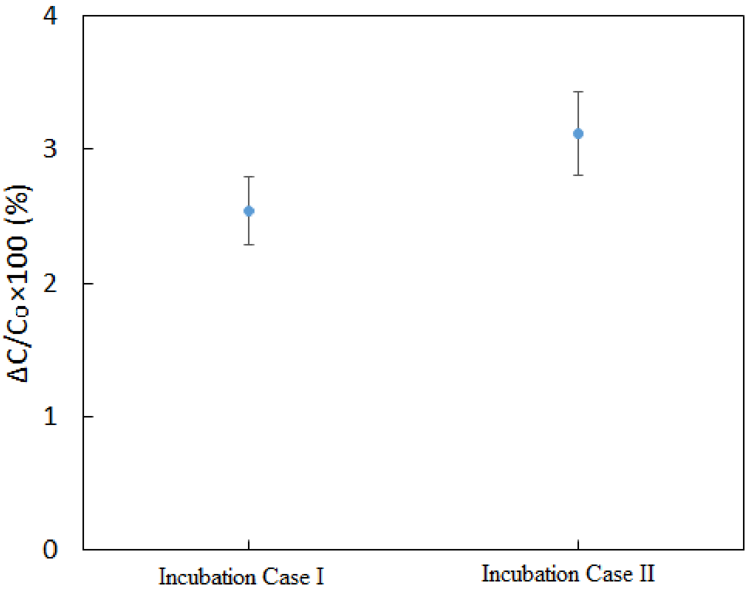

Figure 7-5 Results of the capacitive biosensing for Case I and Case II.

In the second case of incubation, the concentration of the cells inside the droplet was increased using the DGD technique (Chapter 4). For this purpose, a *Cryptosporidium* droplet was dispensed from Reservoir 1 using two actuating electrodes (Figure 7-6a), resulting a droplet with a larger volume (approximately double the size of the droplet in the first case). Using the

DGD method and by applying a voltage with the frequency of $200kHz$ and the amplitude of $50V$, the cells were concentrated into a smaller droplet. This process involved three steps: 1) The droplet was pulled slightly ($\sim 1/3$ of the length of the electrode) towards the upper electrode by EWOD. 2) By applying DGD for $30s$ to the same electrode (upper electrode, which was covered with a smaller portion of the droplet), the cells were pushed towards the lower side of the droplet. 3) Finally, the droplet was split to two parts (Figure 7-6b), one with a high and the other with the low concentrations of the cells. The low concentration droplet was transported to the waste reservoir. The high concentration droplet was used for incubation and detection, performed exactly similar to the first case. The result of the second case is also shown in Figure 7-5 labeled as "Incubation Case II". It can be observed that an increase in the signal has been achieved using the DGD method, confirming the applicability of the method for enhancing sample preparation and biosensing.

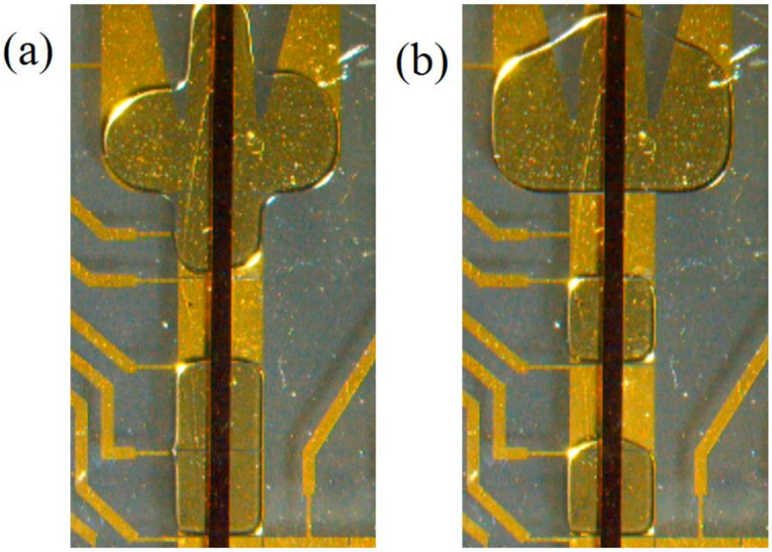

Figure 7-6 a) Splitting a big sample droplet using two actuated electrodes. b) Splitting the droplet to two parts after the cells are concentrated to one side (lower side) of the droplet.

7.4 Summary

A digital microfluidic (DMF) device was designed for detection of *Cryptosporidium,* as a proof of concept. The techniques and strategies proposed in previous chapters have all been integrated to perform the entire assay from sample preparation to post detection sample removal on DMF. Biosensing was performed using an interdigitated capacitive biosensor, functionalized with the anti-*Cryptosporidium* antibodies. The strategies developed in Chapter 3 were used for accurately splitting the droplets containing the sample, and the washing or sensing buffer. The electrohydrodynamic mixing method, which is explained in Chapter 4, was used to perform on-chip mixing through the reservoir sample droplet to maintain uniformity of the cells within the droplet. Also, the dielectrophoretic-gravity driven (DGD) method developed in Chapter 5 was used to increase the concentration of the cells inside the droplet. The geometry of the biosensor was designed and fabricated using the strategies developed in Chapter 6 to facilitate removal of the droplets from the hydrophilic surface of the biosensors, without the residual liquid on the surface. The enhanced detection signals from the capacitive biosensors show the capability of the methods proposed in this thesis for preforming biosensing on DMF platforms.

Chapter 8 Conclusions and future work

8.1 Summary

The focus of this research has been on the development of advanced operators for digital microfluidics (DMF) to enhance on-chip sample preparation and biosensing. Biochemical assays include several steps for manipulation and preparation of samples and detection of biochemical events. Miniaturization and integration of such assays on to DMF devices are associated with limitations due to the small and confined geometry of such devices, hindering the range of their applicability in biochemical and biomedical applications. In this thesis, several operators and strategies have been developed based on the physical properties of the chip and samples to overcome the limitations of DMF device in the areas related to sample preparation and biosensing. The physics behind these operators have been thoroughly explained in Chapters 3 to 6, and a successful application of these operators in performing a detection assay has been illustrated in Chapter 7. A conclusive summary of the developed operators is provided here.

8.1.1 Unequal splitting operator

An operator is developed by geometrical modification of a conventional electrode on DMF devices for unequal splitting and dispensing variable volumes of droplets. This has been performed by dividing one electrode to several smaller sub-electrodes which can be actuated individually. Depending on the number of the simultaneous actuated sub-electrodes, a wide range of droplet volumes could be dispensed or split. The optimized geometry of the sub-electrodes was found to be square. Also, it was shown that an applied voltage close to the threshold voltage provides over 99% accuracy of the split/dispensed droplets.

8.1.2 Rapid mixing operator

It is shown that by applying non-uniform high frequency electric field inside the droplets on DMF devices it is possible to generate circulation regions which can be used for mixing the droplet contents in stationary droplets. This technique was used for rapid mixing inside the droplets containing dye and microbeads (less than $1s$ for 95% uniformity) to characterize the method. The effects of the frequency and the amplitude of the applied voltage was studied on mixing time and it was found that increasing them enhances mixing time. However, there is a threshold value for each of the frequency and amplitude above which the droplet sheds satellite droplets. Therefore, an effective range was identified for rapid mixing without shedding satellite droplets. The droplet size showed to have a negative effect on the mixing time. In other words, mixing was achieved more rapidly for smaller droplets. The gap height between the two plates on the other hand showed that is directly related to the mixing time. The larger the gap height the more rapid the mixing process. Concentration of salts inside the droplets was shown to suppress mixing effect. For higher concentrations of salt the frequency and amplitude of the applied voltage has to be increased to maintain a high efficiency of mixing. Therefore, for high salt concentrations mixing was associated with satellite droplets. This issue could be solved by enhancing the dielectric properties of the insulating layer used for chip fabrication. The application of the method was also shown for on chip pH measurement and also mixing a sample containing DNA.

8.1.3 Particle focusing operator

Manipulation of cells and microbeads has always required the use of external modules such as magnet, or geometrically modification of the device for using phenomena such as dielectrophoresis (DEP). In this thesis, the dielectrophoretic-gravity-driven (DGD) technique has been developed which can be applied using the conventional electrodes and only by modulating the applied voltage to the chip. Using this technique, the cells or microbeads inside the sample could be focused on a certain point, or could be concentrated in one side of the droplet, followed by splitting, which results in a high concentration droplet and the other droplet with a low concentration of the cells or microbeads.

8.1.4 Biosensing operator

While the integration of biosensors onto DMF has been shown in a few studies, it is well-known that the hydrophilic surface of such biosensors can hinder removal of the droplets from their surface. In this thesis, a systematic study has been performed to characterize the hydrophilic behavior of such surfaces and optimize the geometry and the configuration of the biosensor and the DMF chip for successful droplet removal. It was found that higher aspect ratio of the biosensor facilitates droplet removal. Also, increasing the gap height was shown to enhance droplet removal. However, this is limited to the maximum height for which sample splitting and transport is accurately possible. The best location for placing the biosensor was found to be aligned with the center of an actuating electrode. Also, droplet volume did not have a significant effect on the droplet removal. Using the optimized geometry and configuration, a capacitive biosensor has been developed for the detection of *Cryptosporidium*. It is shown that the droplet can be removed completely from the biosensing surface after performing detection.

8.2 Contributions to the field

Each of the developed techniques can significantly benefit the field of lab-on-a-chip by providing a wider range of the applicability of the devices for performing biochemical experiments. The specific contributions of this research are summarized below:

- The unequal splitting operator can provide dispensing a wide range of droplet volumes and splitting droplets with a high volume ratio without any feedback control and sensing modules integrated to the device. Also, the accuracy of sample dispensing is over 99% which is a crucial factor in numerous biochemical assays. The main benefit of this operator is providing such abilities without any complications in the device fabrication or the addition of external modules..
- The electrohydrodynamic mixing method provides rapid mixing inside the droplets without the requirement of transporting the droplets in long cycles. This will increase the speed of the operation, reduces the chance of cross contamination due to the transport of the sample in multiple cycles, and also increases the device durability by avoiding the frequent transport of the biological samples such as proteins on the chip surface. A main advantage of the method is that it can be used using the conventional electrodes which eliminates the requirement for geometrically modification of the device, and also can be used at any location on the chip. This method can also be used for stationary mixing of the reservoir droplets to maintain their uniformity, and for circulation of the samples on the biosensors for increasing the chance of capturing the target analytes.
- The developed DGD method can provide focusing and concentration of the cells and microbeads on the DMF devices only by modulating the applied voltage. This techniques and does not require any modification of the device or adding external modules to the chip. Also, due to the application of the conventional electrodes for performing the operation, DGD can be used at any location on the chip.
- The characterization and optimization of the geometry of the hydrophilic surface of the biosensors has a great impact on the applicability of the biosensors on DMF devices.

Without such optimization, the removal of the droplets from the biosensors will be hindered, which means the chip cannot be further used after the first droplet is introduced to the biosensor integrated into the chip. Even for disposable chips, the assay might require delivery and removal of multiple droplets to the biosensor (e.g., for incubation of the analyte or washing steps). Therefore, regardless of the single or multiple application the chip and biosensor, it is crucial to follow the developed procedures for the optimization of the geometry of the biosensor on DMF devices.

8.3 Future work

- The unequal splitting and DGD techniques were developed and tested separately. Combination of these two operators provides a powerful tool for high throughput sample preparation on the chip by reducing the number of washing steps. It is recommended that these two methods are applied simultaneously for an immunodetection assay including microbeads. The combination of these two techniques will significantly enhance the speed and efficiency of the detection: without these operators, the washing steps may have to be repeated several times which is time consuming and results in the sample loss.
- The electrohydrodynamic mixing operator can provide a significant increase in the speed of the assays including sample mixing. It is recommended that this operator is used for applications such as polymerase chain reaction (PCR) and the speed of the assay is compared with conventional mixing methods. Also, this operator can be used for biosensing purposes, in which the sample containing the target analyte is circulated on the sensing surface to increase the chance of capturing the target analyte using the bioreceptors. In addition to such applications, the effects of different types of salt on the

mixing performance could also be studied and different salts have different solubility in the solvents.

- The application of the DGD operator was shown for the case of microbeads. Therefore, the focus has been on the physical properties of the operator and the samples. It is recommended to perform the DGD operator for manipulating a wide range of cells and perform a viability study on them to evaluate the range of the applicability of the method for cell applications. Following that, DGD can be used for performing cell patterning and cell culture on DMF devices.
- The regeneration of the biosensors on DMF devices includes two steps. The first step which is the mechanical removal of the sample from the biosensor was developed and tested in this thesis. The second step is breaking the bonds between the target analyte and the receptors without damaging the receptors for further biosensing. This step varies from one application to another. It is recommended to perform multiple studies for biological regeneration of the biosensor (along with mechanical regeneration) for different applications on DMF devices. Following that, a study can be conducted to perform multiple cycles of detection using one biosensor, which will be a significant step towards developing durable devices for point-of-care applications.

References

1. Haeberle, S. and R. Zengerle, Microfluidic platforms for lab-on-a-chip applications. Lab on a Chip, 2007. 7(9): p. 1094-1110.
2. Le, H.P., Progress and trends in ink-jet printing technology. Journal of Imaging Science and Technology, 1998. 42(1): p. 49-62.
3. Clark, T.J., P.H. McPherson, and K.F. Buechler, The triage cardiac panel: Cardiac markers for the triage system. Point of Care, 2002. 1(1): p. 42-46.
4. Xia, Y., et al., Complex optical surfaces formed by replica molding against elastomeric masters. Science, 1996. 273(5273): p. 347-349.
5. Madou, M., et al., Lab on a CD. Annu. Rev. Biomed. Eng., 2006. 8: p. 601-628.
6. Krupke, R., et al., Separation of metallic from semiconducting single-walled carbon nanotubes. Science, 2003. 301(5631): p. 344-347.
7. Nisisako, T., T. Torii, and T. Higuchi, Droplet formation in a microchannel network. Lab on a Chip, 2002. 2(1): p. 24-26.
8. He, M., et al., Selective encapsulation of single cells and subcellular organelles into picoliter-and femtoliter-volume droplets. Analytical Chemistry, 2005. 77(6): p. 1539-1544.
9. Pollack, M.G., R.B. Fair, and A.D. Shenderov, Electrowetting-based actuation of liquid droplets for microfluidic applications. Applied Physics Letters, 2000. 77(11): p. 1725-1726.
10. Gutmann, O., et al., A highly parallel nanoliter dispenser for microarray fabrication. Biomedical microdevices, 2004. 6(2): p. 131-137.
11. Choi, K., et al., Digital microfluidics. Annual review of analytical chemistry, 2012. 5: p. 413-440.
12. Fair, R.B., Digital microfluidics: is a true lab-on-a-chip possible? Microfluidics and Nanofluidics, 2007. 3(3): p. 245-281.

13. Teh, S.-Y., et al., Droplet microfluidics. Lab on a Chip, 2008. 8(2): p. 198-220.

14. Cho, S.K., H. Moon, and C.-J. Kim, Creating, transporting, cutting, and merging liquid droplets by electrowetting-based actuation for digital microfluidic circuits. Microelectromechanical Systems, Journal of, 2003. 12(1): p. 70-80.

15. Gong, J. and C.-J.C. Kim. Two-dimensional digital microfluidic system by multilayer printed circuit board. in Micro Electro Mechanical Systems, 2005. MEMS 2005. 18th IEEE International Conference on. 2005. IEEE.

16. Böhringer, K.F., Modeling and controlling parallel tasks in droplet-based microfluidic systems. Computer-Aided Design of Integrated Circuits and Systems, IEEE Transactions on, 2006. 25(2): p. 334-344.

17. Ren, H., R.B. Fair, and M.G. Pollack, Automated on-chip droplet dispensing with volume control by electro-wetting actuation and capacitance metering. Sensors and Actuators B: Chemical, 2004. 98(2): p. 319-327.

18. Gong, J., All-electronic droplet generation on-chip with real-time feedback control for EWOD digital microfluidics. Lab on a Chip, 2008. 8(6): p. 898-906.

19. Liu, Y., A. Banerjee, and I. Papautsky, Precise droplet volume measurement and electrode-based volume metering in digital microfluidics. Microfluidics and Nanofluidics, 2014. 17(2): p. 295-303.

20. Paik, P., et al. Coplanar digital microfluidics using standard printed circuit board processes. in Proc. Intl. Conf. on MicroTAS. 2005. Citeseer.

21. Yi, U.-C. and C.-J. Kim, Characterization of electrowetting actuation on addressable single-side coplanar electrodes. Journal of Micromechanics and Microengineering, 2006. 16(10): p. 2053.

22. Abdelgawad, M. and A.R. Wheeler, The digital revolution: a new paradigm for microfluidics. Adv. Mater, 2009. 21(8): p. 920-925.

23. Samiei, E., H. Rezaeinejad and M. Hoorfar, Droplet dispensing from open to close digital microfluidic platforms, in World innovation conference and Expo (Nanotech). 2014: Washington D.C., USA.

24. Pollack, M., A. Shenderov, and R. Fair, Electrowetting-based actuation of droplets for integrated microfluidics. Lab on a Chip, 2002. 2(2): p. 96-101.

25. Velev, O.D., B.G. Prevo, and K.H. Bhatt, On-chip manipulation of free droplets. Nature, 2003. 426(6966): p. 515-516.

26. Hunt, T.P., D. Issadore, and R.M. Westervelt, Integrated circuit/microfluidic chip to programmably trap and move cells and droplets with dielectrophoresis. Lab on a Chip, 2008. 8(1): p. 81-87.

27. Renaudin, A., et al., Surface acoustic wave two-dimensional transport and location of microdroplets using echo signal. Journal of applied physics, 2006. 100(11): p. 116101.

28. Guttenberg, Z., et al., Planar chip device for PCR and hybridization with surface acoustic wave pump. Lab on a Chip, 2005. 5(3): p. 308-317.

29. Guo, Z.-G., et al., “Stick and slide” ferrofluidic droplets on superhydrophobic surfaces. Applied physics letters, 2006. 89(8): p. 081911.

30. Lehmann, U., et al., Two-dimensional magnetic manipulation of microdroplets on a chip as a platform for bioanalytical applications. Sensors and Actuators B: Chemical, 2006. 117(2): p. 457-463.

31. Chen, J.Z., et al., Effect of contact angle hysteresis on thermocapillary droplet actuation. Journal of applied physics, 2005. 97(1): p. 014906.

32. Darhuber, A.A., et al., Thermocapillary actuation of droplets on chemically patterned surfaces by programmable microheater arrays. Microelectromechanical Systems, Journal of, 2003. 12(6): p. 873-879.

33. Pei, S.N., et al. Light-actuated digital microfluidics for large-scale, parallel manipulation of arbitrarily sized droplets. in Micro Electro Mechanical Systems (MEMS), 2010 IEEE 23rd International Conference on. 2010. IEEE.

34. Chiou, P.Y., et al., Light actuation of liquid by optoelectrowetting. Sensors and actuators A: physical, 2003. 104(3): p. 222-228.

35. Khaw, M.K., et al., Digital microfluidics with magnetically actuated floating liquid marble. Lab on a Chip, 2016, 16: p. 2211-2218.

36. Mugele, F. and J.-C. Baret, Electrowetting: from basics to applications. Journal of Physics: Condensed Matter, 2005. 17(28): p. R705.

37. Washizu, M., Electrostatic actuation of liquid droplets for micro-reactor applications. Industry Applications, IEEE Transactions on, 1998. 34(4): p. 732-737.

38. Vallet, M., B. Berge, and L. Vovelle, Electrowetting of water and aqueous solutions on poly (ethylene terephthalate) insulating films. Polymer, 1996. 37(12): p. 2465-2470.

39. Jebrail, M.J., M.S. Bartsch, and K.D. Patel, Digital microfluidics: a versatile tool for applications in chemistry, biology and medicine. Lab on a Chip, 2012. 12(14): p. 2452-2463.

40. Kaler, K.V. and R. Prakash, Droplet microfluidics for chip-based diagnostics. Sensors, 2014. 14(12): p. 23283-23306.

41. Rackus, D.G., M.H. Shamsi, and A.R. Wheeler, Electrochemistry, biosensors and microfluidics: a convergence of fields. Chemical Society Reviews, 2015, 44: p. 5320-5340.

42. Pollack, M.G., et al., Applications of electrowetting-based digital microfluidics in clinical diagnostics. 2011, 11(4): p. 393-407.

43. Ng, A.H., et al., Digital Microfluidic Cell Culture. Annual Review of Biomedical Engineering, 2015. 17(1): p. 91-112.

44. He, J.-L., et al., Digital Microfluidics for Manipulation and Analysis of a Single Cell. International journal of molecular sciences, 2015. 16(9): p. 22319-22332.

45. Malic, L., et al., Integration and detection of biochemical assays in digital microfluidic LOC devices. Lab on a Chip, 2010. 10(4): p. 418-431.

46. Moon, H., et al., An integrated digital microfluidic chip for multiplexed proteomic sample preparation and analysis by MALDI-MS. Lab on a Chip, 2006. 6(9): p. 1213-1219.

47. Lin, Y.-Y., et al., Low voltage electrowetting-on-dielectric platform using multi-layer insulators. Sensors and Actuators B: Chemical, 2010. 150(1): p. 465-470.

48. Gong, J., S.-K. Fan, and C.-J. Kim. Portable digital microfluidics platform with active but disposable lab-on-chip. in Micro Electro Mechanical Systems, 2004. 17th IEEE International Conference on.(MEMS). 2004. IEEE.

49. Martinez, A.W., et al., Diagnostics for the developing world: microfluidic paper-based analytical devices. Analytical chemistry, 2009. 82(1): p. 3-10.

50. Abadian, A. and S. Jafarabadi-Ashtiani, Paper-based digital microfluidics. Microfluidics and Nanofluidics, 2014. 16(5): p. 989-995.

51. Yafia, M., S. Shukla, and H. Najjaran, Fabrication of digital microfluidic devices on flexible paper-based and rigid substrates via screen printing. Journal of Micromechanics and Microengineering, 2015. 25(5): p. 057001.

52. Ko, H., et al., Active Digital Microfluidic Paper Chips with Inkjet-Printed Patterned Electrodes. Advanced Materials, 2014. 26(15): p. 2335-2340.

53. Fobel, R., et al., Paper microfluidics goes digital. Advanced materials, 2014. 26(18): p. 2838-2843.

54. Monkkonen, L., et al., Screen-Printed Digital Microfluidics Combined with Surface Acoustic Wave Nebulization for Hydrogen-Deuterium Exchange Measurements. Journal of Chromatography A, 2015, 1439: p. 161-166.

55. Sista, R.S., et al., Multiplex newborn screening for Pompe, Fabry, Hunter, Gaucher, and Hurler diseases using a digital microfluidic platform. Clinica Chimica Acta, 2013. 424: p. 12-18.

56. Leiterer, C., et al. Printed circuit boards as platform for disposable lab-on-a-chip applications. in SPIE Micro+ Nano Materials, Devices, and Applications. 2015. International Society for Optics and Photonics.

57. Barbulovic-Nad, I., et al., Digital microfluidics for cell-based assays. Lab on a Chip, 2008. 8(4): p. 519-526.

58. Srinivasan, V., V.K. Pamula, and R.B. Fair, Droplet-based microfluidic lab-on-a-chip for glucose detection. Analytica Chimica Acta, 2004. 507(1): p. 145-150.

59. Nejad, H.R., et al., Characterization of the geometry of negative dielectrophoresis traps for particle immobilization in digital microfluidic platforms. Lab on a chip, 2013. 13(9): p. 1823-1830.

60. Vallet, M., M. Vallade, and B. Berge, Limiting phenomena for the spreading of water on polymer films by electrowetting. The European Physical Journal B-Condensed Matter and Complex Systems, 1999. 11(4): p. 583-591.

61. Peykov, V., A. Quinn, and J. Ralston, Electrowetting: a model for contact-angle saturation. Colloid and Polymer Science, 2000. 278(8): p. 789-793.

62. Cho, S.K., et al. Towards digital microfluidic circuits: creating, transporting, cutting and merging liquid droplets by electrowetting-based actuation. in Micro Electro Mechanical Systems, 2002. The Fifteenth IEEE International Conference on. 2002. IEEE.

63. Yafia, M. and H. Najjaran, High precision control of gap height for enhancing principal digital microfluidics operations. Sensors and Actuators B: Chemical, 2013. 186: p. 343-352.

64. Foudeh, A.M., et al., Rapid and multiplex detection of Legionella's RNA using digital microfluidics. Lab on a Chip, 2015. 15(6): p. 1609-1618.

65. Moon, H., S.K. Cho, and R.L. Garrell, Low voltage electrowetting-on-dielectric. Journal of applied physics, 2002. 92(7): p. 4080-4087.

66. Li, Y., et al., Anodic Ta 2 O 5 for CMOS compatible low voltage electrowetting-on-dielectric device fabrication. Solid-State Electronics, 2008. 52(9): p. 1382-1387.

67. Shibata, S., Dielectric constants of Ta 2 O 5 thin films deposited by rf sputtering. Thin Solid Films, 1996. 277(1): p. 1-4.

68. Lin, Y.-Y., E.R. Welch, and R.B. Fair, Low voltage picoliter droplet manipulation utilizing electrowetting-on-dielectric platforms. Sensors and Actuators B: Chemical, 2012. 173: p. 338-345.

69. Narasimhan, V. and S.-Y. Park, An Ion Gel as a Low-Cost, Spin-Coatable, High-Capacitance Dielectric for Electrowetting-on-Dielectric (EWOD). Langmuir, 2015. 31(30): p. 8512-8518.

70. Luk, V.N., G.C. Mo, and A.R. Wheeler, Pluronic additives: a solution to sticky problems in digital microfluidics. Langmuir, 2008. 24(12): p. 6382-6389.

71. Gong, J. and C.-J. Kim, Direct-referencing two-dimensional-array digital microfluidics using multilayer printed circuit board. Microelectromechanical Systems, Journal of, 2008. 17(2): p. 257-264.

72. Hadwen, B., et al., Programmable large area digital microfluidic array with integrated droplet sensing for bioassays. Lab on a Chip, 2012. 12(18): p. 3305-3313.

73. Ahamedi, M.J., R. Ben-Mrad, and P. Sullivan, Electrowetting on Dielectric (EWOD)-based thermo-responsive microvalve for interfacing droplet flow with continuous flow. Microelectromechanical Systems, Journal of, 2013. 22(3): p. 536-541.

74. Watson, M.W., M.J. Jebrail, and A.R. Wheeler, Multilayer hybrid microfluidics: A digital-to-channel interface for sample processing and separations. Analytical chemistry, 2010. 82(15): p. 6680-6686.

75. Paknahad, M., H.R. Nejad, and M. Hoorfar, Development of a Digital Micropump with Controlled Flow Rate for Microfluidic Platforms. Sensors & Transducers, 2014. 183(12): p. 84.

76. Banerjee, A., et al., Programmable Electrowetting with Channels and Droplets. Micromachines, 2015. 6(2): p. 172-185.

77. Shih, S.C., et al., A droplet-to-digital (D2D) microfluidic device for single cell assays. Lab on a Chip, 2015. 15(1): p. 225-236.

78. Berge, B., Electrocapillarité et mouillage de films isolants par l'eau. Comptes rendus de l'Académie des sciences. Série 2, Mécanique, Physique, Chimie, Sciences de l'univers, Sciences de la Terre, 1993. 317(2): p. 157-163.

79. Quilliet, C. and B. Berge, Electrowetting: a recent outbreak. Current Opinion in Colloid & Interface Science, 2001. 6(1): p. 34-39.

80. Hong, J.S., et al., A numerical investigation on AC electrowetting of a droplet. Microfluidics and Nanofluidics, 2008. 5(2): p. 263-271.

81. Jones, T.B., et al., Frequency-based relationship of electrowetting and dielectrophoretic liquid microactuation. Langmuir, 2003. 19(18): p. 7646-7651.

82. Jones, T.B., K.-L. Wang, and D.-J. Yao, Frequency-dependent electromechanics of aqueous liquids: electrowetting and dielectrophoresis. Langmuir, 2004. 20(7): p. 2813-2818.

83. Dong, C., et al., On the droplet velocity and electrode lifetime of digital microfluidics: voltage actuation techniques and comparison. Microfluidics and Nanofluidics, 2015. 18(4): p. 673-683.

84. Paik, P., et al., Electrowetting-based droplet mixers for microfluidic systems. Lab on a Chip, 2003. 3(1): p. 28-33.

85. Fowler, J., H. Moon, and C.K. CHANG-JIN. Enhancement of mixing by droplet-based microfluidics. in Proceedings, IEEE micro electro mechanical systems. 2002.

86. Mugele, F., J. Baret, and D. Steinhauser, Microfluidic mixing through electrowetting-induced droplet oscillations. Applied Physics Letters, 2006. 88(20): p. 204106-204106.

87. Theisen, J. and L. Davoust, Mass transfer enhancement and surface functionalization in digital microfluidics using AC electrowetting: the smaller, the better. Microfluidics and Nanofluidics, 2015. 18(5-6): p. 1373-1389.

88. Samiei, E. and M. Hoorfar. Modifying Electrode Geometry for Unequal Droplet Splitting in Digital Microfluidics. in ASME 2013 International Mechanical Engineering Congress and Exposition. 2013. American Society of Mechanical Engineers.

89. Berthier, J., et al., Computer aided design of an EWOD microdevice. Sensors and Actuators A: Physical, 2006. 127(2): p. 283-294.

90. Berthier, J., et al., An analytical model for the prediction of microdrop extraction and splitting in digital microfluidics systems. Young, 2005. 9(2): p. 0-2.

91. Banerjee, A., et al., Deterministic splitting of fluid volumes in electrowetting microfluidics. Lab on a Chip, 2012. 12(24): p. 5138-5141.

92. Armani, M., et al., Control of microfluidic systems: two examples, results, and challenges. International Journal of Robust and Nonlinear Control, 2005. 15(16): p. 785-803.

93. Luan, L., et al., Integrated optical sensor in a digital microfluidic platform. Sensors Journal, IEEE, 2008. 8(5): p. 628-635.

94. Wang, K.-L., T.B. Jones, and A. Raisanen, DEP actuated nanoliter droplet dispensing using feedback control. Lab on a Chip, 2009. 9(7): p. 901-909.

95. Bhattacharjee, B. and H. Najjaran, Droplet position control in digital microfluidic systems. Biomedical microdevices, 2010. 12(1): p. 115-124.

96. Bhattacharjee, B. and H. Najjaran, Simulation of droplet position control in digital microfluidic systems. Journal of dynamic systems, measurement, and control, 2010. 132(1): p. 014501.

97. Niu, X., et al., Real-time detection, control, and sorting of microfluidic droplets. Biomicrofluidics, 2007. 1(4): p. 044101.

98. Shih, S.C., et al., A feedback control system for high-fidelity digital microfluidics. Lab on a Chip, 2011. 11(3): p. 535-540.

99. Schertzer, M., R. Ben-Mrad, and P.E. Sullivan, Using capacitance measurements in EWOD devices to identify fluid composition and control droplet mixing. Sensors and Actuators B: Chemical, 2010. 145(1): p. 340-347.

100. Bhattacharjee, B. and H. Najjaran, Droplet sensing by measuring the capacitance between coplanar electrodes in a digital microfluidic system. Lab on a Chip, 2012. 12(21): p. 4416-4423.

101. Chen, J.Z., et al., Capacitive sensing of droplets for microfluidic devices based on thermocapillary actuation. Lab on a Chip, 2004. 4(5): p. 473-480.

102. Elbuken, C., et al., Detection of microdroplet size and speed using capacitive sensors. Sensors and Actuators A: Physical, 2011. 171(2): p. 55-62.

103. Su, F., W. Hwang, and K. Chakrabarty. Droplet routing in the synthesis of digital microfluidic biochips. in Design, Automation and Test in Europe, 2006. DATE'06. Proceedings. 2006. IEEE.

104. Dhal, D., et al., A New Move Toward Parallel Assay Operations in a Restricted Sized Chip in Digital Microfluidics. Applied Computation and Security Systems. 2015, 305: p. 157-182.

105. Li, Z., T.-Y. Ho, and K. Chakrabarty, Optimization of 3D Digital Microfluidic Biochips for the Multiplexed Polymerase Chain Reaction. ACM Transactions on Design Automation of Electronic Systems (TODAES), 2016. 21(2): p. 25.

106. Roy, P., et al. 3D integration in biochips: New proposed architectures for 3D applications in ATDA based digital microfluidic biochips. in Design & Technology of Integrated Systems in Nanoscale Era (DTIS), 2015 10th International Conference on. 2015. IEEE.

107. Yoon, J.-Y. and R.L. Garrell, Preventing biomolecular adsorption in electrowetting-based biofluidic chips. Analytical Chemistry, 2003. 75(19): p. 5097-5102.

108. Srinivasan, V., V.K. Pamula, and R.B. Fair, An integrated digital microfluidic lab-on-a-chip for clinical diagnostics on human physiological fluids. Lab on a Chip, 2004. 4(4): p. 310-315.

109. Fair, R.B., et al., Chemical and biological applications of digital-microfluidic devices. Design & Test of Computers, IEEE, 2007. 24(1): p. 10-24.

110. Bayiati, P., et al., Electrowetting on plasma-deposited fluorocarbon hydrophobic films for biofluid transport in microfluidics. Journal of applied physics, 2007. 101(10): p. 103306.

111. Yang, H., et al., A world-to-chip interface for digital microfluidics. Analytical Chemistry, 2008. 81(3): p. 1061-1067.

112. Prakash, R., et al., Dielectrophoretic liquid actuation on nano-textured super hydrophobic surfaces. Sensors and Actuators B: Chemical, 2013. 182: p. 351-361.

113. Prakash, R., et al., Multiplex, quantitative, reverse transcription pcr detection of influenza viruses using droplet microfluidic technology. Micromachines, 2014. 6(1): p. 63-79.

114. Fan, S.-K., et al., Cross-scale electric manipulations of cells and droplets by frequency-modulated dielectrophoresis and electrowetting. Lab on a Chip, 2008. 8(8): p. 1325-1331.

115. Agastin, S., M.R. King, and T.B. Jones, Rapid enrichment of biomolecules using simultaneous liquid and particulate dielectrophoresis. Lab on a Chip, 2009. 9(16): p. 2319-2325.

116. Nejad, H.R., et al., Gravity-driven hydrodynamic particle separation in digital microfluidic systems. RSC Advances, 2015. 5(45): p. 35966-35975.

117. Wang, Y., Y. Zhao, and S.K. Cho, Efficient in-droplet separation of magnetic particles for digital microfluidics. Journal of Micromechanics and Microengineering, 2007. 17(10): p. 2148.

118. Zhao, Y., U.-C. Yi, and S.K. Cho, Microparticle concentration and separation by traveling-wave dielectrophoresis (twDEP) for digital microfluidics. Microelectromechanical Systems, Journal of, 2007. 16(6): p. 1472-1481.

119. Martel, J.M. and M. Toner, Particle focusing in curved microfluidic channels. Scientific Reports, 2013. 3: p. 3340.

120. Xuan, X., J. Zhu, and C. Church, Particle focusing in microfluidic devices. Microfluidics and nanofluidics, 2010. 9(1): p. 1-16.

121. Bhagat, A.A.S., et al., Microfluidics for cell separation. Medical & biological engineering & computing, 2010. 48(10): p. 999-1014.

122. Amini, H., et al., Intrinsic particle-induced lateral transport in microchannels. Proceedings of the National Academy of Sciences, 2012. 109(29): p. 11593-11598.

123. Shah, G.J., et al., EWOD-driven droplet microfluidic device integrated with optoelectronic tweezers as an automated platform for cellular isolation and analysis. Lab on a Chip, 2009. 9(12): p. 1732-1739.

124. Nestor, B., et al., Digital microfluidic platform for dielectrophoretic patterning of cells encapsulated in hydrogel droplets. RSC Advances, 2016. 6(62): p. 57409-57416.

125. Sista, R.S., et al., Heterogeneous immunoassays using magnetic beads on a digital microfluidic platform. Lab on a Chip, 2008. 8(12): p. 2188-2196.

126. Huang, C.-Y., et al., A highly efficient bead extraction technique with low bead number for digital microfluidic immunoassay. Biomicrofluidics, 2016. 10(1): p. 011901.

127. Chen, L. and R.B. Fair, Digital microfluidics chip with integrated intra-droplet magnetic bead manipulation. Microfluidics and Nanofluidics, 2015. 19(6): p. 1349-1361.

128. Zhao, Y. and S.K. Cho, Microparticle sampling by electrowetting-actuated droplet sweeping. Lab on a Chip, 2006. 6(1): p. 137-144.

129. Cho, S.K. and Y. Zhao, Concentration and binary separation of micro particles for droplet-based digital microfluidics. Lab on a Chip, 2007. 7(4): p. 490-498.

130. Nejad, H.R. and M. Hoorfar, Purification of a droplet using negative dielectrophoresis traps in digital microfluidics. Microfluidics and Nanofluidics, 2014. 18(3): p. 483-492.

131. Sista, R., et al., Development of a digital microfluidic platform for point of care testing. Lab on a Chip, 2008. 8(12): p. 2091-2104.

132. Li, Z., T.-Y. Ho, and K. Chakrabarty. Optimization of heaters in a digital microfluidic biochip for the polymerase chain reaction. in Thermal Investigations of ICs and Systems (THERMINIC), 2014 20th International Workshop on. 2014. IEEE.

133. Kuswandi, B., J. Huskens, and W. Verboom, Optical sensing systems for microfluidic devices: a review. Analytica chimica acta, 2007. 601(2): p. 141-155.

134. Luka, G., et al., Microfluidics integrated biosensors: A leading technology towards lab-on-a-chip and sensing applications. Sensors, 2015. 15(12): p. 30011-30031.

135. Zhou, Y., et al., Enzyme-based electrochemical biosensor for sensitive detection of DNA demethylation and the activity of DNA demethylase. Analytica chimica acta, 2014. 840: p. 28-32.

136. Amine, A., et al., Recent advances in biosensors based on enzyme inhibition. Biosensors and Bioelectronics, 2016. 76: p. 180-194.

137. Srinivasan, V., et al. A digital microfluidic biosensor for multianalyte detection. in Micro Electro Mechanical Systems, 2003. MEMS-03 Kyoto. IEEE The Sixteenth Annual International Conference on. 2003. IEEE.

138. Samiei, E., et al., Integration of biosensors into digital microfluidics: impact of hydrophilic surface of biosensors on droplet manipulation. Biosensors and Bioelectronics, 2016, 81: 480-486.

139. Choi, K., et al., Integration of field effect transistor-based biosensors with a digital microfluidic device for a lab-on-a-chip application. Lab on a Chip, 2012. 12(8): p. 1533-1539.

140. Lin, H., et al., Microfluidic approaches to rapid and efficient aptamer selection. Biomicrofluidics, 2014. 8(4): p. 041501.

141. Jia, X., S. Dong, and E. Wang, Engineering the bioelectrochemical interface using functional nanomaterials and microchip technique toward sensitive and portable electrochemical biosensors. Biosensors and Bioelectronics, 2016. 76: p. 80-90.

142. Vergauwe, N., et al., A versatile electrowetting-based digital microfluidic platform for quantitative homogeneous and heterogeneous bio-assays. Journal of Micromechanics and Microengineering, 2011. 21(5): p. 054026.

143. Myers, F.B. and L.P. Lee, Innovations in optical microfluidic technologies for point-of-care diagnostics. Lab on a Chip, 2008. 8(12): p. 2015-2031.

144. Liu, Y.-J., et al., DNA ligation of ultramicro volume using an EWOD microfluidic system with coplanar electrodes. Journal of Micromechanics and Microengineering, 2008. 18(4): p. 045017.

145. Chang, Y.-H., et al., Integrated polymerase chain reaction chips utilizing digital microfluidics. Biomedical microdevices, 2006. 8(3): p. 215-225.

146. Dubois, P., et al., Ionic liquid droplet as e-microreactor. Analytical Chemistry, 2006. 78(14): p. 4909-4917.

147. Xu, W., et al., Miniaturization of mass spectrometry analysis systems. Journal of the Association for Laboratory Automation, 2010. 15(6): p. 433-439.

148. Baker, C.A. and M.G. Roper, Online coupling of digital microfluidic devices with mass spectrometry detection using an eductor with electrospray ionization. Analytical chemistry, 2012. 84(6): p. 2955-2960.

149. Choi, K., et al., A digital microfluidic interface between solid-phase microextraction and liquid chromatography–mass spectrometry. Journal of Chromatography A, 2016. 1444: p. 1-7.

150. Homola, J., Present and future of surface plasmon resonance biosensors. Analytical and bioanalytical chemistry, 2003. 377(3): p. 528-539.

151. Hoa, X., A. Kirk, and M. Tabrizian, Towards integrated and sensitive surface plasmon resonance biosensors: a review of recent progress. Biosensors and Bioelectronics, 2007. 23(2): p. 151-160.

152. Miller, E.M. and A.R. Wheeler, A digital microfluidic approach to homogeneous enzyme assays. Analytical Chemistry, 2008. 80(5): p. 1614-1619.

153. Norian, H., et al., An integrated CMOS quantitative-polymerase-chain-reaction lab-on-chip for point-of-care diagnostics. Lab on a Chip, 2014. 14(20): p. 4076-4084.

154. Luk, V.N. and A.R. Wheeler, A digital microfluidic approach to proteomic sample processing. Analytical chemistry, 2009. 81(11): p. 4524-4530.

155. Zhang, K.-D., et al., Reliability Study on Compact and Portable Chemiluminescence Detector. International Journal of Automation and Smart Technology, 2014. 4(4): p. 222-227.

156. Shamsi, M.H., et al., Electrochemiluminescence on digital microfluidics for microRNA analysis. Biosensors and Bioelectronics, 2016. 77: p. 845-852.

157. Malic, L., T. Veres, and M. Tabrizian, Biochip functionalization using electrowetting-on-dielectric digital microfluidics for surface plasmon resonance imaging detection of DNA hybridization. Biosensors and Bioelectronics, 2009. 24(7): p. 2218-2224.

158. Malic, L., T. Veres, and M. Tabrizian, Two-dimensional droplet-based surface plasmon resonance imaging using electrowetting-on-dielectric microfluidics. Lab on a Chip, 2009. 9(3): p. 473-475.

159. Malic, L., T. Veres, and M. Tabrizian, Nanostructured digital microfluidics for enhanced surface plasmon resonance imaging. Biosensors and Bioelectronics, 2011. 26(5): p. 2053-2059.

160. Nichols, K.P. and J. Gardeniers, A digital microfluidic system for the investigation of pre-steady-state enzyme kinetics using rapid quenching with MALDI-TOF mass spectrometry. Analytical chemistry, 2007. 79(22): p. 8699-8704.

161. Shih, S.C., et al., Dried blood spot analysis by digital microfluidics coupled to nanoelectrospray ionization mass spectrometry. Analytical chemistry, 2012. 84(8): p. 3731-3738.

162. Kirby, A.E. and A.R. Wheeler, Digital microfluidics: an emerging sample preparation platform for mass spectrometry. Analytical chemistry, 2013. 85(13): p. 6178-6184.

163. Feng, X., et al., Advances in coupling microfluidic chips to mass spectrometry. Mass spectrometry reviews, 2015. 34(5): p. 535-557.

164. Liu, C., et al., Direct Interface between Digital Microfluidics and High Performance Liquid Chromatography–Mass Spectrometry. Analytical chemistry, 2015, 87(24): p. 11967-11972.

165. Yu, Y., J. Chen, and J. Zhou, Parallel-plate lab-on-a-chip based on digital microfluidics for on-chip electrochemical analysis. Journal of Micromechanics and Microengineering, 2014. 24(1): p. 015020.

166. Karuwan, C., et al., Electrochemical detection on electrowetting-on-dielectric digital microfluidic chip. Talanta, 2011. 84(5): p. 1384-1389.

167. Zheng, G., et al., Multiplexed electrical detection of cancer markers with nanowire sensor arrays. Nature biotechnology, 2005. 23(10): p. 1294-1301.

168. Hunt, H.K. and A.M. Armani, Label-free biological and chemical sensors. Nanoscale, 2010. 2(9): p. 1544-1559.

169. Berthier, J., Micro-drops and digital microfluidics. 2012: William Andrew.

170. Miller, E.M. and A.R. Wheeler, Digital bioanalysis. Analytical and bioanalytical chemistry, 2009. 393(2): p. 419-426.

171. Wulff-Burchfield, E., et al., Microfluidic platform versus conventional real-time polymerase chain reaction for the detection of Mycoplasma pneumoniae in respiratory specimens. Diagnostic microbiology and infectious disease, 2010. 67(1): p. 22-29.

172. Sista, R.S., et al., Digital microfluidic platform for multiplexing enzyme assays: implications for lysosomal storage disease screening in newborns. Clinical chemistry, 2011. 57(10): p. 1444-1451.

173. Sista, R., et al., Rapid, single-step assay for Hunter syndrome in dried blood spots using digital microfluidics. Clinica Chimica Acta, 2011. 412(19): p. 1895-1897.

174. Jebrail, M.J., et al., A digital microfluidic method for dried blood spot analysis. Lab on a Chip, 2011. 11(19): p. 3218-3224.

175. Mousa, N.A., et al., Droplet-scale estrogen assays in breast tissue, blood, and serum. Science Translational Medicine, 2009. 1(1): p. 1ra2-1ra2.

176. Ng, A.H., et al., Digital Microfluidic Platform for the Detection of Rubella Infection and Immunity: A Proof of Concept. Clinical chemistry, 2015. 61(2): p. 420-429.

177. Millington, D.S., et al., Development of Biomarker Assays for Clinical Diagnostics Using a Digital Microfluidics Platform. Dried Blood Spots: Applications and Techniques, 2014: p. 325-331.

178. Pamula, V., et al. A droplet-based lab-on-a-chip for colorimetric detection of nitroaromatic explosives. in Micro Electro Mechanical Systems, 2005. MEMS 2005. 18th IEEE International Conference on. 2005. IEEE.

179. Sista, R.S., et al., Rapid assays for Gaucher and Hurler diseases in dried blood spots using digital microfluidics. Molecular genetics and metabolism, 2013. 109(2): p. 218-220.

180. Martin, J.G., et al., Toward an artificial Golgi: redesigning the biological activities of heparan sulfate on a digital microfluidic chip. Journal of the American Chemical Society, 2009. 131(31): p. 11041-11048.

181. Millman, J.R., et al., Anisotropic particle synthesis in dielectrophoretically controlled microdroplet reactors. Nature Materials, 2005. 4(1): p. 98-102.

182. Jebrail, M.J., et al., Synchronized Synthesis of Peptide-Based Macrocycles by Digital Microfluidics. Angewandte Chemie, 2010. 122(46): p. 8807-8811.

183. Keng, P.Y., et al., Micro-chemical synthesis of molecular probes on an electronic microfluidic device. Proceedings of the National Academy of Sciences, 2012. 109(3): p. 690-695.

184. Abdelgawad, M., et al., All-terrain droplet actuation. Lab on a Chip, 2008. 8(5): p. 672-677.

185. Hung, P.-Y., et al., Genomic DNA extraction from whole blood using a digital microfluidic (DMF) platform with magnetic beads. Microsystem Technologies, 2015: p. 1-8.

186. Hua, Z., et al., Multiplexed real-time polymerase chain reaction on a digital microfluidic platform. Analytical chemistry, 2010. 82(6): p. 2310-2316.

187. Welch, E.R.F., et al., Picoliter DNA sequencing chemistry on an electrowetting-based digital microfluidic platform. Biotechnology journal, 2011. 6(2): p. 165-176.

188. Hua, Z., et al., Multiplexed real-time polymerase chain reaction on a digital microfluidic platform. Analytical chemistry, 2010. 82(6): p. 2310-2316.

189. Barbulovic-Nad, I., S.H. Au, and A.R. Wheeler, A microfluidic platform for complete mammalian cell culture. Lab on a Chip, 2010. 10(12): p. 1536-1542.

190. Allazetta, S. and M.P. Lutolf, Stem cell niche engineering through droplet microfluidics. Current opinion in biotechnology, 2015. 35: p. 86-93.

191. Zhou, J., et al., Electrowetting-based multi-microfluidics array printing of high resolution tissue construct with embedded cells and growth factors. Virtual and Physical Prototyping, 2007. 2(4): p. 217-223.

192. Kumar, P., et al., Digital microfluidics for time-resolved cytotoxicity studies on single non-adherent yeast cells. Lab on a Chip, 2015. 15(8): p. 1852-1860.

193. Rival, A., et al., An EWOD-based microfluidic chip for single-cell isolation, mRNA purification and subsequent multiplex qPCR. Lab on a Chip, 2014. 14(19): p. 3739-3749.

194. Bender, B.F., A.P. Aijian, and R.L. Garrell, Digital microfluidics for spheroid-based invasion assays. Lab on a Chip, 2016. 16(8): p. 1505-1513.

195. Miller, E.M., et al., A digital microfluidic approach to heterogeneous immunoassays. Analytical and bioanalytical chemistry, 2011. 399(1): p. 337-345.

196. Cao, J., et al., A microfluidic multiplex proteomic immunoassay device for translational research. Clinical proteomics, 2015. 12(1): p. 1.

197. Ng, A.H., et al., Digital microfluidic magnetic separation for particle-based immunoassays. Analytical chemistry, 2012. 84(20): p. 8805-8812.

198. Chao, T.C. and N. Hansmeier, Microfluidic devices for high-throughput proteome analyses. Proteomics, 2013. 13(3-4): p. 467-479.

199. Mok, J., et al., Digital microfluidic assay for protein detection. Proceedings of the National Academy of Sciences, 2014. 111(6): p. 2110-2115.

200. Luk, V.N., et al., Digital microfluidic hydrogel microreactors for proteomics. Proteomics, 2012. 12(9): p. 1310-1318.

201. Kim, H., et al., Automated digital microfluidic sample preparation for next-generation DNA sequencing. Journal of the Association for Laboratory Automation, 2011. 16(6): p. 405-414.

202. Zeng, Z., et al., Portable electrowetting digital microfluidics analysis platform for chemiluminescence sensing. IEEE Sensors Journal, 2016. 16(11): 4531-4536.

203. Khan, S., L. Lorenzelli, and R.S. Dahiya, Technologies for printing sensors and electronics over large flexible substrates: a review. Sensors Journal, IEEE, 2015. 15(6): p. 3164-3185.

204. Tavana, H., et al., Contact angle hysteresis on fluoropolymer surfaces. Advances in colloid and interface science, 2007. 134: p. 236-248.

205. Limbut, W., et al., A comparative study of capacitive immunosensors based on self-assembled monolayers formed from thiourea, thioctic acid, and 3-mercaptopropionic acid. Biosensors and Bioelectronics, 2006. 22(2): p. 233-240.

206. Chaki, N.K. and K. Vijayamohanan, Self-assembled monolayers as a tunable platform for biosensor applications. Biosensors and Bioelectronics, 2002. 17(1): p. 1-12.

207. Cho, S.K. and C.-J. Kim. Particle separation and concentration control for digital microfluidic systems. in Micro Electro Mechanical Systems, 2003. MEMS-03 Kyoto. IEEE The Sixteenth Annual International Conference on. 2003. IEEE.

208. Zhao, Y., U.-C. Yi, and S.K. Cho. Highly efficient in-droplet particle concentration and separation by twDEP and EWOD for digital microfluidics. in Micro Electro Mechanical Systems, 2007. MEMS. IEEE 20th International Conference on. 2007. IEEE.

209. Paik, P., V.K. Pamula, and R.B. Fair, Rapid droplet mixers for digital microfluidic systems. Lab on a Chip, 2003. 3(4): p. 253-259.

210. García-Sánchez, P., A. Ramos, and F. Mugele, Electrothermally driven flows in ac electrowetting. Physical Review E, 2010. 81(1): p. 015303.

211. Lee, K.Y., et al., Magnetic droplet microfluidic system incorporated with acoustic excitation for mixing enhancement. Sensors and Actuators A: Physical, 2016. 243: p. 59-65.

212. Ko, S.H., H. Lee, and K.H. Kang, Hydrodynamic flows in electrowetting. Langmuir, 2008. 24(3): p. 1094-1101.

213. Lee, H., et al., An electrohydrodynamic flow in ac electrowetting. Biomicrofluidics, 2009. 3(4): p. 044113.

214. Nilsson, J., et al., Review of cell and particle trapping in microfluidic systems. Analytica chimica acta, 2009. 649(2): p. 141-157.

215. Karimi, A., S. Yazdi, and A. Ardekani, Hydrodynamic mechanisms of cell and particle trapping in microfluidics. Biomicrofluidics, 2013. 7(2): p. 021501.

216. Grier, D.G., A revolution in optical manipulation. Nature, 2003. 424(6950): p. 810-816.

217. Hölzel, R., et al., Trapping single molecules by dielectrophoresis. Physical review letters, 2005. 95(12): p. 128102.

218. Lin, Y.-H. and G.-B. Lee, An optically induced cell lysis device using dielectrophoresis. Applied Physics Letters, 2009. 94(3): p. 033901.

219. Lapizco-Encinas, B.H. and M. Rito-Palomares, Dielectrophoresis for the manipulation of nanobioparticles. Electrophoresis, 2007. 28(24): p. 4521-4538.

220. Jones, T.B., Basic theory of dielectrophoresis and electrorotation. IEEE Engineering in medicine and Biology Magazine, 2003. 22(6): p. 33-42.

221. Zhang, C., et al., Dielectrophoresis for manipulation of micro/nano particles in microfluidic systems. Analytical and bioanalytical chemistry, 2010. 396(1): p. 401-420.

222. Rezaei Nejad, H., et al., A molecular dynamics study of nano-bubble surface tension. Molecular Simulation, 2011. 37(01): p. 23-30.

223. Alizadeh, T. and A. Akbari, A capacitive biosensor for ultra-trace level urea determination based on nano-sized urea-imprinted polymer receptors coated on graphite electrode surface. Biosensors and Bioelectronics, 2013. 43: p. 321-327.

224. Jomeh, S., Development of a microfluidic capture device for the manipulation and concentration of waterborne pathogens. 2013, University of British Columbia.